# The sources of rural atmospheric HONO and their impact on regional air quality in the North China Plain

Chaoyang Xue

**To cite this version:**

Chaoyang Xue. The sources of rural atmospheric HONO and their impact on regional air quality in the North China Plain. Other. Université d'Orléans; University of Chinese academy of sciences, 2020. English. NNT : 2020ORLE3107 . tel-03272454

**HAL Id: tel-03272454**

**https://theses.hal.science/tel-03272454**

Submitted on 28 Jun 2021

# UNIVERSITÉ D'ORLÉANS

## ÉCOLE DOCTORALE
## ENERGIE, MATERIAUX, SCIENCES DE LA TERRE ET DE L'UNIVERS
## LABORATOIRE DE PHYSIQUE ET CHIMIE DE L'ENVIRONNEMENT ET DE L'ESPACE (LPC2E)

**THÈSE** présentée par:

**Chaoyang XUE**

pour obtenir le grade de: **Docteur de l'Université d'Orléans**

Discipline/ Spécialité: Chimie atmosphérique (Atmospheric chemistry)

# The Sources of Rural Atmospheric HONO and Their Impact on Regional Air Quality in The North China Plain

**THÈSE dirigée par:**

| | |
|---|---|
| **Prof. Valéry CATOIRE** | LPC2E, CNRS-Université d'Orléans |
| **Dr. Gisèle KRYSZTOFIAK** | LPC2E, CNRS-Université d'Orléans |
| **Prof. Yujing MU** | RCEES, CAS-University of CAS |

---

**JURY:**

| | | |
|---|---|---|
| **Dr. Abdelwahid MELLOUKI** | ICARE, CNRS | President |
| **Prof. Maofa GE** | IC, CAS | Rapporteur |
| **Dr. Christian GEORGE** | IRCELYON, CNRS | Rapporteur |
| **Prof. Yujing MU** | RCEES, CAS-University of CAS | Co-supervisor |
| **Prof. Valéry CATOIRE** | LPC2E, CNRS-Université d'Orléans | Supervisor |
| **Prof. Min HU** | PKU | Examinateur |
| **Prof. Zhongming CHEN** | PKU | Examinateur |

# Acknowledgments

Time flies! It has already been almost six years since the first time I conducted scientific research in the summer of 2014 when I just started to be a master student. During this period, lots of friends, teachers, and families gave me lots of help that I appreciated very much.

I wish to express my sincere appreciation to my supervisors, Professor Valéry Catoire, Doctor Gisèle Krysztofiak, and Professor Yujing Mu, who are very nice and professional scientists. They convincingly guided and encouraged me to be professional and do the right thing even when the road got tough. Without their persistent help and patience, the goal of this thesis would not have been realized.

I would like to thank Doctor Abdelwahid Mellouki and Doctor Daële Véronique, who have helped lots of students to get an internship between France and China. Without their help, I would not have the chance to study in France. They also helped and taught me a lot and took care of me during my stay in France.

I am grateful to Doctor Jörg Kleffmann. The corporation with him helped me to understand much deeper on my topic. And his professionalism and generosity encouraged me to improve my understanding of scientific topics.

I wish to acknowledge the help provided by the technical, scientific, and support staff in LPC2E and ICARE, Orleans. It will be a good memory for me when I think about: the teaching on SPIRIT from Claude Robert and Stéphane Chevrier; the discussion with Yangang Ren, Max Mcgillen, Ibrahim Ouchen, and Min Cai; the conversation with Christophe Guimbaud, Michel Chartier and Patrick Jacquet; and the help from Fabrice Jégou, Isabelle Langer, and Catherine Hong.

In the same office, Mariam Tidiga, Vanessa Brocchi, and Francois Bernard guided me a lot on the life in Orleans, the work in our lab, etc., which I really appreciated.

I'm also grateful to my Chinese friends who also study in France. They are Pinpin Wang, Hao Li, Wei Wei, Zhiwei Hu, Qian Li, Fengfeng Zhang, Juan Li, Xiaoqing Wang, Xiaoyan Zhu, Zhaojing Ni, Yunfeng Li. Thank you for the accompany and help.

I also want to say thank you to the members of the jury, including Dr. Abdelwahid Mellouki, Dr. Christian George, Prof. Maofa Ge, Prof. Valéry Catoire, Prof. Yujing Mu, Prof. Min Hu and Prof. Zhongming Chen for my defense. I deeply appreciate your presence in my defense. It is whole-heartedly appreciated that your great advice for my

study proved monumental towards the success of my defense.

Thanks to my girlfriend Mingyi Wang, I am so lucky to meet you. Your accompany, understanding, trust, and support make me stronger and better. Most importantly, none of this could have happened without my family. Thanks to my family for their support and care over the years, and thanks again to my parents for creating a pleasant environment for my growth and study.

March 2020

Orleans

## List of Figures

## List of Tables

# Résumé

Les radicaux hydroxyles (OH) sont l'oxydant le plus important dans la chimie troposphérique et peuvent réagir avec la plupart des gaz-traces dans l'atmosphère avec la production possible de pollution secondaire (comme l'ozone, les particules, etc...), résultant en un impact significatif sur la qualité de l'air régional et le changement climatique mondial. La photolyse de l'acide nitreux atmosphérique (HONO) est l'une des sources primaires d'OH les plus importantes avec une contribution de 20% à 80%. Cependant, les sources de HONO ne sont pas bien comprises. Par exemple, les rapports de mélange HONO élevés et inattendus observés dans les régions polluées ne peuvent toujours pas être bien expliqués par les modèles incluant des sources de HONO connues. Par conséquent, cette étude a sélectionné un site rural typique de la grande Plaine de Chine du Nord (PCN) où la pollution de l'air est encore très sévère par rapport à d'autres régions du monde. Les émissions de HONO des sols agricoles en été et leur impact sur la qualité de l'air régional ont été quantifiés par un modèle de chimie-transport (Système communautaire de modélisation de la qualité de l'air à plusieurs échelles, CMAQ). En outre, une campagne de terrain détaillée comprenant des mesures de HONO a été menée sur ce site rural. Un modèle de boîte (Master Chemical Mechanism, MCM) a été utilisé pour explorer la formation de HONO et son rôle dans la formation de OH et de nitrate particulaire. Les principaux résultats obtenus dans cette étude sont les suivants:

1. Un système a été développé pour collecter efficacement et quantifier avec précision l'HONO atmosphérique. Sur la base de la méthode chimique par voie humide, une bobine d'écoulement (stripping coil) équipée de la méthode de chromatographie ionique (SC-IC) a été développée pour mesurer l'HONO atmosphérique et ses performances ont été systématiquement évaluées en laboratoire et sur le terrain. Tout d'abord, l'efficacité de la collecte et ses facteurs d'influence (par exemple, le débit d'échantillonnage de gaz, le débit de liquide) ont été testés dans la chambre à smog dans des conditions spécifiques. Nous avons constaté que la coexistence de $NO_2$ et de $SO_2$ a eu un impact positif significatif sur la mesure de HONO lors de l'utilisation d'une solution d'absorption typique de carbonate de sodium (méthode N). Cependant, l'impact a été remarquablement réduit lorsque de l'eau ultrapure a été utilisée comme solution d'absorption (méthode H). La méthode H a montré une efficacité de collecte élevée (>

90%) à des niveaux ambiants typiques de $NO_2$ et de $SO_2$. Deuxièmement, des comparaisons entre la SC-IC développée dans cette étude et les deux techniques de photomètre d'absorption à long chemin (LOPAP) ou une technique de spectroscopie d'absorption résonante amplifiée par cavité (CEAS) ont été menées lors de campagnes sur le terrain. Nous avons trouvé des mesures cohérentes de HONO entre SC-IC et LOPAP et CEAS déduites de corrélations élevées ($R^2$=0,90-0,96, pente=0,95-1,06), indiquant la capacité de la SC-IC à mesurer l'HONO atmosphérique. Nous avons également déployé un contrôleur logique programmable pour collecter automatiquement des échantillons de liquide en ligne avec une fréquence d'échantillonnage aussi faible que 5 minutes. Cela a fourni la garantie technique pour les campagnes suivantes pour mesurer le flux d'émission atmosphérique de HONO et la concentration de HONO du sol agricole.

2. Un système de chambres dynamiques à double toit ouvert (OTC : open top chamber) a été développé pour quantifier avec précision les émissions de HONO du sol. Comme $NO_2$ génère facilement HONO grâce à des réactions hétérogènes sur les surfaces et le film d'eau condensé peut également absorber le HONO gazeux, ce système dépasse la capacité des chambres dynamiques traditionnelles à quantifier le flux d'émission de HONO du sol. Le système OTC développé dans cette étude se composait de deux chambres dynamiques. Le fond d'une chambre était recouvert d'un film de Téflon inerte en tant que chambre de référence (Ref-chambre) et l'autre couvrait directement le sol en tant que chambre de mesure (Exp-chambre). Ainsi, le flux d'émission de HONO du sol pouvait être déduit de la différence des rapports de mélange HONO dans les deux chambres. Le système OTC a pu réduire l'impact de la réaction hétérogène du $NO_2$ ambiant sur les surfaces de la chambre. En outre, les deux chambres ont été continuellement rincées par l'air ambiant à un débit constant, ce qui pouvait réduire considérablement la formation de film d'eau condensée sur les surfaces des chambres. Nous avons ensuite testé le système OTC en mesurant le flux de NO à des flux de relargage connus et avons constaté que le flux mesuré était très cohérent avec le flux donné.

3. Le flux d'émission de HONO du sol agricole typique de la PCN a été obtenu par le système OTC et son impact sur la qualité de l'air régional a été quantifié par un modèle de chimie- transport (CMAQ). En utilisant les systèmes SC-IC et OTC développés dans notre étude, deux campagnes de terrain ont été menées pour mesurer le flux d'émission de HONO du sol et les paramètres associés au cours de l'été 2016 et 2017 dans le village

de Dongbaituo, Baoding, Hebei. Les observations ont montré que le flux d'émission de HONO augmentait rapidement après la fertilisation sur le sol agricole, et une émission significative de HONO a été observée en continu 15 jours après la fertilisation. De plus, le flux d'émission observé présentait une variation diurne évidente avec un pic à midi et un minimum la nuit. Les plus grandes émissions de HONO ont atteint jusqu'à 350 ng N $m^{-2}$ $s^{-1}$ après la fertilisation, ce qui était de 1 à 2 ordres de grandeur plus élevé que les valeurs rapportées d'études limitées. Pendant ce temps, une évaluation remarquable des rapports de mélange de HONO atmosphérique avec un pic à midi a été trouvée après la fertilisation, ce qui a confirmé à nouveau une forte émission de HONO dans le sol. Selon la relation entre les flux d'émission de HONO et la température et l'humidité relative du sol (RH) observées, la variation diurne moyenne du flux d'émission de HONO a été bien reproduite par une équation d'Arrhenius. Le paramétrage a ensuite été adopté dans le modèle CMAQ pour explorer l'impact des émissions de HONO du sol sur la qualité de l'air régional. Les résultats du modèle ont montré que les niveaux moyens diurnes d'$O_3$ et d'OH dans la PCN ont augmenté d'environ 8 ppbv et $5\times10^6$ molécules $cm^{-3}$, respectivement, indiquant l'impact significatif du processus de fertilisation intensive sur le sol agricole sur la pollution atmosphérique régionale et la capacité d'oxydation atmosphérique pendant l'été de la PCN. Des études plus similaires doivent être menées dans cette région ou dans des régions similaires.

4. Un nouveau mécanisme d'émission de HONO du sol a été proposé. Sur la base des techniques des réacteurs à écoulement, des expériences en laboratoire ont été menées pour mesurer les émissions de HONO et de NO provenant a) d'échantillons de sol originaux avec des engrais à base d'ammonium, b) d'échantillons de sol stérilisés avec des engrais nitrate, c) d'échantillons de sol stérilisés avec des engrais à base d'ammonium, et d) des échantillons de sol originaux avec des engrais à base d'ammonium et des inhibiteurs de nitrification. Nous avons constaté que seuls les échantillons du sol d'origine contenant des engrais à base d'ammonium pouvaient émettre de manière significative HONO et NO, ce qui indique que les émissions de HONO provenaient principalement du processus de nitrification. Au cours du processus de nitrification, $NH_4^+$ a été converti en $NO_3^-$ par les bactéries nitrifiantes avec des produits intermédiaires de $NO_2^-$ et $H^+$. La combinaison de $NO_2^-$ et de $H^+$ a augmenté la concentration de HONO dans l'environnement de la solution du sol, ce qui a favorisé la libération de HONO dans l'atmosphère. De plus, les émissions de HONO et de NO ont augmenté avec la température du sol dans la plage de 18 à 35 ºC, mais ont diminué avec

l'humidité relative du gaz de rinçage, ce qui pourrait bien expliquer la variation diurne observée des émissions de HONO du sol. D'une part, l'augmentation de la température du sol pourrait accélérer les activités de nitrification; d'autre part, elle a réduit la solubilité de HONO dans la solution du sol et accéléré l'évaporation de l'eau des surfaces du sol, ce qui a favorisé la libération de HONO du sol. De même, une humidité relative élevée du gaz de rinçage a supprimé l'évaporation de l'eau des surfaces du sol, entraînant de faibles émissions de HONO du sol.

5. La formation de HONO dans la PCN rurale et son impact sur la formation de OH atmosphérique et de nitrate particulaire ont été quantifiés. Basé sur une campagne hivernale détaillée de Novembre 2017 à Janvier 2018 menée sur un site rural de la plaine de Chine du Nord, un modèle de boîte (MCM v3.3.1) a été utilisé pour simuler le bilan de HONO de jour et la formation de nitrate. Nous avons constaté que le HONO diurne observé pouvait être bien expliqué par les sources connues dans le modèle. La conversion hétérogène du $NO_2$ sur les surfaces du sol et la réaction homogène du NO avec OH étaient les sources HONO dominantes avec des contributions de plus de 36% et 34% au HONO diurne, respectivement. La contribution de la photolyse du nitrate de particules et des réactions du $NO_2$ sur les surfaces des aérosols était négligeable en périodes propres (2%) et légèrement plus élevée en période de pollution (8%). En outre, la diminution progressive du coefficient de capture de $NO_2$ sur les surfaces du sol avec des niveaux de pollution pourrait mieux expliquer le HONO observé à différents niveaux de pollution.

La photolyse de HONO a agi comme la source dominante d'OH primaire avec une contribution de plus de 92%, beaucoup plus élevée que les autres sources d'OH telles que la photolyse d'$O_3$, $H_2O_2$, HCHO, etc. Les niveaux d'OH relativement élevés dus à la photolyse rapide de HONO sur le site rural ont fait remarquablement accélérer les réactions en phase gazeuse, entraînant la formation rapide de nitrate et d'autres polluants secondaires pendant la journée. Par exemple, les rapports de mélange $HO_x$ ($OH+HO_2$) et la formation potentielle de nitrate étaient respectivement 1 à 8 fois et 1 à 2 fois sous-estimés par le modèle si HONO n'était pas contraint par l'observation, ce qui implique le rôle important de HONO dans la capacité d'oxydation atmosphérique et la formation des nitrates en hiver dans cette région.

**Mot clé**: HONO, Plaine de Chine du Nord, émissions atmosphériques, $O_3$, nitrate particulaire

# Abstract

Hydroxyl radicals (OH) are the most important oxidant in the tropospheric chemistry that can react with most trace gases in the atmosphere with the possible production of secondary pollution (such as ozone, particulate matter, etc.), resulting in a significant impact on regional air quality and global climate change. The photolysis of atmospheric nitrous acid (HONO) is one of the most important primary OH sources with a contribution of 20%-80%. However, the sources of HONO were not well understood. For example, unexpected high HONO mixing ratios observed in polluted regions still cannot be well explained by the models with known HONO sources. Therefore, this study selected a typical rural site in the North China Plain (NCP) where air pollution is still very severe compared to other regions in the world. HONO emissions from agricultural soil in the summertime and their impact on regional air quality were quantified by a chemistry transport model (The Community Multiscale Air Quality Modeling System, CMAQ). Besides, a comprehensive field campaign, including HONO measurement was conducted at this rural site. A box model (Master Chemical Mechanism, MCM) was used here to explore HONO formation and its role in the formation of OH and particulate nitrate. The main results obtained in this study are as follows:

1. A system was developed to efficiently collect and accurately quantify atmospheric HONO. Based on the wet chemical method, a stripping coil equipped with ion chromatograph (SC-IC) method was developed to measure atmospheric HONO and its performance was systematically evaluated in the laboratory and field conditions. First of all, the collection efficiency and its influencing factors (e.g., gas sampling flow, liquid flow) were tested in the smog chamber under specific conditions. We found that the co-existence of $NO_2$ and $SO_2$ caused a significant positive impact on HONO measurement when using a typical absorption solution of sodium carbonate (N-method). However, the impact was remarkably reduced when ultrapure water was used as the absorption solution (H-method). H-method showed a high collection efficiency (>90%) under typical ambient levels of $NO_2$ and $SO_2$. Secondly, intercomparisons between the SC-IC developed in this study and two Long Path Absorption Photometer (LOPAP) techniques or a Cavity-Enhanced Absorption Spectroscopy (CEAS) technique were conducted in field campaigns. We found consistent HONO

measurements by SC-IC with LOPAP and CEAS inferred from high correlations ($R^2$=0.90-0.96, slope=0.95-1.06), indicating the capacity of SC-IC to measure atmospheric HONO. We furtherly deployed a programmable logic controller to automatically collect liquid samples online with a sampling frequency as low as 5 min. This provided the technical guarantee for the following campaigns to measure atmospheric HONO concentrations and HONO emission flux from agricultural soil.

2. A twin open-top dynamic chambers (OTC) system was developed to accurately quantify HONO emissions from soil. $NO_2$ easily generates HONO through heterogeneous reactions on surfaces and the condensed water film can also absorb gaseous HONO, which are the key challenges for traditional dynamic chambers to quantify soil HONO emission flux. The OTC system developed in this study consisted of two dynamic chambers. The bottom of one chamber was covered by inert Teflon film as the reference chamber (Ref-chamber) and the other one directly covered the soil as the experimental chamber (Exp-chamber). Thus, the soil HONO emission flux could be inferred from the difference of HONO mixing ratios in the two chambers. The OTC system was able to reduce the impact of ambient $NO_2$ heterogeneous reaction on the chamber surfaces. Besides, both chambers were continuously flushed by ambient air at a consistent flow, which could largely reduce the formation of condensed water film on chamber surfaces. We then tested the OTC system by measuring NO flux at known releasing fluxes and found that the measured flux was highly consistent with the given flux.

3. HONO emission flux from typical agricultural soil in the NCP was obtained by the OTC system and its impact on regional air quality was quantified by a chemistry transport model (CMAQ). By using the SC-IC and OTC systems developed in our study, two field campaigns were carried out to measure soil HONO emission flux and related parameters in the summer of 2016 and 2017 in Dongbaituo Village, Baoding, Hebei. The observations showed that the HONO emission flux rapidly increased after fertilization on the agricultural soil, and significant HONO emission was continuously observed in 15 days after fertilization. Besides, the observed emission flux exhibited an evident diurnal variation with a peak at noontime and a minimum at nighttime. The larges HONO emission reached up to 350 ng N $m^{-2}$ $s^{-1}$ after fertilization which was 1-2 orders of magnitude higher than the reported values from limited studies. Meanwhile, a remarkable increase of atmospheric HONO mixing ratios with a noontime peak was found after fertilization, which confirmed strong soil HONO emission again.

According to the relationship of HONO emission fluxes and the observed soil temperature and relative humidity (RH), the averaged diurnal variation of HONO emission flux was well reproduced by an Arrhenius equation. The parameterization was then adopted to the CMAQ model to explore the impact of soil HONO emission on regional air quality. Model results showed that daytime averaged levels of $O_3$ and OH in the NCP increased by about 8 ppbv and $5\times10^6$ molecules $cm^{-3}$, respectively, indicating the significant impact of the intensive fertilization process on agricultural soil on regional air pollution and atmospheric oxidizing capacity in the summertime of the NCP. More similar studies need to be conducted in this region or similar regions.

4. A new mechanism for soil HONO emission was proposed. Based on flow tube techniques, laboratory experiments were conducted to measure HONO and NO emission from a) original soil samples with ammonium fertilizers, b) sterilized soil samples with nitrate fertilizers, c) sterilized soil samples with ammonium fertilizers, and d) original soil samples with ammonium fertilizers and nitrification inhibitors. We found that only the original soil samples with ammonium fertilizers could significantly emit HONO and NO, indicating that the HONO emission was mainly from the nitrification process. During the nitrification process, $NH_4^+$ was converted to $NO_3^-$ by the nitrifying bacteria with intermediate products of $NO_2^-$ and $H^+$. The combination of $NO_2^-$ and $H^+$ increased the concentration of HONO in the soil solution environment which promoted the release of HONO to the atmosphere. Additionally, HONO and NO emissions increased with soil temperature in the range of 18-35 ºC but decreased with the relative humidity of the flushing gas, which could well explain the observed diurnal variation of soil HONO emissions. On the one hand, the increase in soil temperature could accelerate nitrification activities; on the other hand, it reduced the solubility of HONO in soil solution and accelerate water evaporation from soil surfaces, which promoted the release of HONO from the soil. Similarly, high relative humidity of the flushing gas suppressed water evaporation from soil surfaces, leading to low HONO emissions from the soil.

5. HONO formation in the rural NCP and its impact on the formation of atmospheric OH and particulate nitrate were quantified. Based on a comprehensive winter field campaign from November 2017 to January 2018 conducted at a rural site of the North China Plain, a box model (MCM v3.3.1) was used to simulate the daytime HONO budget and nitrate formation. We found that the observed daytime HONO could be well explained by the known sources in the model. The heterogeneous conversion of

$NO_2$ on ground surfaces and the homogeneous reaction of NO with OH were the dominant HONO sources with contributions of more than 36% and 34% to daytime HONO, respectively. The contribution from the photolysis of particulate nitrate and the reactions of $NO_2$ on aerosol surfaces were negligible in clean periods (2%) and slightly higher in polluted periods (8%). Besides, the gradual decrease of $NO_2$ uptake coefficient on ground surfaces with pollution levels could better explain the observed HONO under different pollution levels.

The photolysis of HONO acted as the dominant source for primary OH with a contribution of more than 92%, much higher than other OH sources such as the photolysis of $O_3$, $H_2O_2$, HCHO, etc. The relatively high OH levels due to fast HONO photolysis at the rural site remarkably accelerated gas-phase reactions, resulting in the rapid formation of nitrate as well as other secondary pollutants in the daytime. For example, $HO_x$ ($OH+HO_2$) mixing ratios and potential nitrate formation were 1-8 timed and 1-2 times underestimated by the model, respectively, if HONO was not constrained by the observation, implying the critical role of HONO in atmospheric oxidizing capacity and nitrate formation in the wintertime of this region.

**Keyword:** HONO, North China Plain, atmospheric emissions, $O_3$, particulate nitrate

# Chapter 1 Introduction: atmospheric chemistry of HONO

The hydroxyl radical (OH) is the most important oxidant in the troposphere to initiate the oxidation of organic and inorganic compounds, leading to the formation of secondary pollutants such as ozone ($O_3$), secondary organic (SOA) and secondary inorganic aerosols (SIA), which deteriorate regional air quality[1,2]. Therefore, a vast number of field campaigns over the world have been conducted with the target to improve our understanding of radical chemistry, including the quantification of the sources and sinks of OH[1,2]. Nitrous acid (HONO) has been recognized as an important primary OH source to initiate daytime atmospheric photochemistry[3]. Recent studies further found that HONO not only played a dominant role in triggering daytime atmospheric chemistry in the early morning but also acted as an important and even the dominant OH source throughout the whole day, e.g., the photolysis of HONO contributed ca. 20%-80% of atmospheric primary OH production in polluted regions[4–7]. Because the classical gas-phase reaction of NO with OH cannot explain the extremely high HONO levels observed in the daytime, additional HONO sources were further proposed based on laboratory studies and field campaigns.

The North China Plain (NCP) suffers from severe particle/aerosol pollution (usually called haze pollution) in wintertime and $O_3$ pollution in the summertime, and extremely high HONO concentrations were also frequently observed during the winter haze pollution events in the NCP[8,9]. HONO formation and its impact on regional air pollution in the NCP, therefore, became a crucial scientific question that needs to be answered.

In this chapter, progress on HONO research is summarized, including 1) the role of HONO in the atmospheric chemistry, 2) the proposed HONO sources and sinks, 3) HONO measurement techniques, and 4) HONO measurements in the NCP region.

## 1.1 The role of HONO in atmospheric chemistry

### 1.1.1 Hydroxyl radicals (OH)

Hydroxyl radicals (OH) play a central role in atmospheric chemistry because of its high reactivity with inorganic ($NO_x$, $SO_2$, etc.) as well as organic compounds(VOCs, etc.), with potential formation of secondary pollutants such as aerosols and $O_3$[2,10–12]. Meanwhile, OH determines the lifetime of greenhouse gases such as $CH_4$ and $N_2O$, which notably affect the global climate change.

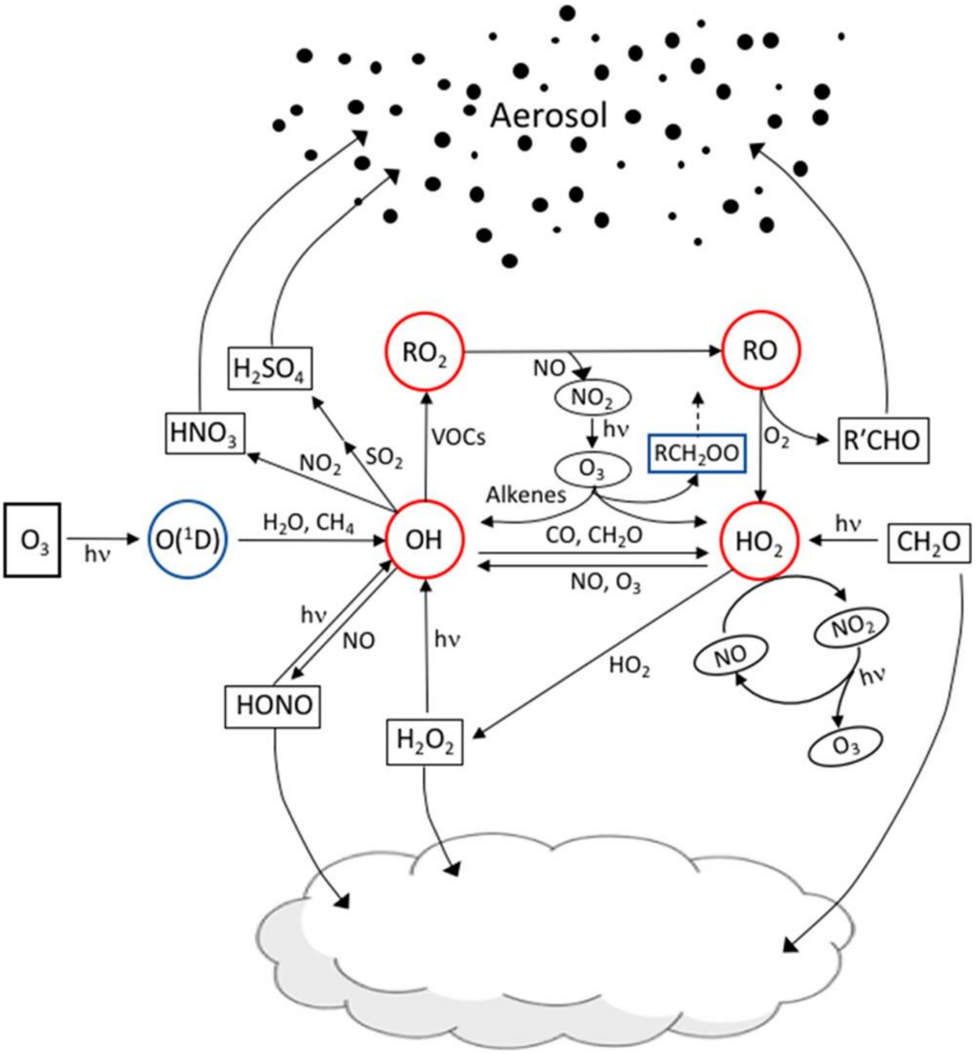

Figure 1.1 Examples of $HO_x$ formation, cycling and their environmental impact. (Taken from Burkholder et al. (2017)[13])

Figure 1.1 shows the $HO_x$ formation, cycling and their environmental impacts. The main OH sources contain the cycling between $HO_2$ and NO, and primary OH formation. The OH production from the conversion of $HO_2$ with NO is shown in equation (1.1).

$HO_2 + NO \rightarrow OH + NO_2$ (1.1)

Several primary OH sources were proposed as follows:

**a) Photolysis of $O_3$**

At the global scale, atmospheric OH mainly came from the reaction of excited oxygen atoms ($O(^1D)$) with water vapor[12,14]. $O(^1D)$ came from the photolysis of $O_3$. Related mechanisms were shown in the following equations.

$O_3 + h\nu \rightarrow O(^1D) + O_2 \quad (\lambda<320nm)$ (1.2)

$O(^1D) + H_2O \rightarrow 2OH$ (1.3)

$O(^1D) + M \rightarrow O(^3P) + M \quad M=N_2 \text{ or } O_2$ (1.4)

The occurrence of channel (1.3) depends on the atmospheric relative humidity and temperature. For example, during a summer campaign in Germany, this channel had a branching ratio of about 6%-15%, with an average of 10%[3], the remaining being de-excitation by collision.

**b) Photolysis of HCHO**

During the photolysis of HCHO, H atoms can be formed and react with $O_2$ to form $HO_2$. Through equation (1.1), $HO_2$ is rapidly converted to OH. Related mechanisms can be simplified shown as follows:

$HCHO + h\nu \rightarrow H + HCO\ (J_{rad}, \lambda < 340\ nm)$ (1.5)

$HCHO + h\nu \rightarrow H_2 + CO\ (J_{mol}, \lambda < 365\ nm)$ (1.6)

$H + O_2 \rightarrow HO_2$ (1.7)

$HCO + O_2 \rightarrow HO_2 + CO$ (1.8)

$HO_2 + NO \rightarrow OH + NO_2$ (1.1)

During the process, the reaction (1.1) is much faster than other steps, which will play the rate-determining step. Sources of HCHO contain primary emission and secondary formation. Since radical-driven atmospheric chemistry was mainly responsible for secondary HCHO formation[15], the primary emissions were typically considered as a net radical source[5,16].

**c) Ozonolysis of alkenes**

Reactions of $O_3$ and alkenes produce the Criegee intermediate[17], which could be decomposed with the production of OH and $RO_2$ radicals[18]. The yield of OH, which was in the range of 7%-100%, depended on the structure of the alkenes.

**d) Photolysis of hydroxyl peroxide ($H_2O_2$)**

The photolysis of one $H_2O_2$ molecule could produce 2 OH. According to the MCM model (http://cprm.acom.ucar.edu/Models/TUV/Interactive_TUV/), the photolysis frequency of $H_2O_2$ was always low (few $10^{-7}$ $s^{-1}$), which was 3-4 orders of magnitude lower than other photolysis processes such as HONO (up to few $10^{-3}$ $s^{-1}$). Therefore, OH production from $H_2O_2$ photolysis was usually negligible.

**e) Photolysis of HONO**

The photolysis of HONO is detailed in the following section.

### 1.1.2 The contribution of HONO to OH

HONO was one of the most important OH precursors. It could be photolyzed under radiation with a wavelength of less than 400 nm, as shown in the following equation.

$$HONO + h\nu \rightarrow NO + OH \ (\lambda < 400\ nm) \qquad (1.9)$$

After the first detection of HONO in 1979 by Platt et al. (1980)[19], HONO was treated as the most important OH source in the morning after accumulation during nighttime. For example, Platt et al. (1980)[19] used the DOAS technique to measure atmospheric HONO and found 3 ppbv HONO before sunrise, which could produce an OH production rate of $2\times10^{7}$ molecules $cm^{-3}$ $s^{-1}$ after sunrise, playing the most important OH source. Alick et al. (2003)[3] observed up to 1 ppbv HONO in the morning hours and the OH production from HONO photolysis were much higher than the photolysis of HCHO and $O_3$.

With the advancement of HONO measurement techniques, low HONO mixing ratios during the daytime could be accurately quantified. Lots of HONO-involved campaigns were conducted all over the world. It was found that HONO not only played an essential role in OH production in the morning, but also played an essential role throughout the whole daytime, with a contribution of 20%-80%[3,4,16,20–24], and there were strong missing sources for daytime HONO[20,22,25–29]. For example, Kleffmann et al (2003)[23] observed noontime HONO up to 210 pptv in Forschungszentrum Karlsruhe (Germany), which was much higher than that calculated from the photo stationary state (90 pptv), indicating a strong daytime HONO source.

## 1.2 The proposed HONO sources and sinks

After several decades of research on HONO, various HONO formation paths were proposed. Some of them were already well studied, but some were still in critical discussion. This section summarizes the proposed HONO sources and sinks.

### 1.2.1 Direct emissions

Car exhaust could emit $NO_x$ as well as HONO. The ratio of HONO/NOx in the car exhaust was typically 0.03%-1.6%[30–32]. However, the ratio might change with the type of cars, the quality of the gasoline or diesel, and the experimental environmental conditions. For example, Trinh et al. (2017)[32] found the emission ratio of HONO/$NO_x$ from the petrol car and diesel car was in the range of 0.16%-1% with an average of

0.8%. Kurtenbach et al. (2001)[30] conducted HONO and NOx measurements in the tunnel and found an averaged HONO/$NO_x$ of (0.8±0.1)%. Liu et al. (2017)[31] carried out laboratory experiments on HONO emissions from the car exhaust and determined a HONO/$NO_x$ of 0.03%-0.42% with an average of 0.18%.

### 1.2.2 Homogeneous reactions

The homogeneous reaction of NO with OH could produce HONO. The path was well known and it's normally contained in the model mechanism as a default HONO source.

### 1.2.3 Heterogeneous conversion of $NO_2$

The heterogeneous conversion of $NO_2$ on various surfaces was proposed as one important HONO source both in the nighttime[33,34] and daytime. Besides, the heterogeneous conversion of $NO_2$ could be largely enhanced by solar radiation, which was a photosensitized reaction. For example, HONO could be formed during the heterogeneous $NO_2$ reactions on soot surfaces[35,36], humic acid surfaces[34,37–40], MgO surfaces[41], city grime surfaces[42], etc. The uptake coefficient could reach $2\times10^{-5}$, and was influenced by the solar intensity and $NO_2$ concentrations. For example, Stemmler et al. (2006)[38] and George et al. (2005)[37] firstly conducted laboratory experiments to explore the mechanism for the photosensitized heterogeneous reaction of $NO_2$ on organic surfaces, and proposed the well-accepted mechanism as shown in the following equations.

$$HA \overset{h\upsilon}{\rightarrow} A^{red} + X \tag{1.10}$$

$$A^{red} + X \rightarrow A' \tag{1.11}$$

$$A^{red} + NO_2 \rightarrow A'' + HONO \tag{1.12}$$

where HA, $A^{red}$, X, A´ and A´´ represent humic acid, reductive centers, unknown oxidants, unknown products formed in the deactivation process, and unknown products formed in the reduction process of $NO_2$, respectively.

This HONO formation path was often proven to be the dominant HONO source in various regions[43–50].

### 1.2.4 Photolysis of nitric acid and particulate nitrate

The adsorbed gas-phase nitric acid ($HNO_3$) on surfaces such as clean glass surfaces could produce HONO and $NO_2$[51]. However, the photolysis frequency was always low (few $10^{-7}$ $s^{-1}$), which could not make a significant impact like the heterogeneous $NO_2$ reactions, on the HONO budget. While, Zhou et al. (2003)[52] conducted field campaigns and laboratory experiments, and found the photolysis of $HNO_3$ was enhanced by 1-2 orders of magnitude when gas-phase $HNO_3$ was adsorbed on soil or leaf surfaces, which was expected to have an important impact on the HONO budget. Additionally, Zhou et al. (2011)[53] conducted field campaign to quantify the HONO emission flux above the canopy and found the upward HONO emission flux was positively correlated with the product of the loading of particulate nitrate and its photolysis frequency, indicating potential HONO formation from the photolysis of particulate nitrate ($pNO_3$) loaded on the canopy surfaces. Based on aircraft measurements, Ye et al. (2016)[54] found the HONO unknown source strength in the marine boundary layer was positively correlated with the product of the concentrations of particulate nitrate and its photolysis frequency obtained from laboratory experiments. Hence, they concluded that the photolysis of total nitrate ($HNO_3$+$pNO_3$) might play an essential role in HONO and $NO_x$ budgets in low $NO_x$ regions like marine or rural regions. Since then, several laboratory experiments based on flow tube techniques were conducted, and also found large photolysis frequencies up to several $10^{-4}$ $s^{-1}$ levels, 2-3 orders of magnitude higher than that of gas-phase $HNO_3$[55–57].

However, there was a model study indicating the enhancement of photolysis of $pNO_3$ was moderate, with enhancement less than 100, i.e., typically 30 or less.[58] So, more experiments need to be conducted to understand the process.

### 1.2.5 Acid displacement of soil surface nitrite by strong atmospheric acids

Based on flow tube experiments, Vandenboer et al. (2015)[59] found that HONO could react with carbonate on the soil surface to form a HONO reservoir, which could further react with strong atmospheric acids (HCl, $HNO_3$, etc.) with the release of HONO. This indicated HONO could be stored on the soil surfaces and furtherly acid-based displaced by strong atmospheric acids, which could have a potential impact on the daytime HONO budget, especially at noontime when atmospheric photochemistry was strong. However, recent model studies found the present HONO source had a negligible impact on the HONO budget[60]. Related reactions are as follows:

$$NaNO_2(s) + HCl(g) \rightarrow NaCl(s) + HONO(g) \quad (1.13)$$

$$NaNO_2(s) + HNO_3(g) \rightarrow NaNO_3(s) + HONO(g) \quad (1.14)$$

### 1.2.6 Soil HONO emissions

To our knowledge, the first time that soil was found to be a potential HONO source was in 1965, in an abstract of a Japan conference but without detailed discussion. In

1985, a scientist from Ibaraki University (Japan) found HONO emissions from sampled soil and measured the emission flux. He found higher HONO emissions from soil treated with ammonium fertilizer than other types of fertilizers. But this study did not attract widespread attention because of its limited techniques.

With the improvement of HONO measurement techniques and the revelation of the critical role of HONO in atmospheric chemistry, more studies found that soil emissions could play an important role in HONO formation[23,29,48,61–64].

In 2011, Su et al. (2011)[65] used a flow tube combined with LOPAP to measure continuous soil HONO emissions for the first time and proposed that the balance of $NO_2^-$ and $H^+$ is an important mechanism for soil HONO emissions, and the potential emission was expected to be greater under acid soil conditions.

In 2013, based on laboratory flow tube experiments, Oswald et al. (2013)[66] found that soil acidity was not the essential influencing factor on soil emissions of HONO, but ammonia-oxidizing bacteria could direct release HONO during the nitrification process. And they also found that weakly alkaline soils with high soil nitrogen content showed greater potential HONO emissions. In 2014, based on flow tube experiments, Donaldson et al. (2014)[67] found that soil HONO emissions mainly depended on the acidity and of the soil microenvironment rather than the bulk acidity. Therefore, both the abiotic and biotic formation of $NO_2^-$ on the soil surface could be HONO sources.

In 2015, Scharko et al. (2015)[68] conducted flow tubes experiments combined with isotope technology, and gene sequencing technology. They found that the HONO emitted from the soil comes from the conversion of $NH_4^+$, and the 16S rRNA (one gene sequence detected belongs to known ammonia oxidizing bacteria and archaea) content was higher in soil, showing higher HONO emissions, indicating that the HONO released from the soil came from ammonia-oxidizing bacteria. They also found that low soil pH was not an important factor since they found strong HONO emissions from alkaline soil samples.

In the same year, Weber et al. (2015)[69] also found that the HONO emitted from soil mainly comes from the biocrust on the soil surfaces through laboratory experiments, and also demonstrated the important role of microorganisms in soil HONO emission process.

In 2017, based on laboratory research, Ermel et al. (2017)[70] found that hydroxylamine ($NH_2OH$) could react with water on the surface to generate HONO, and hydroxylamine can be produced by multiple microbial communities (such as ammonia-oxidizing bacteria AOB, ammonia-oxidizing archaea AOA, etc.). Therefore, biotic soil HONO emissions might be much greater than expected before.

In 2019, Kim et al. (2019)[71] conducted laboratory research and found that the microenvironment (microbiological scale) pH was a key factor in the conversion of $NO_2^-$ in the soil into gaseous HONO. The microenvironment (microbiological scale) might have a significant impact on HONO release from the soil, which needs more studies to confirm.

However, it is still necessary to conduct more experiments, including laboratory research and field campaigns on soil HONO emissions, to reveal the mechanism and its impact in different regions.

### 1.2.7 Other HONO sources

Based on measurements in the free troposphere, the reaction of $NO_2$ with $HO_2{\cdot}H_2O$ complex was proposed as a significant HONO source[72]. However, a recent field campaign found a negligible impact of this reaction on the HONO budget[73]. Photolysis of ortho-nitrophenols[74] can also produce HONO, while it has been proved to have a negligible effect on the HONO budget at this site and other sites[60]. The reaction of excited $NO_2$ with $H_2O$ ($NO_2^*$+$H_2O$) could be a HONO source, but it is still rebutted by other studies[75,76].

## 1.3 HONO measurement techniques

The off-line method of Denuder absorption coupling ion chromatograph (Denuder-IC) had been widely used for atmospheric HONO measurements in the past[77,78], but it was not popular used due to the relatively low time resolution (4-6h), relatively high detection limit (80-600pptv) and fussy manual operation after the emergence of the online methods. The existing online methods mainly include DOAS (Differential Optical Absorption Spectroscopy)[77,78], CRDS (Cavity Ring-Down Spectroscopy)[79] and CEAS (Cavity Enhanced Absorption Spectroscopy)[80–83], FTIR (Fourier Transform InfraRed spectroscopy)[84], LOPAP (Long Path Absorption Photometer)[85–87], GAC (Gas and Aerosol Collector)[88], AIM-IC (Ambient Ion Monitor-IC)[89,90], SC-IC (Stripping Coil-Ion Chromatograph)[91], DNPH-HPLC (2,4-dinitrophenylhydrazine derivatization and high-performance liquid chromatograph)[92], LIF (Laser Induced Fluorescence)[83,93], and CIMS (Chemical Ionization Mass Spectrometry)[83,94,95]. Compared with other methods, the spectroscopic techniques of DOAS, CRDS, CEAS, and FTIR usually have relatively high HONO detection limits (>100 pptv), which cannot meet the demand for measuring atmospheric HONO around noontime when HONO concentration is usually less than 100 pptv[77,96–101]. Although the detection limits (2-20 pptv) and time resolution (minutes) of the methods of LIF and CIMS are desirable for atmospheric HONO measurements, they were not widely adopted for field HONO measurements probably due to high cost of the delicate instruments[83,93–95].

The wet-chemical methods of LOPAP, GAC, AIM-IC, and SC-IC are relatively cheaper and sensitive to HONO, and thus they are widely adopted for field HONO measurements[85–91]. However, the wet-chemical methods often suffer from interferences from atmospheric pollutants as well as artifact influence of the inlet tube during the sampling process[102]. To minimize the artifact influence and the interference of atmospheric pollutants, LOPAP adopts an external sampling module without an inlet tube and two stripping coils connected in series. Heland et al. (2001)[59] and Kleffmann et al (2008)[102] had conducted a systematic investigation to verify the reliability of LOPAP for measuring atmospheric HONO, finding that LOPAP indeed possessed the ability to resist to interference from other pollutants (such as $NO_2$, $SO_2$, PAN, etc.). Nowadays, LOPAP has been considered as the interceder for judging the reliability of different methods in field HONO comparison measurements. For example, the 42% lower HONO concentration measured by the GAC than by LOPAP during nighttime at the sampling site of Kaiping, Guangdong province, was ascribed to the artificial influence of the long inlet tube of the GAC[103].

## 1.4 HONO measurements in the NCP region

The air pollution in the NCP, including summertime $O_3$ pollution and wintertime haze pollution, is still a severe environmental problem that needs to be improved urgently[104–118]. Meanwhile, high HONO levels were also frequently observed by field campaigns in the NCP. However, HONO measurement in the NCP was relatively late. Since 2000, scientists started to measure HONO in the NCP and most of them were in Beijing. In this section, measurements of HONO in the NCP will be summarized as follows:

To our knowledge, the first observation of HONO in the NCP occurred at an observation station in Peking University, led by Tang Xiaoyan’s group. They carried out the campaign in three periods from May to September of 2000, and found that the averaged value of HONO was 2-3 ppbv during the whole observation period. However, the study only reported the concentration levels and daily variations of HONO. The source has not been analyzed in this study[119].

Qin et al. (2006)[120] carried out HONO observation campaign in Beijing in the autumn of 2004. They observed HONO reached 6.1 ppbv and found that HONO had a good correlation with $NO_2$. HONO might come from the heterogeneous reaction of $NO_2$ and exhaust emissions.

Yang et al. (2014)[121] conducted field observation experiments at a suburban site in Beijing in the summer of 2006. Various species related to HONO, including radicals, were measured. The observation period was from August 18 to 31, 2006. During the period, two techniques, namely GAC and LOPAP, were used to measure HONO. Based on the observation, HONO measured by the two techniques showed the same trend and good correlation, but HONO from GAC was about 17% higher than LOPAP, which is because GAC was affected by the inlet. During the observation period, the concentration of HONO was between 0.03 and 3.7 ppbv. The highest value appeared in the morning and the lowest value occurred in the later afternoon. The observed HONO/$NO_x$ values range from 1.1% to 28.6%, with an average value of 7.5%, which was much higher than the HONO/$NO_x$ values from direct emissions, indicating that HONO originated mainly from secondary formation, rather than direct emissions. Based on HONO budget analysis, this study calculated the unknown source of HONO during the daytime and found that the known source (NO+OH, $NO+NO_2+H_2O$) was far from explaining the observed HONO during the daytime, and the unknown source strength was about 4 times of NO+OH. In addition, the correlation between the unknown source strength and $NO_2$ or $NO_2*J(NO_2)$ was poor, indicating that the photosensitized $NO_2$ reactions might not be the main source of the local unknown HONO formation. At the same time, the study found that HONO was the dominant source of primary OH, and its contribution was about three times of $O_3$ photolysis.

Zhu et al. (2009)[122] used DOAS to conduct HONO observations in Beijing in January 2007, and measured HONO as high as 7.5 ppbv. At the same time, they found that the observed HONO with $SO_2$ or $NO_x$ had a good correlation. The source of primary pollutants ($SO_2$, $NO_x$) was related to coal-burning during the heating season in Beijing. In the same year, the research group conducted a second campaign at the same location in August. The measured HONO showed an average of 0.8 ppbv, with a maximum of 4.0 ppbv. Besides, it was found that vehicle exhaust emissions contributed by about 15%

to HONO at night, and heterogeneous $NO_2$ reaction was the dominant source.

Spataro et al. (2013)[123] conducted two field campaigns in Beijing in the summer and the winter of 2017. The observed HONO concentration was in the range of 0.03-2.91 ppbv, and the HONO/$NO_x$ value was much higher than the HONO/$NO_x$ value from direct emissions, indicating an important contribution of secondary generation to the HONO budget. Nevertheless, based on the photo-stationary state, it was found that the homogeneous reaction of NO and OH was the most important source of HONO in winter. In the summertime, there was a strong unknown source that might come from the photoreduction reaction of $NO_2$ on the ground surfaces.

Hendrick et al. (2014)[124] carried out a four-year observation experiment in Beijing based on the MAX-DOAS technology. The campaign was conducted in urban Beijing area from July 2008 to April 2009, and in a rural site (Xianghe Station) near Beijing from March 2010 to December 2012. The article only reported data from 6:00 to 18:00 during the daytime. Most of the large values of HONO observed in the urban areas of Beijing and Xianghe Station appeared in the morning, with concentrations of 1.3-1.6 ppbv and 0.7-1.0 ppbv, respectively. Besides the discussion on the daily or seasonal variations of HONO, this study also discussed the contribution of HONO to OH and found that HONO was the dominant source of OH during most of the observation period. Although the study did not discuss the source of HONO, it could also be inferred that the value of HONO/$NO_x$ was much higher than that from direct emissions, indicating significant secondary HONO formation.

Wang et al. (2015)[125] carried out the HONO observation in Jinan. The observation period was from November 26, 2013 to January 5, 2014. MARGA (Monitor for AeRosols and Gases in ambient Air) was used to continuously measured gas-phase pollutants or particulate components such as HONO and particulate nitrite. Based on the nighttime observation, it was concluded that the HONO/$NO_x$ value from direct emissions was 0.42% -0.87%, with an average of 0.58%. During the experiment period, higher levels of particulate nitrite were observed. Due to the higher concentrations of alkaline substances such as ammonia ($NH_3$), more particulate nitrite rather than HONO, on the surface of particulate matter, was produced. And particulate nitrite on the aerosol surfaces could play a potential source of HONO during the daytime, especially on the surface of acidic particles with low ambient humidity.

Hou et al. (2016)[126] carried out a HONO observation campaign in the winter of 2014 in urban Beijing. During the observation period, it was found that the HONO concentration during the haze period was 0.49-3.24 ppbv, and the HONO concentration during the clean period was 0.28-1.52 ppbv. The HONO concentration and $PM_{2.5}$ showed a good correlation. However, when $PM_{2.5}$ reached up to a certain level (350 µg $m^{-3}$) or more, HONO concentration became relatively stable. Besides, based on photo-stationary state analysis, unknown source strength of HONO during the haze period was about 1.85 ppbv $h^{-1}$, which was higher than that during the clean period (1.26 ppbv $h^{-1}$).

Tong et al. (2016)[127] carried out HONO observation experiments at a urban site and a suburban site of Beijing in the winter of 2014. They found that the average concentrations of HONO at the urban and suburban sites were 1.34 and 0.79 ppbv during the haze period, and 0.54 and 0.44 ppbv during the clean period, respectively. By assuming a direct emission ratio of $HONO/NO_x$ = 0.8%, it was found that the direct emissions contributed accounting for 48.8% to atmospheric HONO in the urban site, which was more than the suburban site (10.3%). The heterogeneous conversion of $NO_2$ on the ground surface contributed more in the case of the suburban site than the urban site inferred from that the $HONO/NO_2$ at the suburb site was higher than that in the urban site. Based on an assumed OH concentration of $1\times10^6$ molecules $cm^{-3}$ and the measured NO, it was found that the homogeneous reaction of NO and OH at night was expected to have an important contribution to the production of HONO.

Wang et al. (2017)[128] carried out long-term observations in an urban site of Beijing. The observation period covered the autumn and winter of 2015 and the spring and summer of 2016. HONO was measured for one month in each. The average observed HONO concentrations in the four seasons of spring, summer, autumn, and winter were 1.05, 1.38, 2.27, and 1.05 ppbv, and $HONO/NO_2$ were 4.08%, 7.89%, 5.97%, and 7.04%, respectively. During the observation period, the $NO_2$ conversion rate during the night was 0.005 $h^{-1}$ to 0.01 $h^{-1}$, with an average value of 0.008 $h^{-1}$. The conversion of $NO_2$ was the main source at night. The observed daytime HONO could not be explained by HONO formation from homogeneous reaction and direct emissions, indicating strong unknown HONO sources. The strengths of the unknown HONO sources in the four seasons were 2.63, 3.05, 3.82, and 1.30 ppbv $h^{-1}$, respectively.

Li et al. (2018)[8] carried out 1-year HONO measurement in Jinan City, Shandong, from September 2015 to August 2016. This was the first time conducting a continuously one-year observation in the NCP reported in the literature. The average HONO concentration during the entire observation period was 1.28 ppbv, and the average

HONO concentrations observed during the four seasons of spring, summer, autumn, and winter at night were 1.24, 1.20, 0.87, 2.15 ppbv, respectively. High levels of HONO were also observed during the day, with average concentrations of 1.04, 1.01, 0.66, and 1.35 ppbv during the four seasons, respectively. The study used 12 fresh air masses to obtain a ratio of HONO/$NO_x$ from direct emissions, which was about 0.19%-0.87%, with an average value of 0.53%. Direct emissions at night contributed 12%-21% of the observed HONO. The nighttime conversion rate of $NO_2$ to HONO was 0.0068 $h^{-1}$. Based on the nighttime $NO_2$ conversion rate, the uptake coefficient of $NO_2$ on the surface (including the ground surface and aerosol surface) was calculated to be $6.1\times10^{-8}$- $1.7\times10^{-5}$, with a mean value of $1.4\times10^{-6}$. Based on the analysis of the HONO budget, direct emissions and homogeneous reactions could not explain the observed daytime HONO. The average HONO unknown strength was as large as 2.95 ppbv $h^{-1}$. Besides, it was found that the unknown source strength was well correlated with $J(NO_2)*[NO_2]$ (R=0.76), which was higher than the correlation with $J(NO_2)*[NO_2]*(S/V_a)$, suggesting that the photosensitized heterogeneous reaction of $NO_2$ on the ground surfaces might be a more important source of HONO than the reactions on the aerosol surfaces.

Xu et al. (2019)[129] carried out HONO observations in a rural site of Hebei province based on the IGAC technology. The observation period was from October 15 to November 25, 2016. The highest HONO concentration reached up to 17.6 ppbv, and the average value of HONO concentrations was 3.0 ppbv. During the observation period, it was found that the rapid increase of HONO concentration under severe fog and haze conditions might be related to the promotion of $NO_2$ reduction by $MH_3$ on the aerosol surfaces.

Zhang et al. (2019)[9] carried out HONO observations in Beijing in the winter of 2016. The observation time was from December 16, 2016, to December 23, 2016. During this period, a slightly polluted period, and a severely polluted period followed by a clean period were observed. It was found that concentrations of HONO during the haze period were significantly higher than that during the clean period, and the observed $NO_x$, an important precursor of HONO, during the haze period was also significantly increased. Based on the measured NO concentrations and an assumed OH concentration, it was found that the homogeneous reaction of NO and OH was expected to have an important contribution to nighttime HONO. Based on the nighttime observations of HONO and $NO_x$, it was inferred that the HONO/$NO_x$ ratio of direct emissions in the region was 1.3%, which showed a significant contribution to nighttime HONO. The study also found that under high humidity and high $PM_{2.5}$ conditions, HONO showed a relatively stable concentration, rather than an increasing trend, indicating that HONO might have a sink associated with particulate matter.

Besides field campaigns, various model studies[60,130–136] were also conducted to explore the HONO budget and its impact on regional air quality such as atmospheric visibility, SOA formation, $O_3$ pollution, particulate nitrate formation, etc.

Table 1.1 Summary of HONO measurements in the North China Plain.

| **Observation period** | **Location** | **Techniques** | **Mean ppbv** | **Max ppbv** | **Main source** | **Reference** |
|---|---|---|---|---|---|---|
| 5.15-9.12 2000 | Urban Beijing | SJAC-MOBIC | 2-3 | -- | --- | 119 |
| 8.24-9.5 2004 | Urban Beijing | DOAS | | 6.1 | $NO_2$ conversion, direct emission | 137 |
| 8.18-8.31 2006 | Suburban Beijing | GAC, LOPAP | ~0.8 | ~3.7 | NO+OH, unknown source | 121 |
| 1.19-2.8 2007 | Urban Beijing | DOAS | | 7.5 | | 122 |
| 8.14-8.24 2007 | Urban Beijing | DOAS | 0.8 | 4.0 | $NO_2$ conversion, direct emission | 138 |
| 1.23-2.14 2007 | Urban Beijing | Denuder-IC | 1.04 | 2.67 | $NO_2$ conversion, direct emission, NO+OH | 123 |
| 8.2-8.31 2007 | Urban Beijing | Denuder-IC | 1.45 | 2.91 | $NO_2$ conversion, direct emission, NO+OH, $pNO_3$ photolysis | 123 |
| 7.1 2008-4.30 2009 | Urban Beijing | MSX-DOAS | ~0.5[a] | 0.8[a] | -- | 124 |
| 3.1 2010-12.31 2012 | Suburban Beijing | MSX-DOAS | ~0.4[a] | 0.7[a] | -- | 124 |
| 11.6 2013-1.5 2014 | Urban Ji’nan | MARGA | 0.35 | ~3 | $NO_2$ conversion, direct emission | 125 |
| 2.22-3.2 2014 | Urban Beijing | LOPAP | | 3.24 | NO+OH, direct emission | 126 |
| 12.12-12.22 2014 | Urban Beijing | LOPAP | 1.34[b]/0.51[c] | ~4.0 | $NO_2$ conversion, direct emission, NO+OH | 127 |
| 12.12-12.22 2014 | Suburban Beijing | LOPAP | 0.79[b] /0.44[c] | ~1.5 | $NO_2$ conversion, direct emission, NO+OH | 127 |
| 9.22 2015-7.25 2016 | Urban Beijing | AIM-IC | 1.44 | ~8.0 | $NO_2$ conversion, unknown source | 128 |
| 9.1 2015-8.31 2016 | Urban Ji’nan | LOPAP | 1.15 | 8.36 | $NO_2$ conversion, direct emission | 8 |
| 10.15-11.25 2016 | Rural Hebei | IGAC | 3.0 | 17.6 | $NO_2$ conversion, direct emission | 129 |
| 12.16-12.23 2016 | Urban Beijing | LOPAP | 3.5 | 10.7 | NO+OH, direct emission, $NO_2$ conversion | 9 |

[a]: noontime observation, [b]: polluted conditions [c]: non-polluted conditions.

Even though field campaigns and model studies have already been conducted, HONO formation and its regional impact are still not well understood. On the one hand, unexpected high HONO mixing ratios observed in the NCP still cannot be well explained by the models with known HONO sources. On the other hand, different studies had different conclusions, and some of them were caused by the lack of measurements on important related parameters like radicals, boundary layer height, mixing layer height, etc. The estimation of related parameters may cause a discrepancy between different studies. Hence, comprehensive field campaigns with measurements on various parameters are still needed to be conducted in the future.

Therefore, this study selected a typical rural site in the North China Plain (NCP) where air pollution is still very severe compared to other regions in the world. HONO emissions from agricultural soil in the summertime and their impact on regional air quality were quantified by a chemistry transport model (The Community Multiscale Air Quality Modeling System, CMAQ). Besides, a comprehensive field campaign, including HONO measurement, was conducted at this rural site. A box model (Master Chemical Mechanism, MCM) was used here to explore HONO formation and its role in the formation of OH and particulate nitrate.

# Chapter 2 Development of a stripping coil-ion chromatograph method to measure atmospheric HONO

To summarize, this chapter described a stripping coil (SC) equipped with ion chromatograph (IC) to measure HONO, which was developed and assessed. Briefly, the reliability of the method mainly depends on the collection efficiency and the interference with other species. The performance of the method was assessed in the chamber using two kinds of absorption solutions, i.e., ultrapure water and 25 μM $Na_2CO_3$ solution under different concentrations of $SO_2$. Results indicated that HONO concentrations absorbed by ultrapure water and $Na_2CO_3$ solution were almost identical in the absence of $SO_2$ in the chamber, and both the collection efficiencies were more than 99%. However, the collection efficiency of ultrapure water decreased with the increase of $SO_2$, indicating that the presence of $SO_2$ resulted in the penetration of HONO during the sampling process in water. The collection efficiency kept more than 90% when the concentration of $SO_2$ was no more than 23 ppbv. Comparing with the situation without $SO_2$, HONO performed a remarkable increase with the presence of $SO_2$ when using $Na_2CO_3$ absorption solution, indicating the extra generation of HONO from the reaction between $SO_2$ and $NO_2$ in alkaline solution. Consequently, using ultrapure water as the absorption solution could provide a high collection efficiency and avoid the interferences from $SO_2$ when the concentration of $SO_2$ was below 23 ppbv. High correlations (slope=0.94~1.06, $r^2$>0.90) were found during the intercomparisons between SC-IC and other three techniques (two LOPAPs and one CEAS), suggesting the SC-IC method developed in this study was able to measure atmospheric HONO in the field campaigns.

This work has already been published in Xue et al. (2019)[139] Details are as follows:

## 2.1 Experimental

### 2.1.1 Technical setup of the SC-IC

In brief, the SC-IC system was based on the wet chemical method. Atmospheric HONO was absorbed by the absorption solution (ultrapure water or $Na_2CO_3$ solution) and converted to $NO_2^-$ in the liquid samples. $NO_2^-$ in the liquid samples was quantified by IC. Then the atmospheric HONO mixing ratio could be calculated by the gas sampling flow, liquid flow, $NO_2^-$ concentrations in the liquid samples, and atmospheric temperature.

As shown in Figure 2.1, the SC-IC device consists of three units: the sampling unit (part A), the transferring and supporting unit (part B), and the detection unit (part C). The sampling unit consists of a five-turn stripping coil (2 mm inner diameter), which is enclosed by a glass cylinder. The stripping coil has two inlets in the front (one for air and another is for absorption solution) and a gas-liquid separator. A small non-transparent box was used to cover the stripping coil to protect the SC and keep it away from sunlight with the air inlet stretching out the box for about 2 cm. A circulating water bath is used to keep the temperature of the stripping coil stable at 20±1 °C. Consequently, the sampling unit is conveniently movable. The sampling unit can be placed outside without inlet tubes in the field measurements, avoiding interference from the heterogeneous reaction on the surface of the inlet tubes.

The transferring and supporting unit consists of a dryer, a circulating water bath, a mass flow controller (MFC), an air membrane pump (KNF, Germany), two peristaltic pumps (Shenchen, China), a micro-filter, a glass bottle (1 L) for absorption solution, a 24-port valve and some sample bottles (20 mL). During the sampling process, the ambient air is drawn into the stripping coil by the air membrane pump. The air is absolutely mixed with the absorption solution supplied by the peristaltic pump and then the solution in the stripping coil is gathered in the gas-liquid separator. In the gas-liquid separator, the air is continually drawn through a dryer and an MFC and finally released as exhaust gas by the air membrane pump. The liquid is pumped through the micro-filter and the 24-port valve and collected in the sample bottles by another peristaltic pump. The MFC is weekly calibrated by a soap-foam flowmeter.

The detection unit consists of an anion chromatograph (WAYEE IC6200, China). Briefly, water-soluble ions ($F^-$, $HCOO^-$, $Cl^-$, $NO_2^-$, $NO_3^-$, $SO_4^{2-}$, etc.) are separated through a column (IC SI-52 4E, 4 mm ID × 250 mm) and then detected by a conductivity detector, respectively. The temperature for the column and detector is set to 25 °C and 40 °C, respectively. Its resolution time is 10 min. The detection limit for $NO_2^-$ is $2.5\times10^{-5}$ mg $L^{-1}$ based on N (3σ), equivalent to 4 pptv with a gas sampling flow of 2 L min and a liquid flow of 0.2 mL $min^{-1}$ for absorption solution. The concentration of atmospheric HONO is calculated from the concentration of liquid $NO_2^-$ based on the following equation[139].

$$[HONO]=\frac{\rho\times F_l\times V_m}{M\times F_g}\times10^3 \qquad (2.1)$$

[HONO]: HONO mixing ratio, ppbv

ρ: the concentration of $NO_2^-$ based on N in the liquidus samples, mg $L^{-1}$

$F_l$: the flow rate of the absorption solution, 0.2 mL $min^{-1}$

$V_M$: the molar volume of gas at the given temperature, 23.8 L $mol^{-1}$

M: the molar mass of nitrogen N, 14 g $mol^{-1}$

$F_g$: the flow rate of the gas, L $min^{-1}$

As the liquid volume for IC to analyze should be no less than 0.5 mL, the method we designed is able to meet the high time resolution (>2.5 min for one sample) for field measurements or laboratory researches.

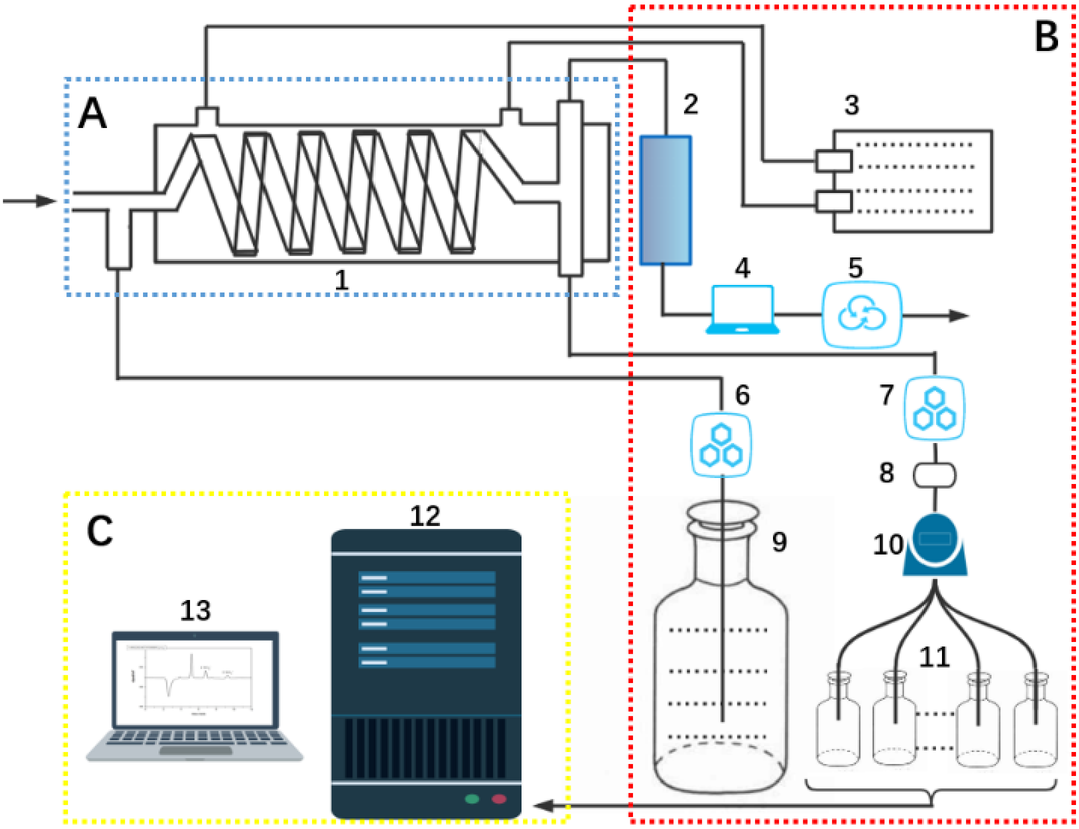

Figure 2.1 Schematic diagram of the SC-IC method. 1. Stripping coil. 2. Dryer. 3. Thermostatic water bath (20°C). 4. Mass flow controller. 5. Membrane air pump. 6. Peristaltic pump. 7. Peristaltic pump. 8. Filter. 9. Absorption solution. 10. 24-port valves. 11. Sampling bottles. 12. Ion chromatograph. 13. Computer.

### 2.1.2 Collection efficiency

Previous studies[140] have revealed that the equilibration between gas and liquid phase is established rapidly when the uptake coefficient $\gamma$ is more than 0.01, and thus mass transfer is diffusion controlled. The uptake coefficient of HONO ($\gamma_{HONO}$) is reported to be 0.05. Therefore, the ideal collection efficiency $\beta$ mainly depends on Henry's law shown in Eq (2.2)[92].

$$\beta=\frac{F_l H^* RT}{F_g+F_l H^* RT} \qquad (2.2)$$

where $F_l$, $H^*$, R, T, $F_g$ are the absorption solution flow (mL $min^{-1}$), effective Henry constant (M $atm^{-1}$), gas constant (L $mol^{-1}$ $K^{-1}$ atm), temperature (K) and gas flow (mL $min^{-1}$), respectively. H* is further defined as Eq (2.3).

$$H^*=H\times\left(1+\frac{K_a}{[H^+]}\right) \qquad (2.3)$$

where H is the Henry constant of HONO (49 M $atm^{-1}$), $K_a$ represents the ionization constant of HONO, and $[H^+]$ is the acidity of the absorption solution. Consequently, the collection efficiency mainly depends on the ratio $\alpha = F_g/F_l$ and the acidity. A proper α is needed because too large $F_g/F_l$ results in a low β and too small α one results in more residence time, which enlarges the potential interference from the heterogeneous reactions. Also, proper acidity is needed because high acidity (low pH) leads to a low β and low acidity (high pH) is in favor of the interference produced from heterogenous or multiphase reactions of $NO_2$.

Besides the ideal collection efficiency β, the measured $\beta_m$, obtained from two stripping coils connected in series, is defined in Eq (2.4).

$$\beta_m = (1 - \frac{[HONO]_{second}}{[HONO]_{first}}) \times 100\% \qquad (2.4)$$

### 2.1.3 Laboratory tests and field measurements

To explore the collection efficiency and potential interference of the sample system, laboratory researches have been conducted in a chamber. The chamber is made of Teflon film with a volume of 3.6 $m^3$. The temperature of the chamber is controlled to be 25 °C by an air conditioner. The chamber is inside a stainless box for light shielding to control the radiation in the chamber.

$N_2$ was introduced into the chamber first, and then standard gas of $NO_2$ was injected into the chamber to generate $NO_2$ concentration of 100 ppbv. Then, gradient concentrations of $SO_2$ (0-113ppbv) were achieved by injecting $SO_2$ standard gas orderly. Two stripping coils connected in series are used to collect HONO in the chamber. The impact on HONO collection efficiency from $SO_2$ can be reflected by the change of β.

To investigate the impact on HONO collection efficiency from different absorption solutions, the researches just mentioned before are conducted by two sample systems: one uses the ultrapure water as the absorption solution (H-method) and the other uses the 25 μ M $Na_2CO_3$ solution (N-method). The gas flow for sampling and the liquid flow for absorption solution are set as 2 L $min^{-1}$ and 0.2 mL $min^{-1}$, respectively. Four replicate samples for each sample system are collected. Each sample period lasts 5 min.

To explore the impact from particulate nitrite, atmospheric particles are collected on the quartz membrane by a particle sampler (Laoying, China) in Beijing from 3 January

2016 to 21 January 2016 during the winter field measurement. The sampling site is on the rooftop of a building in Research Center for Eco-Environmental Sciences, Chinese Academy of Sciences. The site is well documented by previous studies[128]. During the measurement, particles were collected every 2 hours at a sample flow of 100 L min$^{-1}$.

To test the performance of SC-IC on measuring atmospheric HONO in the field measurement, comparison researches were conducted with other methods including CEAS and two LOPAPs at the Station of Rural Environment, Chinese Academy of Sciences (SRE-CAS) located in DongBaiTuo village (38°71′N, 115°15′E), Hebei Province of China. LOPAP-1 was homemade by the Institute of Chemistry, Chinese Academy of Sciences. It has been proved to work well in many field measurements. The comparison with LOPAP-1 lasted from 13 June 2017 to 20 June 2017. LOPAP-2 was a commercial product of QUMA Elektronik & Analytik GmbH, Germany. The comparison with LOPAP-2 was conducted from 10 November 2017 to 22 November 2017. The CEAS was homemade by Anhui Institute of Optics and Fine Mechanics, Chinese Academy of Sciences. The comparison with CEAS lasted from 15 June 2017 to 22 June 2017. Note that both the sample inlets of SC-IC and CEAS were in a dynamic chamber which was serviced for measuring HONO emission flux from fertilized agricultural soil.

During the three comparisons, the SC-IC and LOPAPs ware calibrated by the same standard $NaNO_2$ solution. The CEAS was calibrated once per day. A 24-port valve (Figure 2.1) was used in SC-IC to achieve automatic collection, and the switching frequency was set at once per hour. Therefore, the hourly average of data from CEAS and LOPAPs were used for comparisons.

## 2.2 Results and discussion

### 2.2.1 Impact from $F_g/F_l$

Theoretically, the ideal collection efficiency decreases with the increase of $F_g/F_l$ (α) (Eq (2.2)). However, too small α results in long residence time, enlarging the influence of heterogeneous reaction. Hence, it needs to conduct field measurements to choose proper α. So, two stripping coils were connected in series to measure atmospheric HONO and ultrapure water was used as the absorption solution in a heavy haze winter day of Beijing. Six different sample flows (0.5-3 L min$^{-1}$) were set with $F_l$ at 0.2 mL min$^{-1}$, corresponding to α of 2500-12500. Considering the solubility equilibrium of atmospheric $CO_2$ in water, the pH of ultrapure water is 5.6. Then some studies used the 25 μM $Na_2CO_3$ solution to balance the equilibrium of atmospheric $CO_2$ (pH=6.9). Besides the measured collection efficiency $\beta_m$, the ideal collection efficiency at pH=5.6 ($\beta_{pH=5.6}$) and pH=6.9 ($\beta_{pH=6.9}$) was also calculated (Figure 2.2). It follows that HONO concentration in the second stripping coil under the sample flow above 2 L $min^{-1}$ (2.5 and 3 L $min^{-1}$) was obviously higher than that under the sample flow below 2 L $min^{-1}$, indicating that large airflow or $F_g/F_l$ (>12500) would result in high penetration proportion. While the concentrations of atmospheric $SO_2$ in each sample flow period were 12 (3 L $min^{-1}$), 11 (2.5 L $min^{-1}$), 14 (2 L $min^{-1}$), 11 (1.5 L $min^{-1}$), 14 (1 L $min^{-1}$) and 14 ppbv (0.5 L $min^{-1}$), respectively, the large penetration rate was not ascribed to the increase of $SO_2$ but the limited absorption time.

Although the collection efficiency was expected to be higher at low α values, $\beta_m$ was remarkably lower (<92%) than the ideal collection efficiency at the $F_l$ of 0.5 or 1.0 L $min^{-1}$ (α=2500 or 5000). On the one hand, a small gas flow might introduce more heterogeneous reactions, as discussed before. It was obvious that the absorption solution in the stripping coil distributed quite inhomogeneously either at a large $F_g$ (>2 L $min^{-1}$) or low $F_g$ (<1.0 L $min^{-1}$), the effective collision between gas molecules and liquid surface reduced sharply, resulting in a low $\beta_m$. Besides, the disturbance in the inhomogeneous situation caused the distinctly significant fluctuation (error bars) of the collection efficiency (Figure 2.2).

Compared with the situation under other sample flows, the sampling system showed better performance with the sample flows of 1.5 and 2 L $min^{-1}$. It can not only collect HONO at a high collection efficiency of more than 94.1% but also possess a short residence time (about 0.1 s) to avoid the heterogeneous contribution. Therefore, the sample flow of 1.5~2 L $min^{-1}$, corresponding to the $F_g/F_l$ of 7500-10000, was recommended to accurately measure atmospheric HONO for the SC-IC method.

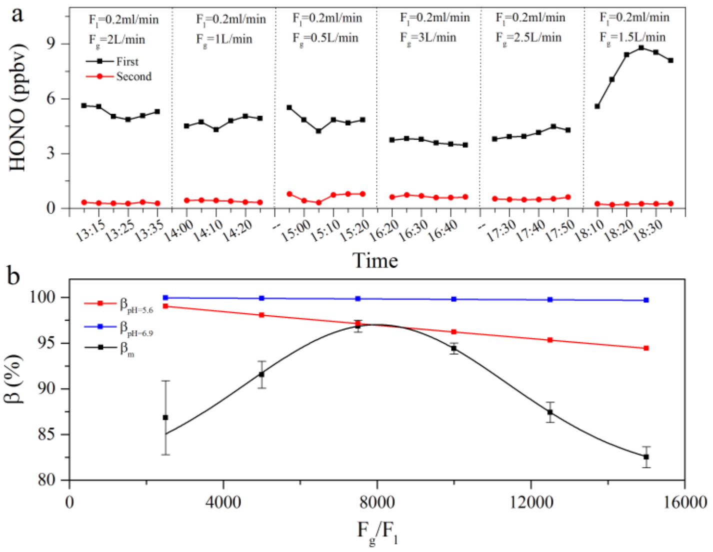

Figure 2.2 The impact on HONO collection efficiency from $F_g/F_l$. a. HONO concentrations in the first (black square) and second (red circle) stripping coils. b. The measured collection efficiency ($\beta_m$, black square), the ideal collection efficiency at pH=5.6 ($\beta_{pH=5.6}$, red square) and pH=6.9 ($\beta_{pH=6.9}$, blue square).

### 2.2.2 Impact from $NO_2$ and $SO_2$

Two stripping coils connected in series were used in the chamber experiments to assess the collection efficiency. The collection efficiency and the concentrations of HONO in the two stripping coils were measured when the chamber was filled with $N_2$ and 100 ppbv $NO_2$ with different concentrations of $SO_2$. HONO concentration in the chamber filled with $N_2$ was less than 5 pptv (Figure 2.3A). However, when $NO_2$ standard gas was injected into the chamber to get its concentration up to 100 ppbv in the chamber, averaged HONO concentration of 20 samples reached up to 2.235±0.027 ppbv, indicating that the injection of $NO_2$ increased HONO in the chamber. Due to the small Henry constant ($9.87\times10^{-8}$ mol $L^{-1}$ Pa at 25 °C in water) of $NO_2$, the concentrations of $NO_2$ in the first and second stripping coils were almost the same. However, HONO in the first stripping coil was two orders of magnitude larger than that in the second, suggesting that the contribution from $NO_2$ reactions on the surface, including heterogeneous reactions to the measured HONO was negligible. Therefore, the increase of HONO after injecting $NO_2$ was ascribed to two potential reasons: 1) HONO existed in the standard gas, and 2) HONO was produced from the $NO_2$ heterogeneous reactions on the chamber wall. Cheng et al. (2013)[128] used dynamic dilution to achieve 200 ppbv

$NO_2$ and found only 4 pptv HONO in the airflow measured by the SC-IC method, indicating that HONO came from the heterogeneous reaction of $NO_2$ on the chamber wall. If the reaction worked continuously, HONO would increase with the reaction time. Whereas, HONO concentration kept stable during a long period (>120min) after injecting $NO_2$, suggesting a large initial uptake coefficient and a small uptake coefficient when the gas was well mixed. In addition, HONO concentrations measured by H-method or N-method were almost identical after injecting $NO_2$, and the penetration rate was less than 1% (Figure 2.3B), indicating that both methods were able to collect HONO with high collection efficiency in this condition.

Compared with the situation when only $NO_2$ was injected into the chamber, HONO concentrations in the first stripping coil increased remarkably using N-method but decreased gradually using H-method after $SO_2$ was injected into the chamber (Figure 2.3A). Previous researches have demonstrated that $NO_2$ could oxidize $SO_2$ on the liquid surface through heterogeneous reaction or multiphase reaction with the production of HONO (Eq (2.5)). The reaction was in favor of alkaline conditions such as the high ammonia areas.

$$2NO_2\ (g)+SO_2\ (g)+2H_2O\ (aq)\rightarrow 2HONO\ (g)+2H^{+}(l)+SO_4^{2-}(l) \qquad (2.5)$$

Obviously, in the situation where certain concentrations of $NO_2$ and $SO_2$ co-existed, HONO concentration would be overestimated because of the HONO production from Eq (2.5), especially for N-method. Even if the penetration percent of H-method increased with the concentration of $SO_2$, it was no more than 8% when $SO_2$ was below 23 ppbv. When $SO_2$ in the chamber reached up to 113 ppbv, the concentration of HONO in the first stripping coil in N-method was consistent with the initial HONO detected just after injecting $NO_2$, which would be ascribed to the decrease of HONO production and the increase of penetration percent. $SO_2$, as a kind of acid gas, can neutralize the alkalinity of the absorption solution. On the one hand, high concentration of $SO_2$ reduced the heterogeneous production of HONO; on the other hand, it reduced the solubility of HONO, resulting in a high penetration percent (Figure 2.3). Therefore, it was a coincidence that HONO in the first stripping coil in N-method was consistent with the initial HONO concentration. Cheng et al. have also explored the impact of $SO_2$ on HONO measurement using the SC-IC method, and they found the impact can be neglected. Note that their result only based on the situation when 100 ppbv $SO_2$ and 300 ppbv $NO_2$ were co-existed. However, our research found that the heterogeneous production of HONO can be just counteracted by the penetration with $SO_2$ concentration of 113 ppbv and $NO_2$ concentration of 100 ppbv.

In the typical polluted areas, including Beijing, the concentration of $SO_2$ is usually about several ppbv in summer and tens of ppbv in winter. Based on our research, H-method has the capacity to carry on HONO field measurements in the typical polluted areas of China. The method can not only provide a high collection efficiency but also reduce the interference from the co-existence of $SO_2$ and $NO_2$. In addition, the study recommended that systematic assessments about the absorption efficiency and potential interference should be conducted when using wet chemical methods to detect HONO.

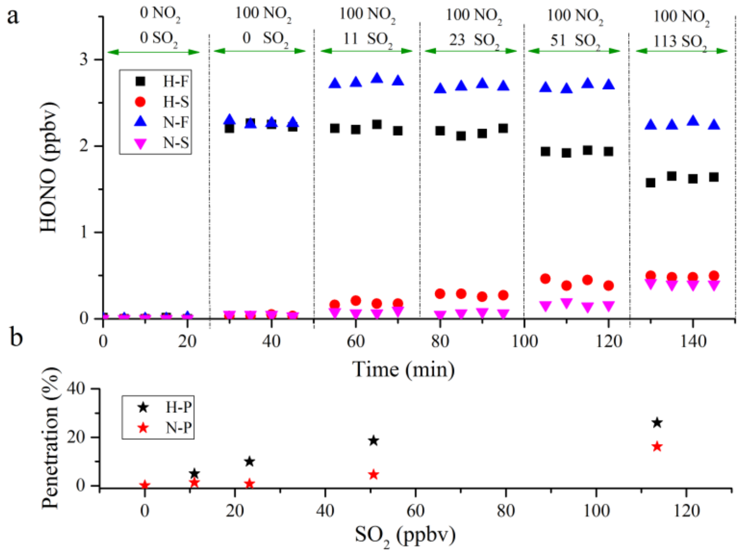

Figure 2.3 The impact of $SO_2$ and $NO_2$ on laboratory HONO measurement. a. HONO concentrations in the chamber detected by SC-IC. H-F and H-S: HONO in the first and second stripping coil detected by H-method. N-F and N-S: HONO in the first and second stripping coil detected by N-method. b. the penetration percent of H-method (H-P) and N-method (N-P).

### 2.2.3 Particulate nitrite and storage time

Besides the factors mentioned above, the method of SC-IC to measure HONO might be influenced by atmospheric particulate nitrite. We synchronously sampled atmospheric particles during the HONO field measurement from 7 January 2016 to 23 January 2016. After analyzing the particulate nitrite, we found that the hourly average concentration was 0.045±0.021 μg $m^{-3}$, equivalent to 0.022±0.010 ppbv of atmospheric HONO. Particulate nitrite just took less than 1% of atmospheric HONO, suggesting that the influence from particulate nitrite on HONO measurement was neglected even if all the particulate nitrite was absorbed by the absorption solution.

As our samples are collected by offline method, they will be stored for some time (usually less than 10 days) before analysis. We explored the impact of storage time on HONO measurement. We collected HONO using H-method and conducted the analysis immediately. Liquid samples were kept hermetic and stored in a refrigerator at 4 °C for 11 days (264 hours). After that, HONO in the samples was analyzed again to compare with that before storage with the results shown in Figure 2.4A. It's evident that HONO concentrations before and after storage show a high correlation (slope=1.005, $r^2$=0.997), suggesting that the liquid sample possesses enough chemical stability for at least 11 days when kept at 4 °C.

In addition, to explore the stability of the sample in the environmental temperature, we picked 12 samples with different HONO concentrations from the campaign in winter 2015/2016. We analyzed them every 2 hours in 24 hours (Figure 2.4B). Results showed that HONO performed no significant variation in all the samples. Statistical analysis revealed that the relative standard deviation was less than 14.3% when HONO concentration was below 0.2 ppbv and less than 1.7% when HONO concentration was more than 0.2 ppbv. The variation might be caused by the uncertainty of detecting $NO_2^-$ by the ion chromatograph rather than the storage time.

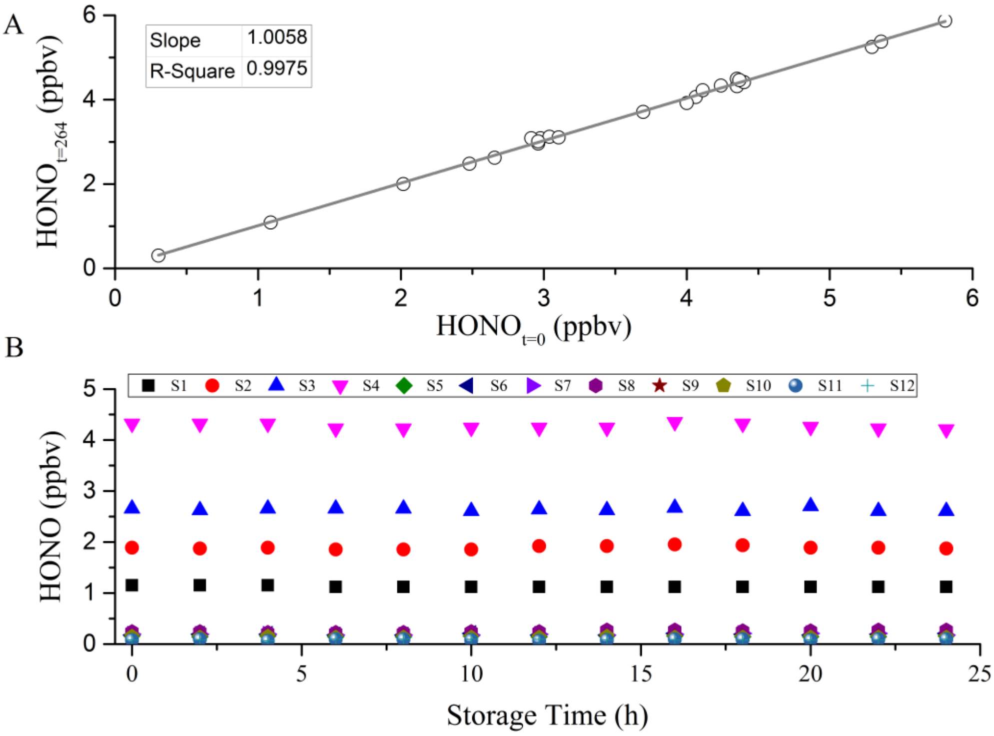

Figure 2.4 The variation of HONO concentration in the liquid samples with the storage time. A. Variations of HONO concentrations before and after storage for 11 days (264 hours) at 4 °C. B. Variations of HONO concentrations in 24 h.

### 2.2.4 Intercomparisons

To further evaluate the reliability of the SC-IC developed in this study, field comparisons between the SC-IC and the methods of LOPAP and CEAS were conducted. As shown in Figure 2.5, the levels and the variations trends of HONO measured by the SC-IC were in good agreement with those measured by the LOPAP-1 (Figure 2.5a), LOPAP-2 (Figure 2.5b) and CEAS (Figure 2.5c) during the three measurement periods, which could be reflected by the significant correlations (slopes≈1 and $r^2$ >0.90) between the HONO concentrations measured by SC-IC and the other two methods (Figure 2.5d). The approximately same parameters (Mean, Median, Standard Deviation, Minimum, Maximum) from the summary statistics (Table 2.1) for each comparison revealed that the SC-IC method developed in this study was able to measure atmospheric HONO from low concentration (0.1 ppbv) to high concentration (14 ppbv).

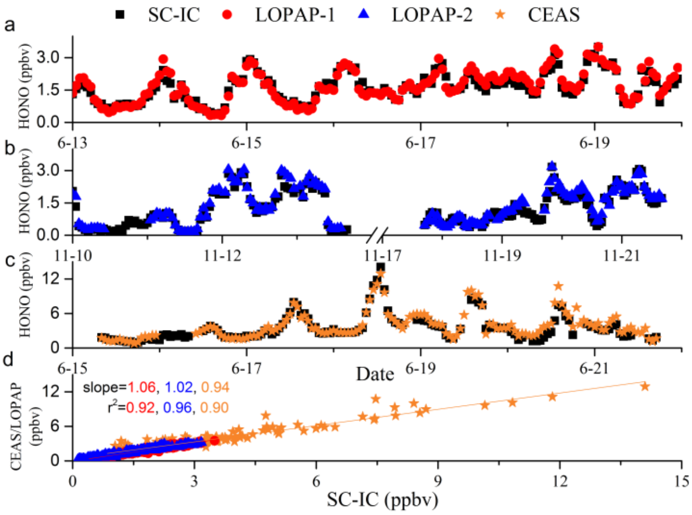

Figure 2.5 Time series of HONO concentrations measured by SC-IC and other different methods during three periods and their correlations.

Table 2.1 Summary statistics of HONO concentrations measured by different methods in the common measurement period ($^{a}$: data measured from 13 June 2017 to 20 June 2017. $^{b}$: data measured from 10 November 2017 to 22 November 2017. $^{c}$: data measured from 15 June 2017 to 22 June 2017).

| Methods / Parameters | SC-IC$^{c}$ | CEAS | SC-IC$^{a}$ | LOPAP-1 | SC-IC$^{b}$ | LOPAP-2 |
|---|---|---|---|---|---|---|
| Obs | 135 | 135 | 168 | 168 | 159 | 159 |
| Mean | 3.52 | 3.82 | 1.62 | 1.68 | 1.33 | 1.42 |
| Median | 3.05 | 3.27 | 1.63 | 1.66 | 1.32 | 1.34 |
| Std. Dev | 2.30 | 2.35 | 0.65 | 0.72 | 0.80 | 0.83 |
| Min | 0.85 | 0.82 | 0.40 | 0.32 | 0.12 | 0.15 |
| Max | 14.10 | 12.93 | 3.50 | 3.51 | 3.17 | 3.18 |

The normalized differences (ND) value has been used in field tests of different methods for measuring one atmospheric pollutant. To quantitatively study the difference between SC-IC and LOPAPs, we calculated the ND values for the two comparisons of SC-IC and LOPAPs[95,141].

$$ND_{ij}=\frac{C_i-C_j}{C_i+C_j} \qquad (2.6)$$

where $C_i$ and $C_j$ represent HONO concentrations measured by SC-IC and one of the LOPAPs. The ND values with HONO concentrations measured by SC-IC were shown in Figure 2.6. In addition, the coefficients of divergence (CD)[95,141], a normalized parameter of similarity between two time-series of data, were also shown in Figure 2.6.

$$CD_{ij}=\sqrt{\left(\left(\frac{1}{p}\right)\times\sum ND_{ij}^{2}\right)} \qquad (2.7)$$

where p is the number of the observations, and $ND_{ij}$ is already defined above. Briefly, the CD values arrange from 0 to 1, indicating that the two time-series of data are from absolutely the same to completely different. The relatively small CD values for SC-IC and LOPAP-1, SC-IC and LOPAP-2 and SC-IC and CEAS were 0.067, 0.096 and 0.137, respectively (Figure 2.6), proving that HONO concentrations measured by SC-IC fitted well with that measured by other methods. Also, this proved that the three methods were in good operation and calibration. Additionally, the ND values for SC-IC and LOPAP-1, SC-IC and LOPAP-2, and SC-IC and CEAS were in the range of ±0.15, ±0.35 and ±0.48, respectively (Figure 2.6), which were comparable to previous studies about comparisons of atmospheric HONO measurement methods. As shown in Figure 2.6a to c, The ND values became convergent with the increase of HONO concentrations, suggesting good agreement of SC-IC with other methods at high HONO levels. The ranges of ND values for SC-IC and LOPAP-1 (LOPAP-2) were among ±0.13 (±0.21) when HONO concentrations were beyond 0.2 ppbv, confirming the preceding inference.

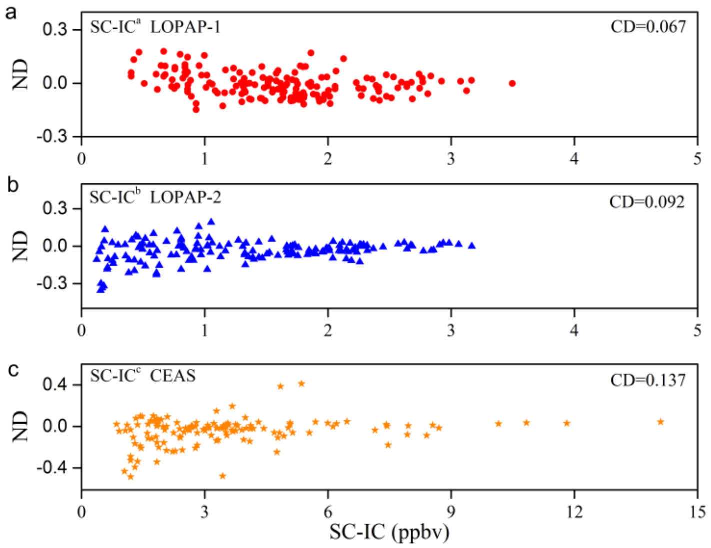

Figure 2.6 ND (Normalized difference) values between SC-IC and other methods in the common measurement period. Also shown is the corresponding CD (coefficient of divergence) values.

Considering the important role of HONO in the daytime, attention should also be paid to the comparison of HONO measured by different methods in low HONO conditions. Additionally, many previous researches have conducted comparisons of different methods in detecting low HONO concentrations. Their results indicated various methods still undergo large differences, while LOPAP was able to detect low HONO concentrations. In the field comparison of SC-IC and LOPAP-2, minimum (daytime) atmospheric HONO concentrations were low to about 0.1 ppbv (Figure 2.6, Table 2.1). In the condition with low HONO concentrations (<0.2 ppbv), most of the ND values were in the range of ±0.22, indicating that SC-IC and LOPAP-2 fitted well even in low HONO conditions.

## 2.3 Summary

An SC-IC method using ultrapure water as the absorption solution was developed and promoted to measure atmospheric HONO. The detection limit and time resolution could reach 4 pptv and in 2.5 min. Chamber studies proved that wet chemical methods, especially those using alkaline absorption solutions, might suffer from small interference from the co-existence of $SO_2$ and $NO_2$. HONO might be overestimated in low $SO_2$ conditions and underestimated in high $SO_2$ conditions with the existence of $NO_2$. Our study showed that the SC-IC method using ultrapure water as the absorption solution was able to collect atmospheric HONO and avoided interference from the co-existence of $SO_2$ and $NO_2$ in typical pollution areas. Statistical analysis of the field comparisons of SC-IC with CEAS or two LOPAPs also confirms the reliability of SC-IC to be applied in the field measurements. Here we recommend that wet chemical methods, especially those using alkaline or neutral solutions as the absorption solutions, need to be systematically assessed for the interference from atmospheric pollutants.

# Chapter 3 Development of a twin open-top chambers method to measure soil HONO emission flux

This chapter describes the development and assessment of a twin open-top chambers (OTCs) method to measure HONO emission flux from agricultural soil. One of the chambers with its bottom covered by Teflon film (designated as the reference chamber), the other one with its bottom covering the agricultural soil (designated as the experimental chamber). The possible formation or absorption of HONO on the wall of the twin chambers could be largely eliminated through subtraction of the HONO concentrations in the reference chamber from those in the experimental chamber for HONO flux measurements. The performance of the OTCs system was tested under laboratory conditions and field measurement conditions. The interference from the wall effect, the greenhouse effect, and photolysis were rationally discussed. Field tests on the performance of the OTCs system before and after fertilization were conducted at a rural site in the NCP. Results revealed that agricultural soil before fertilization was an important source for HONO. Before fertilization, the emission fluxes showed radiation-dependent or temperature-dependent variation, with a maximum up to 3.21 ng N $m^{-2}$ $s^{-1}$ at noontime. The fertilization process substantially accelerated HONO emissions, and unexpectedly strong HONO emission fluxes after fertilization were observed, which was rationally attributed to biological processes, including nitrification. Considering the large fertilization rate in the NCP and similar regions, HONO emission from agricultural soil may have an enormous impact on regional photochemistry and air quality. More research, especially HONO emission flux measurement after fertilization, was expected to be conducted in this aspect.

This chapter focuses on the performance of the OTCs system and analysis of soil HONO emissions and their regional impact is described in the next chapter.

This work has already been published by Xue et al. (2019)[142]. Details are as follows:

## 3.1 Experimental

### 3.1.1 Twin open-top chambers method (OTCs)

The OTCs system consists of two chambers: an experimental chamber (Exp-chamber) and a reference chamber (Ref-chamber). Both the two chambers are continuously flushed by ambient air, and the Exp-chamber covers the soil, but the Ref-chamber does not. Then soil HONO emissions can be inferred from the difference of HONO concentrations in the two chambers.

As is shown in Figure 3.1, the OTCs system consists of two chambers: an experimental chamber (Exp-chamber) and a reference chamber (Ref-chamber). The only difference between the two chambers is that the Exp-chamber consists of an underground part and an aboveground part while the Ref-chamber consists of only the aboveground part. The underground part of the Exp-chamber is a stainless cylinder pedestal (inner diameter, ID: 32cm), which is inserted into the soil (down to 15 cm deep).

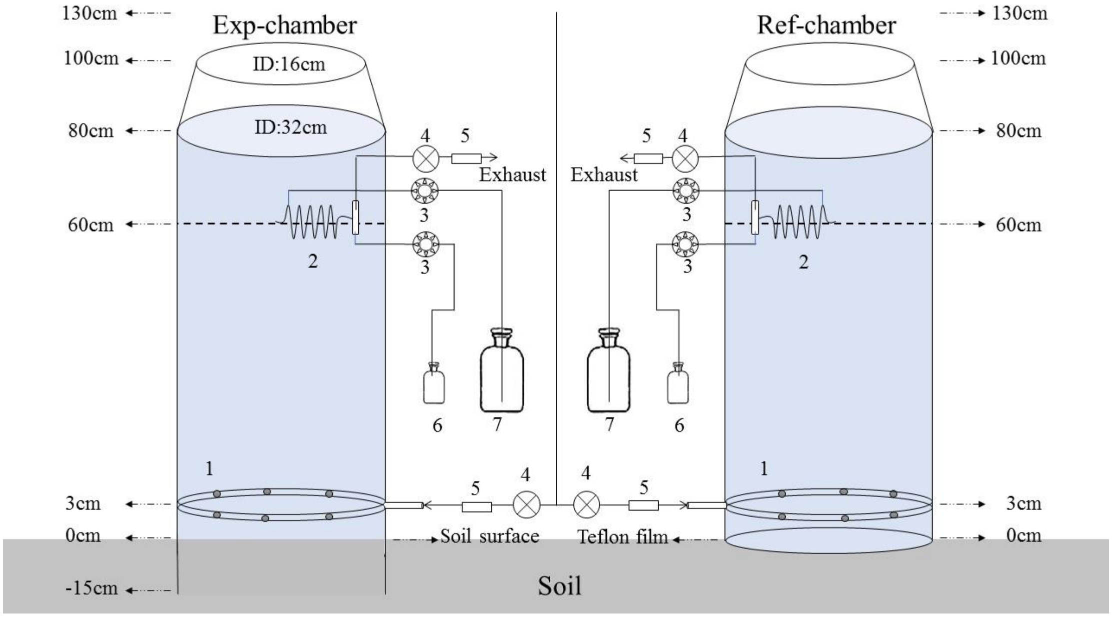

Figure 3.1 Structural diagram of the twin open-top chambers. 1. Stainless collar. 2. Stripping coil. 3. Peristaltic pump. 4. Air pump. 5. Flow regulator. 6. Sample bottle. 7. Absorption solution bottle. Heights of some parts of the chambers are also shown on the left and right of the diagram (the height of the soil surface is treated as zero).

The aboveground part is a stainless bracket (inner diameter: 32 cm) which consists of six stainless tube (height: 80 cm, outer diameter: 1 cm) and three cycle rings (ID: 32 cm, 32 cm and 16 cm). The tops of the six tubes for the experimental chamber are welded on a cycling ring (ID: 32 cm). The bottom of the aboveground part of the Exp-chamber is welding on the cylinder pedestal. Both the tops and the bottoms of the six tubes for the reference chamber are welded on cycle rings (ID: 32 cm), respectively. The bottom of the Ref-chamber is sealed by Teflon film.

For both chambers, about 20 cm above the top cycle ring, another cycle ring (ID: 16

cm) is fixed on the top. All the aboveground parts are covered by Teflon film., A Stainless collar with six holes horizontally facing toward the center is fixed in the chamber at the height of 3cm. Atmospheric gas was pumped into the chambers through the collars to flush the chamber from the bottom (soil surface) to the top. The flushing gas was sprayed through the six holes on the collar like a fan, which can mix well with the emitted gas in the chamber. The flow for the flushing gas is controlled at 20 L $min^{-1}$ by a flow regulator. The regulators are calibrated by a soap flowmeter twice per day. So, the flushing air sweeps the soil surface covered by the chamber and mixes with gases emitted from soil, and finally over brims from the upper ring. The reduction of the inside diameter of the upper ring can avoid the interference from the outside atmosphere. Stripping coils without any inlets for HONO measurement are fixed at the height of 60 cm inside of the chamber. Therefore, the soil emission flux can be obtained by the difference of HONO concentrations in the two chambers[142].

$$F_{HONO\text{-}N}=\frac{(C_{Exp}\text{-}C_{Ref})\times F_{flush}\times M_N\times P}{R\times T\times S}\times\frac{1}{60} \quad (3.1)$$

$F_{HONO\text{-}N}$: HONO emission flux based on N, ng N $m^{-2}$ $s^{-1}$;

$C_{Exp}$: HONO concentration in the Exp-chamber, ppbv;

$C_{Ref}$: HONO concentration in the Ref-chamber, ppbv;

$F_{flush}$: flushing flow, L $min^{-1}$;

$M_N$: molar mass of N, g $mol^{-1}$;

P: air pressure, kPa;

R: ideal gas constant, L kPa $mol^{-1}$ $k^{-1}$;

T: thermodynamic temperature, K;

S: area of the soil covered by the chamber, $m^{-2}$.

### 3.1.2 HONO collection and analyzer

HONO was measured by a wet chemical method, which was detailed in the introduction by the previous chapter. Briefly, HONO is absorbed by ultrapure water in the stripping coil and collected automatically in glass bottles (20 mL) with a sampling period of one hour for one sample. The gas flow and absorption solution flow were set at 2 L $min^{-1}$ and 0.2 mL $min^{-1}$, respectively. The gas flow and liquid flow were calibrated once per day. Two systems of the wet chemical method were continuously working in both Exp-chamber and Ref-chamber. The liquid samples were stored in a refrigerator at 4°C analyzed by an ion chromatograph in no more than one week.

### 3.1.3 Laboratory research about the performance of OTCs

We tested the performance of the OTCs system in laboratory research by giving a specific NO flux. During the investigation, NO standard gas was introduced into the bottom of the chamber through a right-angle Teflon tube (ID: 1.5 mm) that was designed only for laboratory tests, not field campaigns. The shortest side of the tube was horizontally installed at the bottom of the Ref-chamber. The length of the shortest side of the tube was 32 cm, the same as the ID of the chamber, which could guarantee the homogeneous distribution of emission sources inside the chamber. Six holes were evenly distributed on the shortest side while the outlet of the shortest side was blocked by a knot. The longish side of the right-angel tube was connected to a mass flow controller (range: 0-50 mL $min^{-1}$), which controls the flow from the NO standard gas at the bottom of the chamber. High purity nitrogen (>99.999%) was used as the flushing gas at the flow of 20 L $min^{-1}$. Therefore, the NO standard gas was emitted from the bottom of the chamber through the six holes on the right-angle tube, which can represent soil nitrogen gas emission. NO was measured at the height of 60cm in the chamber by a NO-$NO_x$ analyzer (Thermo Fisher Model 42i, NO-$NO_2$-$NO_x$ analyzer, USA).

### 3.1.4 Site description

As shown in Figure 3.2, the field experiments were carried out at the Station of Rural Environment, Chinese Academy of Science (SRE-CAS), which is located in an agricultural field in Wangdu County, Hebei Province of China. Winter wheat and summer maize have been cultivated for several decades in the field. The soil pH (in a 1:2.5 soil to water), organic C and total N were 8.1, 8.34-9.43 g $kg^{-1}$ and 1.02-1.09 g $kg^{-1}$, respectively. The annual rainfall at this site is about 555 mm, and the annual temperature is about 12.3 °C. The highest temperature of about 26.5 °C and the lowest temperature of about -4.1 °C occurred in July and January, respectively.

Many previous studies about $N_2O$, $NH_3$, and NO emission from agricultural soil have been conducted at this site[143–146]. For example, Zhang et al. (2012) and Zhang et al. (2016)[143,144] found that nitrification was the predominant process for NO and $N_2O$ emission in the NCP. During the nitrification process, $NH_4^+$ was transferred to $NO_3^-$ with the intermediate production of $NO_2^-$ and $H^+$, which was a potential source of HONO. Besides, nitrogen fertilizers (mainly ammonium fertilizer) are widely used in the NCP, which exacerbates reactive nitrogen gas emission from soil.

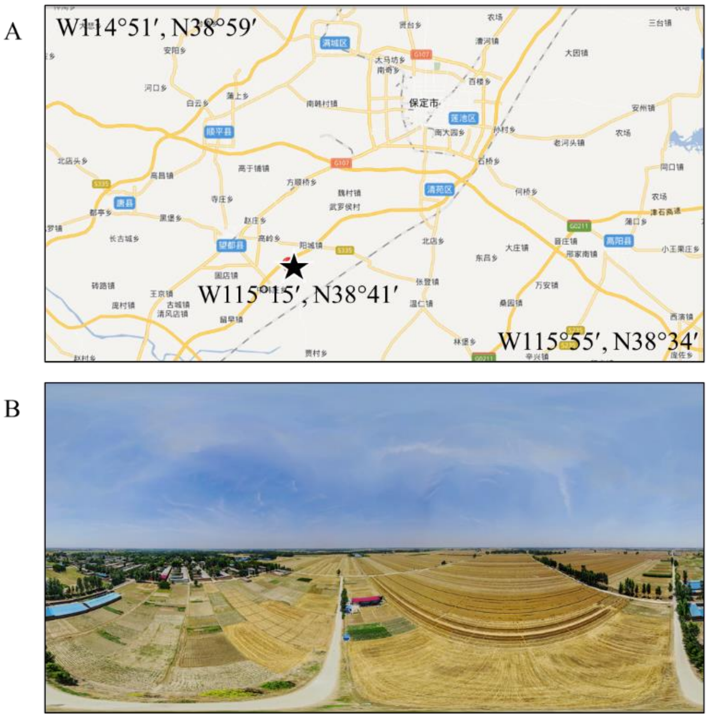

Figure 3.2 Location of the SRE-CAS station (part A, black star) and an aerial view of the measurement site after wheat harvest (part B). In part A, the longitudes and latitudes of the northwest and southeast of the intercepted map were shown in the graph. In part B, the station located at the building with a red rooftop, which was surrounded by agricultural soil and small villages.

During the pre-experiment in 2015, we tested the performance of the OTCs system to measure soil NO emission and soil HONO emission before and after the fertilization process. We measure the gradient concentrations of NO in the Exp-chamber after fertilization by two NO-$NO_x$ analyzers (Thermo Fisher Model 42i, NO-$NO_2$-$NO_x$ analyzer, USA) and the atmospheric NO concentration by a NO-$NO_y$ analyzer (Thermo Fisher Model 42i-Y, NO-$NO_y$ analyzer, USA). Two temperature and RH recorders (Apresys USB Temperature and RH Data Logger 179-UTH, USA) were used to measure the temperature and RH inside and outside of the Exp-chamber in the pre-experiment. We also conducted two field measurements of soil HONO emission fluxes in the summers of 2015 and 2017 when planting maize. In this chapter, we just report about the performances of the OTCs and the preliminary results in the pre-experiment with the aim of testing the OTCs system. More measurements and analysis of the HONO emission flux will be discussed in the next chapter.

## 3.2 Results and discussion

### 3.2.1 Performance of the OTCs system in the laboratory research

Figure 3.3 shows the time series of NO concentrations in the chamber during eight steps. At the beginning of the experiment, only flushing gas ($N_2$) was introduced into the chamber. NO concentrations in the chamber kept stable at zero, suggesting good calibration of the NO analyzer and the negligible interference from outside of the chamber when the atmospheric NO concentration was about 20 ppbv measured 10 min before the experiment. When the NO was introduced into the chamber (step 1), the NO concentrations in the chamber increased quickly and reached a constant value in about 4 min. From step 1 to step 4, NO flux was gradually increased by enlarging the flow of the standard gas, while NO concentration always reached 90% of the consistent value in 4-6min with an average of 4.5 min. From step 5 to step 8, NO flux was gradually decreased. At the same time, NO concentration always reached 90% of the consistent value in 4-7min with an average of 5.25 min, which suggested that the chamber was able to respond quickly to the increase or decrease of soil emission.

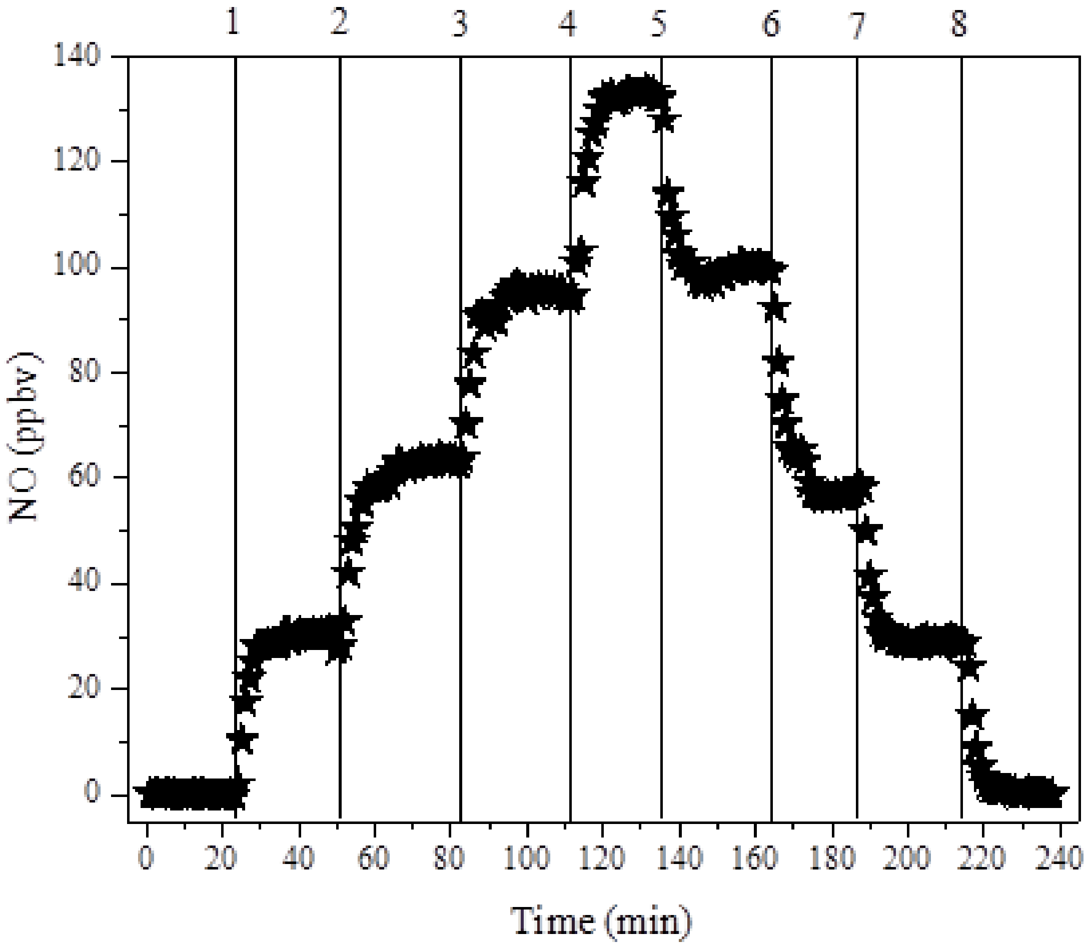

Figure 3.3 NO concentrations in the Ref-chamber during laboratory research. The vertical lines indicate experimental steps1-8. 1 (23 min): $F(NO)_{given}$=90.7 ng $m^{-2}$ $s^{-1}$ was set; 2 (51min): $F(NO)_{given}$=181.4 ng $m^{-2}$ $s^{-1}$; 3 (83 min): $F(NO)_{given}$=181.4 ng $m^{-2}$ $s^{-1}$; 4 (112 min): $F(NO)_{given}$=181.4 ng $m^{-2}$ $s^{-1}$; 5 (136 min): $F(NO)_{given}$=181.4 ng $m^{-2}$ $s^{-1}$; 6 (164 min): $F(NO)_{given}$=181.4 ng $m^{-2}$ $s^{-1}$; 7 (187 min): $F(NO)_{given}$=181.4 ng $m^{-2}$ $s^{-1}$; 8 (214 min): $F(NO)_{given}$=181.4 ng $m^{-2}$ $s^{-1}$.

In addition, the measured NO fluxes had significant correlations with the given NO fluxes (slope=0.918, $r^2$=0.998), which is graphically shown in Figure 3.4. The excellent correlation suggested that the emitted NO mixed well with the flushing gas in the chamber, which indicated that the chamber was able to quantify soil reactive nitrogen gas, including NO and HONO emission.

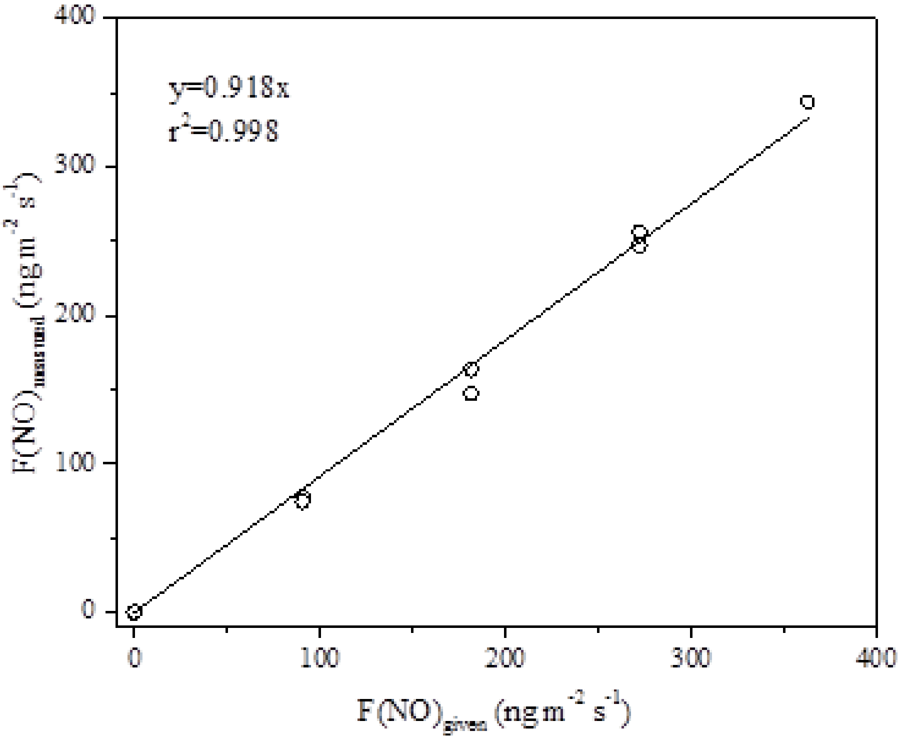

Figure 3.4 Correlations between given NO fluxes and measured NO fluxes based on N.

### 3.2.2 Performance of the OTCs system in the field test

Besides the laboratory research to test the OTCs system, measurement of gradient NO concentrations in the Exp-chamber over the fertilized soil was conducted to confirm the performance of the OTCs system. As is shown in Figure 3.5, both the NO concentrations at 45 cm ($H_{45}$-NO) and 60cm ($H_{60}$-NO) were higher than atmospheric NO concentration, suggesting that the fertilized soil emitted NO to the atmosphere based on the hypothesis that NO in the Ref-chamber was consistent with atmospheric NO. $H_{45}$-NO and $H_{60}$-NO exhibited the same variation trend and high correlation (slope=0.94, $r^2$=0.73), suggesting that NO was homogeneously mixed between the height of 45cm and 60cm. The difference between $H_{45}$-NO and $H_{60}$-NO, that is $H_{60}$-NO was a bit lower than $H_{45}$-NO, was possibly caused by the titration reaction of $O_3$ with NO. Similarly, HONO in the chamber between the two heights was expected to be homogeneously mixed when HONO was released from soil. The results obtained from laboratory research and field measurement confirmed that the OTCs system was able to reflect soil NO and HONO emissions.

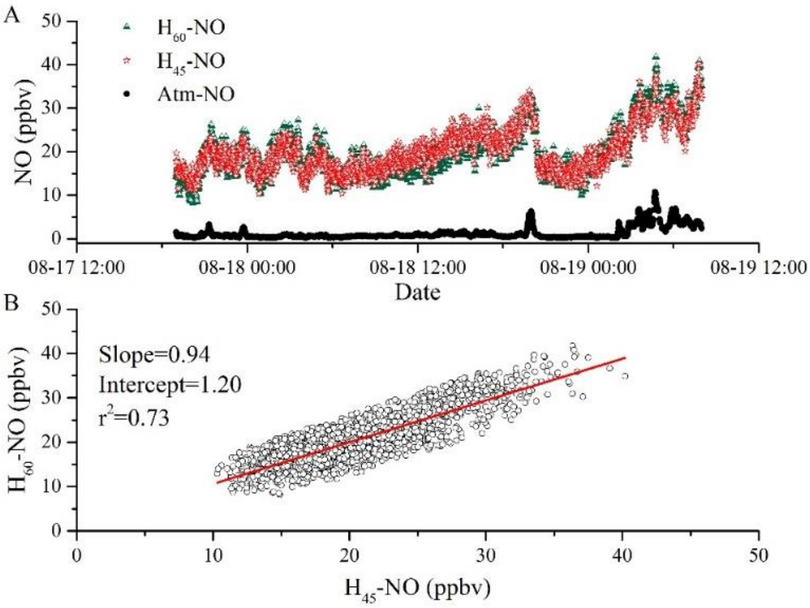

Figure 3.5 The gradient concentrations of NO in the Exp-chamber during the pre-experiment in August 2015. A. NO concentrations at the height of 45 cm ($H_{45}$-NO, red star) and 60 cm ($H_{60}$-NO, green triangle) inside the chamber and atmospheric NO concentration (black line). B. Correlation of NO concentrations at the height of 45 cm and 60 cm.

### 3.2.3 Greenhouse effect in the chamber

One of the critical parameters to assess the chamber methods, including the static chamber method and dynamic chamber method when measuring $CO_2$/$CH_4$/NO/$N_2O$/HONO/$NH_3$ emissions from the soil, is the greenhouse effect including the disturbance on temperature and relative humidity. For the measurement of HONO, a soluble gas with a large Henry constant of 49 M $atm^{-1}$ at 298K, the condensed water film on the inner wall of the chamber would absorb HONO, resulting in unauthentic emission fluxes.

For the static chamber method, which is always used in CO/$CH_4$/NO emission flux, the chamber was always covered by non-transparent material keeping out of sunlight[144]. However, the RH in the chamber was expected to increase quickly, and condensed water film was easy to form on the inner wall of the chamber. Moreover, photochemistry could be largely reduced, including photolysis and photosensitive reactions. Therefore, the traditional static chamber method did not suit to measure HONO emission flux. For the dynamic chamber method, including the open-top chamber method (OTC), the transparent cover (Teflon film) has almost no reduced impact on photochemistry in the chamber. Besides, fluxes inferred from the difference of the Exp-chamber and Ref-chamber eliminated the interference from wall effect and potential atmospheric interference.

Figure 3.6 shows the temperature and relative humidity inside and outside of the Exp-chamber in the pre-experiment in 2015. At nighttime, the temperature and RH inside and outside the chamber cooperated very well, while difference emerged in the daytime. The temperature inside the chamber was always higher than that outside the chamber, and RH inside the chamber was always lower than that outside the chamber (Figure 3.6 and Table 3.1). The averaged ΔT (T-inside - T-outside) was 1.9±1.1 °C leading to a small change in the chamber environment.

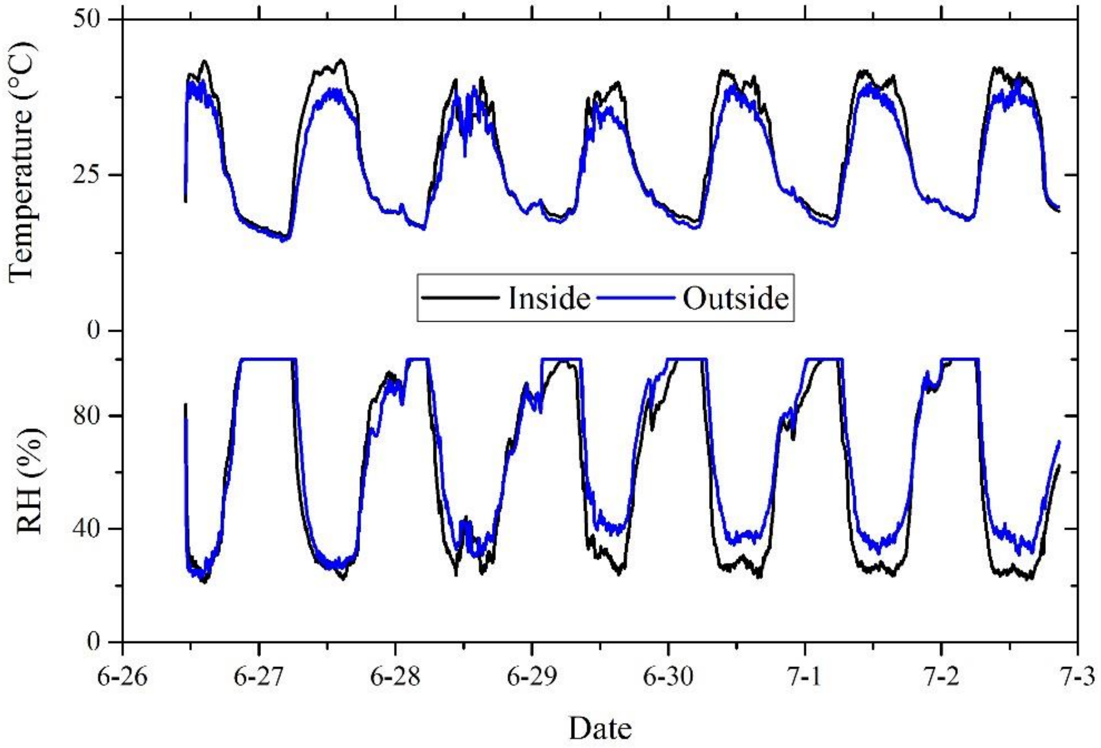

Figure 3.6 Temperature and relative humidity inside (black line) and outside (blue line) of the Exp-chamber in the per-experiment in 2015.

Table 3.1 Descriptive statistics of the temperature and RH inside and outside of the Exp-chamber (T-inside, T-outside, RH-inside, RH-outside, ΔT=T-inside - T-outside, ΔRH=RH-inside - RH-outside) in the pre-experiment. The number for Observation represents the amount of the observed data.

| | T-inside (°C) | T-outside (°C) | ΔT (°C) | RH-inside (%) | RH-outside (%) | ΔRH (%) |
|---|---|---|---|---|---|---|
| Average | 28.3 | 26.5 | 1.9 | 61.3 | 66.8 | -4.8 |
| Median | 25.7 | 24.5 | 1.1 | 62.0 | 67.7 | -3.7 |
| Standard Divation | 9.2 | 8.0 | 1.9 | 30.4 | 27.5 | 6.9 |
| Minimum | 15.2 | 14.4 | -1.1 | 21.1 | 22.9 | -26.0 |
| Maximum | 43.4 | 40.2 | 7.3 | 100.0 | 100.0 | 13.7 |
| Observation | 1837 | 1837 | 1837 | 1837 | 1837 | 1837 |

The relative humidity inside the chamber was lower than that outside the chamber by 3.7% (Table 3.1). The ΔRH (RH-inside - RH-outside) may mainly come from the change of temperature. For example, when the temperature varied from 26.5°C to 28.3°C (Table 3.1), the saturated vapor pressure of water increased from 3.383 kPa to 3.783 kPa, resulting in 3.1% decrement of the relative humidity, assuming the water in the air was the same, which means the influence of the chamber on RH was only -1.7%. The decrement of RH in the chamber mainly resulted from the increase of the chamber temperature suggesting that air was pumped into the chamber with almost no water loss caused by the pump and the tubes during the flushing process. However, the small decrement of RH was just opposed to the formation of water film on the inner wall of the chamber, which largely avoids the interference from condensed water film.

### 3.2.4 Influence from chemical reactions in the chamber

The dynamic chamber method is strictly valid for inert trace gases. However, the destruction and the production of HONO (e.g., by HONO photolysis, HONO+OH, NO+OH, photolysis of $HNO_3$ or particulate $NO_3^-$, $NO_2$ heterogeneous reactions on the wall or soil surface) in the chambers may cause artificial fluxes that need to be corrected for.

As the loss or production rates by the reactions HONO+NO or NO+OH are typically at least one order of magnitude lower than the HONO photolysis even when assuming a high OH concentration of $5\times10^6$ molecule $cm^{-3}$. The photolysis rate of $HNO_3$, $J(HNO_3\rightarrow HONO)$, is not more than $2.4\times10^{-7}$ $s^{-1}$, four orders of magnitude lower than the HONO photolysis rate[147], indicating that the HONO formation path by $HNO_3$ photolysis is negligible. Then, to calculate the influence of gas-phase reactions on soil HONO emission fluxes, we only take HONO photolysis into account, which dominates the destruction of HONO during the daytime. HONO photolysis belongs to the first-order reactions:

$$c_t=c_0*e^{-J(HONO)\times t} \qquad (3.2)$$

Here, $c_t$ is HONO concentration after a period time, t, of photolysis and $c_0$ is the initial concentration of HONO. For the dynamic chambers, the loss of HONO depended on the photolysis rate and the transportation time from the soil surface to the sample height. Therefore, the loss of HONO flux by photolysis, β, is expressed as:

$$\beta=1-e^{-J(HONO)\times t} \qquad (3.3)$$

The ideal transportation time (t) is about 2.4 min. Assuming a typical maximum J(HONO) of $1\times10^{-3}$ $s^{-1}$, the loss of HONO by photolysis (β) will be about 13.4% (t=144s) and 21.3% (t=240s), respectively. It means the measured HONO fluxes are possibly underestimated largely, especially at noontime when the radiation is strong. To obtain the original emission ($c_0$), the underrated part of HONO flux from photolysis can be corrected by being divided by (1- β).

Note that the photolysis of particulate $NO_3^-$ happens in both the experimental chamber and reference chamber. The influence of photolysis of particulate $NO_3^-$ can be neglected because we calculate the soil HONO emission fluxes only based on the difference of HONO concentrations in experimental and reference chambers. Because the chamber is made of Teflon film, the heterogeneous reactions of $NO_2$ on the chamber walls (mainly Teflon film) are of little significance in the experimental chamber and reference chamber. However, the $NO_2$ heterogeneous reactions on the soil surface in the experimental chamber may have a positive impact on HONO fluxes, especially under sunlight. The concentration of $NO_2$ in the experimental chamber will be increased because of the soil NO emission, which can be oxidized to $NO_2$ by $O_3$. $NO_2$ and $O_3$ concentrations measured in this site were mostly lower than 20 ppbv and 100 ppbv, respectively (see section 4.1). Assuming maximum oxidization of NO by $O_3$ in the chamber, $NO_2$ concentrations in the chamber was 120 ppbv. In fact, $NO_2$ concentrations were expected to be much lower than 120 ppbv because of the short residence time in the chamber. Based on the findings of Stmmler et al. (2006)[38] and Han et al. (2016)[40], the largest HONO production on the soil surface is $5\times 10^{10}$ molecule $cm^{-2}$ $s^{-1}$ in the presence of 20 ppbv $NO_2$. As HONO production is not proportional to the initial $NO_2$ concentration[38], the production is predicted to be $1.0\times 10^{11}$ molecule $cm^{-2}$ $s^{-1}$ in the presence of 120 ppbv $NO_2$, which will lead to an increase of HONO concentration in the chamber by ca. 0.9 ppbv. However, NO-derived $NO_2$ is produced during the flushing process that air is blowing from the bottom to the top of the chamber. Since $NO_2$ in the chamber was expected to be much lower than 120 ppbv, the increase of HONO concentration in the experimental chamber by 0.9 ppbv is the theoretical maximum, and the practical influence from soil NO emission is expected to be much less than that. Besides, the HONO flux enhanced by soil NO emissions (soil-derived $NO\rightarrow NO_2\rightarrow HONO$) also belongs to soil-derived HONO emission.

### 3.2.5 HONO emissions before fertilization

On 10 August 2015, the OTCs system was assembled on bare agricultural soil where no fertilization or irrigation proceeded after wheat harvest. Figure 3.7 shows the HONO emission fluxes from the agricultural soil on the daytime of 11 August 2015 and 12 August 2015. HONO concentrations in the Ref-chamber (Ref-HONO) revealed a typical daytime variation trend that showed a peak in the morning and a minimum at noontime. However, HONO concentrations in the Exp-chamber (Exp-HONO) were significantly higher than Ref-HONO and showed a noontime peak (Figure 3.7A). Positive HONO emission fluxes from the agricultural soil were inferred from the difference between Exp-HONO and Ref-HONO. The HONO emission fluxes also showed noontime peaks and nighttime or morning minimums with an average of $1.89\pm0.87$ ng N $m^{-2}$ $s^{-1}$, which was comparable to the field measurement results reported by Laufs et al. (2017)[50] (up to 2.3 ng N $m^{-2}$ $s^{-1}$), Ren et al. (2011)[148] (up to 7 ng N $m^{-2}$ $s^{-1}$) and Zhou et al. (2011)[149] (2.7 ng N $m^{-2}$ $s^{-1}$). Assuming a mixing layer height of 100 m, the measured maximum HONO emission flux (3.21 ng N $m^{-2}$ $s^{-1}$) could account for about 200 pptv $h^{-1}$ of the missing HONO source.

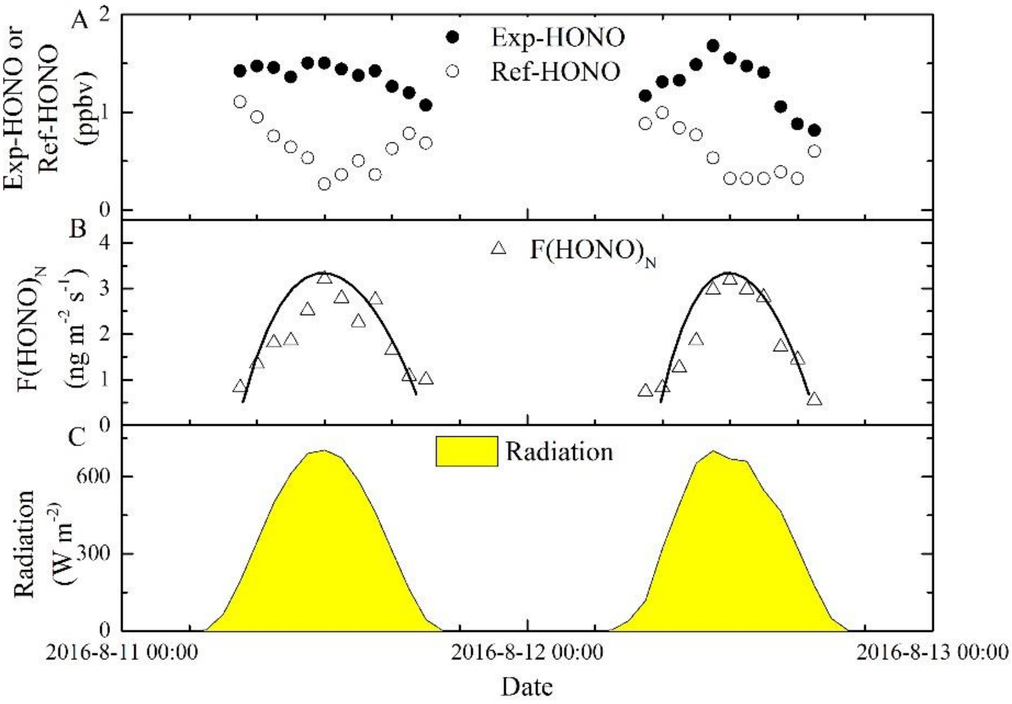

Figure 3.7 HONO emission flux from agricultural soil before fertilization from 2015-8-11 to 2015-8-12. A: HONO concentrations in the Exp-chamber (Exp-HONO) and the Ref-chamber (Ref-HONO). B: HONO emission fluxes. C: Solar radiation.

The variation trend of HONO emission fluxes in the daytime was similar to that of sunlight radiation (Figure 3.7B and C) with a good correlation ($r^2$=0.86, Figure 3.8A), which suggested that soil HONO emission may originate from photosensitive processes such as the reduction of $NO_2$ on the soil surface, the photolysis of nitrate on the soil surface, the displacement of HONO by strong atmospheric acids including HCl and $HNO_3$ generated in atmospheric photochemistry. In addition, a good correlation was found between the HONO flux profile and temperature ($r^2$=0.68, Figure 3.8B). As the temperature variation was consistent with soil temperature or at least with soil surface temperature, the HONO emission profile was suspected to be in good correlation with soil temperature. If so, soil HONO emission was possibly related to biological processes such as the nitrification process, which had been proposed to have the potential HONO emissions[68,150].

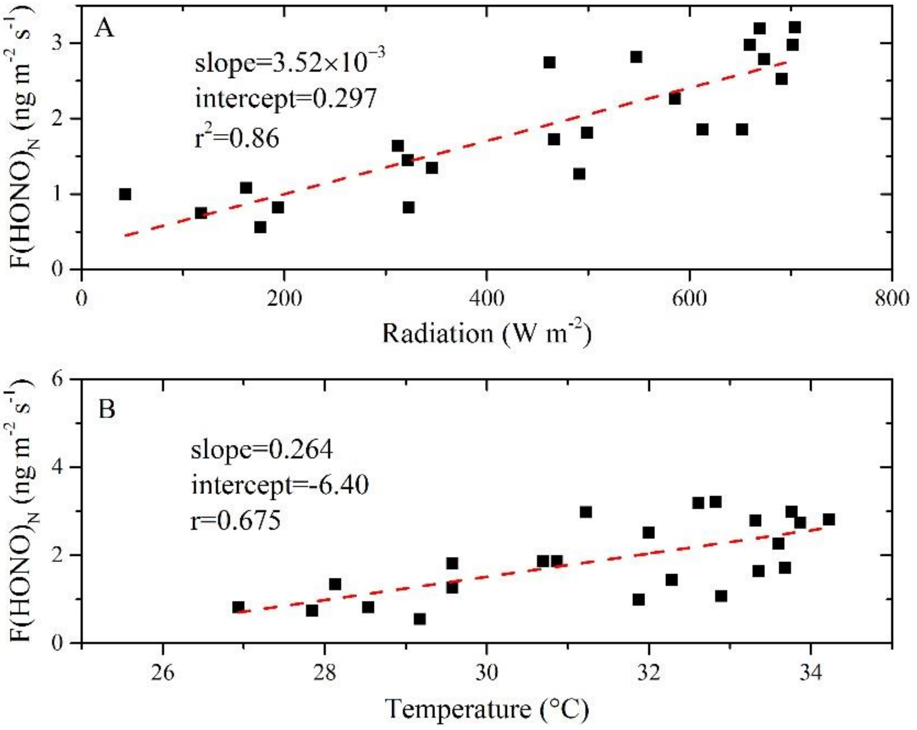

Figure 3.8 Correlations of HONO emission fluxes with radiation and temperature.

### 3.2.6 HONO emissions after fertilization

Figure 3.9 showed the HONO emission fluxes on 14 August 2015 after fertilization. Compared with the condition before fertilization, Exp-HONO after fertilization increased by one order of magnitude, while Ref-HONO was comparable to that before fertilization, leading to a massive increment of HONO emission fluxes (Table 3.2). The diurnal pattern of HONO fluxes after fertilization was similar to that before fertilization: a peak at noontime and a minimum in the morning. Fertilization accelerated soil HONO emission, while HONO formation from photosensitive processes discussed in chapter 3.5 was supposed to be similar to that before fertilization, suggesting that HONO emission from fertilized agricultural soil in the NCP was mainly from the biological process. As is reported by our previous studies[143–146], nitrification was largely enhanced by ammonium fertilization, resulting in a remarkable increment of $N_2O$ and NO emission. During the nitrification process, $NO_2^-$ is produced by ammonium oxidizing bacteria as an intermediate product, which is suspected to be an essential source for HONO. Therefore, soil HONO emissions are expected to be affected by the fertilization rate, which is probably like soil $N_2O$ and NO emissions[68,150].

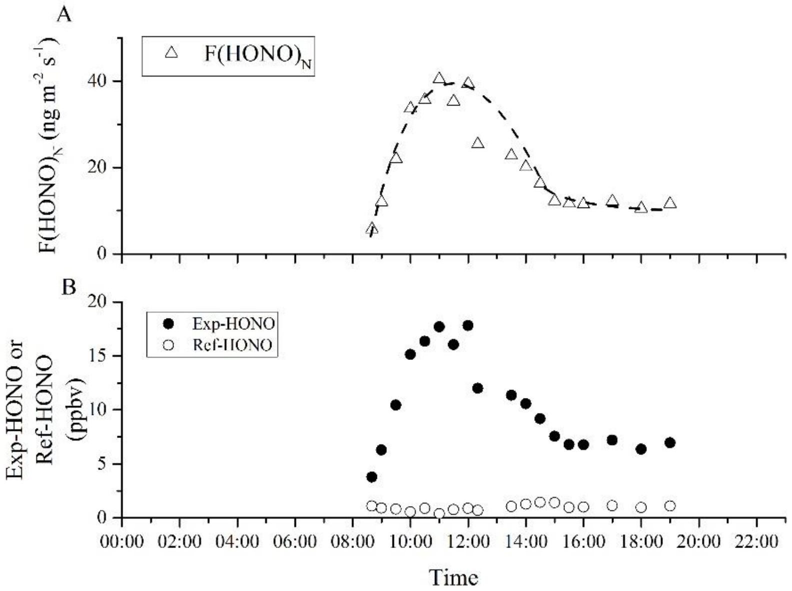

Figure 3.9 HONO emission flux from agricultural soil after fertilization and the variation of Exp-HONO and Ref-HONO on 2015-8-14. 50 mL compound fertilizer solution was evenly sprinkled on the soil surface inside the chamber on 2015-8-13.

Table 3.2 Descriptive statistics of HONO emission fluxes, Exp-HONO, and Ref-HONO before and after fertilization. The number for Observation represents the amount of the observed data.

| | Before fertilization | | | After fertilization | | |
|---|---|---|---|---|---|---|
| | F(HONO)$_N$ ng m$^{-2}$ s$^{-1}$ | Exp-HONO (ppbv) | Ref-HONO (ppbv) | F(HONO)$_N$ ng m$^{-2}$ s$^{-1}$ | Exp-HONO (ppbv) | Ref-HONO (ppbv) |
| Average | 1.89 | 1.33 | 0.60 | 21.00 | 10.46 | 0.97 |
| Midian | 1.81 | 1.41 | 0.60 | 18.19 | 9.81 | 0.97 |
| Standard Divation | 0.87 | 0.21 | 0.25 | 11.34 | 4.45 | 0.27 |
| Minimum | 0.55 | 0.82 | 0.27 | 5.69 | 3.78 | 0.40 |
| Maximum | 3.21 | 1.68 | 1.11 | 40.42 | 17.82 | 1.44 |
| Obeservation | 23 | 23 | 23 | 18 | 18 | 18 |

Note that the fertilization rate here was about 45 kg ha$^{-1}$ based on N, which was much lower than the local fertilization rate in the NCP. Local farmers used a fertilization rate up to about 330 kg ha$^{-1}$ based on N. Then, in the summer of 2016, we repeated the flux measurement over the agricultural soil in the NCP with a fertilization rate of 330 kg ha$^{-1}$ based on N. Figure 3.10 shows the result of the measurements in the summer of 2016. Unexpectedly strong HONO emission fluxes up to 1515 ng N m$^{-2}$ s$^{-1}$, was firstly found in the field measurement. The peak emission was two orders of magnitude higher than the reported fluxes, but comparable to the peak emission reported by laboratory simulations[69,150,151]. The averaged flux was 264 ng N m$^{-2}$ s$^{-1}$, which could account for about 3.3 ppbv h$^{-1}$ of the missing HONO source with an assumed mixing layer height of 500 m. Application with a higher fertilization rate indeed increased soil HONO emission, which was able to explain the missing source in the agricultural field. For example, Tan et al. (2017)[7] observed high HONO concentrations up to 2 ppbv at noontime also in an agricultural field of Wangdu. To maintain such high HONO levels at noontime, a source strength of about 7.2 ppbv $h^{-1}$ was needed with an assumed HONO photolysis frequency of $10^{-3}$ $s^{-1}$. The strength cannot be simply explained by reported homogeneous reactions or heterogeneous reactions without soil HONO emissions.

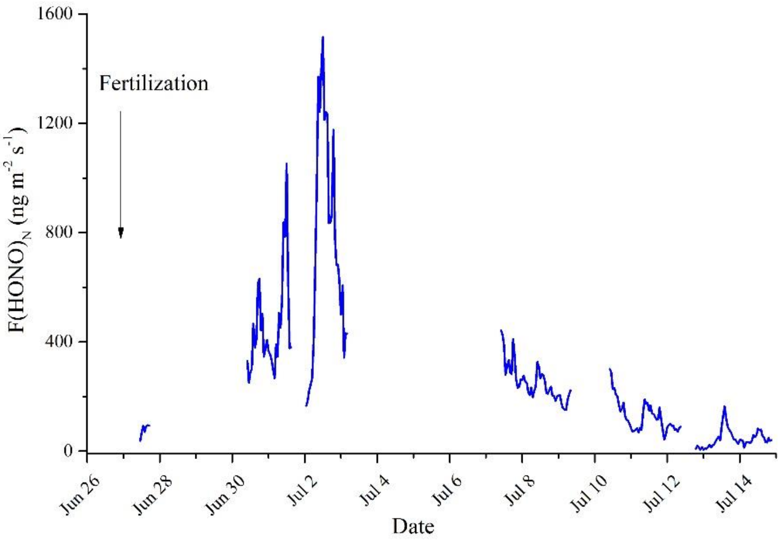

Figure 3.10 HONO emission fluxes in the summer of 2016. A large fertilization rate was applied in this measurement.

In addition, references also reported that N application rate by farmers in the NCP varied from 120 to 729 kg $ha^{-1}$ with a mean of 325 kg $ha^{-1}$ for winter wheat, and 96 to 482 kg $ha^{-1}$ with a mean value of 263 kg $ha^{-1}$ for summer maize[152,153]. As HONO emission from the biological process was strongly linked to soil nutrition, including $NH_4^+$, the agricultural soil in the NCP after normal fertilization with a large fertilization rate was more likely to be a huge reservoir for HONO. More research about HONO emission fluxes from agricultural soil in the NCP should be conducted to better understand the impact of HONO emissions on photochemistry and further the regional air pollution in the future.

## 3.3 Summary

The present study demonstrated a useful development and application of the twin open-top chambers (OTCs) method to measure HONO emission fluxes over agricultural soil in the NCP. Laboratory research and field measurement confirmed the excellent performance of the OTCs system to measure HONO emission fluxes from the soil. The interference from the wall effect, the greenhouse effect, and photolysis were rationally discussed. We found that the HONO emission flux (up to 3.21 ng N $m^{-2}$ $s^{-1}$) before fertilization could account for about 200 pptv $h^{-1}$ of the missing HONO source under an assumed mixing layer height of 100 m. The emission fluxes from agricultural soil in the NCP were largely enhanced by ammonium fertilization, which was possibly attributed to biological processes, including nitrification. Soil HONO emission was significantly affected by the fertilization rate. Our results in this study highlight the critical need to measure HONO emission fluxes from agricultural soil in the NCP and other similar regions to explore its impact on regional air quality.

# Chapter 4 Soil HONO emission flux measurement and regional $O_3$ pollution in the summertime

This chapter will detail results on 1) atmospheric HONO measurement in the summertime, 2) soil HONO emission flux measurement in the summertime, 3) laboratory simulations of soil HONO emissions, and 4) regional impact of soil HONO emissions on air quality.

Two papers about soil HONO emission flux measurement are in preparation. Details are as follows.

## 4.1 Field evidence for soil HONO emissions

In the summer 2017, atmospheric nitrous acid (HONO) and related pollutants like nitrogen dioxide ($NO_2$) were continuously measured at a rural site of the North China Plain (NCP). Remarkable increase of HONO and HONO/$NO_2$ was observed after fertilization of the agricultural fields, indicating strong HONO emission from agricultural soil. High HONO mixing ratios were expected to cause the enhancement of atmospheric oxidizing capacity, resulting in secondary pollution like ozone.

### 4.1.1 Atmospheric HONO and related parameters measurement

The measurement was conducted at the station of Rural Environmental, Chinese Academy of Sciences (SRE-CAS), located in Dongbaituo village (38°42′N, 115°15′E), Hebei province, China. The station was surrounded by agricultural fields with winter wheat and summer maize rotation. The campaign was carried out from 7 to 22 June 2017. Intensive fertilization followed by flood irrigation for summer maize was conducted during the campaign, and most of them around our station was conducted between 12 and 15 June. The nearest field around our station was fertilized on June 13. To better quantify the impact of fertilization, we classified the observations before 13 June as “before fertilization” and after June 13 as “after fertilization.”

Atmospheric HONO was continuously online measured by two Long Path Absorption Photometer (LOPAP)[154]. Both LOPAPs have been well operated in the previous studies[126,139]. The sampling units of the two LOPAPs were mounted at the height of about 3.4 m above the ground level. The two LOPAPs were regularly calibrated by “zero air” (>99.999% $N_2$) and diluted standard $NaNO_2$ solution (Sigma). NO and $NO_2$

were measured by a chemiluminescence technique analyzer (Thermo Fisher Model 42i, USA). The instrument can directly quantify NO by the reaction $NO + O_3 \rightarrow NO_2^* \rightarrow NO_2 + hv$. $NO_2$ was quantified indirectly by being converted to NO by a molybdenum converter with possible interference from other $NO_y$ species like HONO, $HNO_3$ and PAN. Therefore, $NO_2$ mixing ratios used in this study was corrected by subtracting HONO from the measured $NO_2$. Because of no available measurement of $HNO_3$ and PAN, the interference from $HNO_3$ and PAN was not considered in this study. $O_3$ was measured by a UV photometric analyzer (Thermo Scientific Model 49i, USA). Atmospheric $H_2O_2$ was measured by a wet liquid chemistry fluorescence detector (Aero-Laser AL2021, Germany). Besides, the meteorological parameters (air temperature, relative humidity, solar radiation, etc.) were measured by an auto meteorological station. Hourly averaged campaign data was used in this study.

### 4.1.2 Photolysis frequency values (J)

Photolysis frequency values (J) were unfortunately not available during this campaign. While in June, 2018， we had simultaneously measurements of solar radiation and J($NO_2$) in Tai'an city about 400 km south from our station, and they were highly correlated ($R^2$=0.96). Both our station and Tai'an city (36.17ºN, 117.11ºE) were located in the NCP, and both measurements were conducted in the same month (June) of the year. Therefore, similar correlations of solar radiation and J($NO_2$) were used here to obtain J($NO_2$) at our station. Then J(HONO) and J($O_3$) were calculated by the TUV model (https://www2.acom.ucar.edu/) and scaled by J($NO_2$).

### 4.1.3 Overview of the observations

Atmospheric HONO was measured by LOPAP-1 throughout the whole campaign (7-22 June) and by LOPAP-2 after fertilization (13 - 22 June). As shown in Figure 4.1A, HONO mixing ratios measured by the two LOPAPs exhibited the same variation, and they were highly correlated ($r^2$=0.93, Figure 4.2), indicating that both of the two LOPAPs were well operated during the campaign. In the following analysis, HONO mixing ratios measured by LOPAP-1 was used. Figure 4.1B to E showed the time series of hourly $NO_2$, $O_3$, $H_2O_2$, and solar radiation (Ra) during the campaign, respectively. The weather during the campaign was mostly sunny with clear sky conditions, based on the variation of solar radiation with similar daily noontime intensities of about 700 W $m^{-2}$ (Figure 4.1E). Throughout the campaign, the averaged mixing ratios of HONO, $NO_2$, $O_3$, and $H_2O_2$ were 1.3±0.7, 18±9, 52±30, and 0.6±0.6 ppbv, respectively. Besides, the mixing ratios of various pollutants, including HONO, $O_3$, and $H_2O_2$, except $NO_2$, clearly showed significant increases after fertilization compared to before fertilization (Figure 4.1).

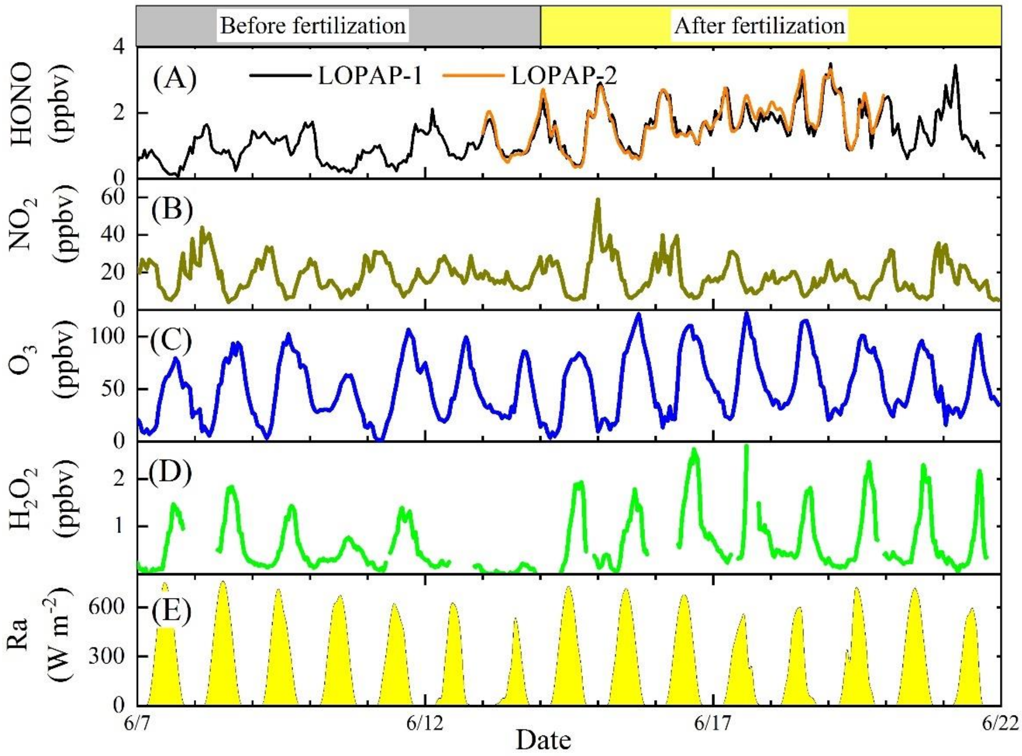

Figure 4.1 Time series of hourly HONO, $NO_2$, $O_3$, $H_2O_2$, and solar radiation (Ra) during the campaign.

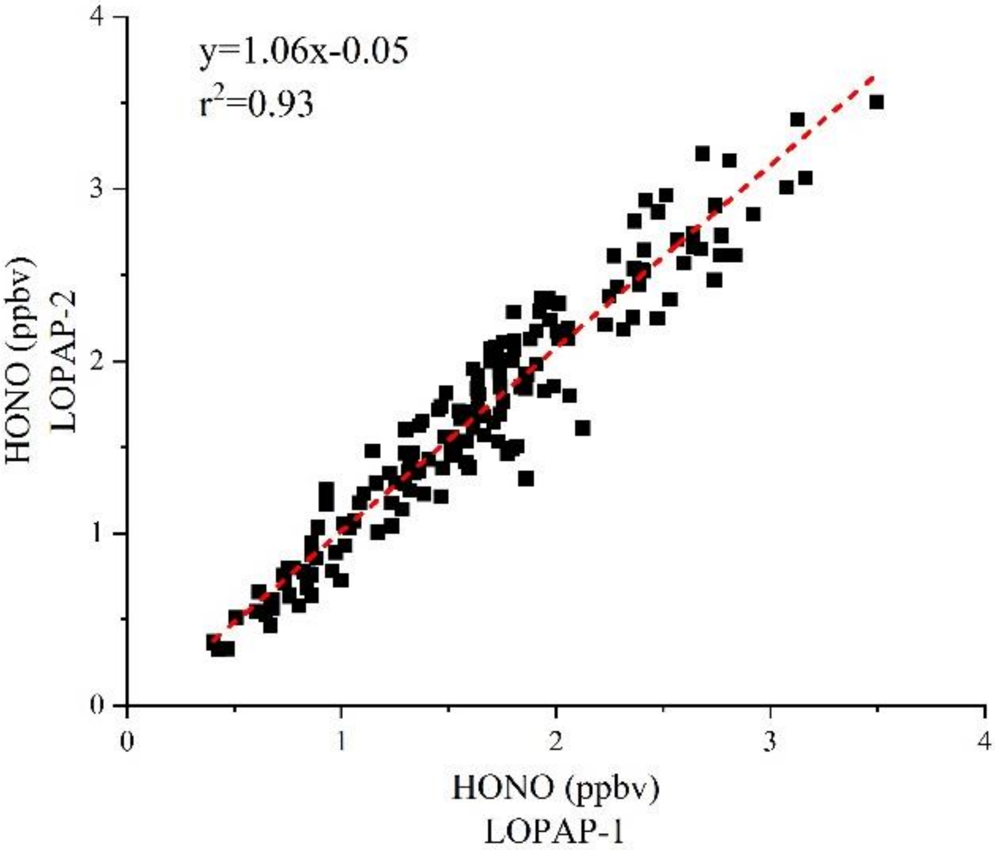

Figure 4.2 Correlation of HONO measurement from the two LOPAPs.

Figure 4.3A shows the diurnal variations of HONO during the periods before and after the intensive fertilization. The observed HONO before fertilization displayed a typical diurnal variation with a peak of about 1.3 ppbv after midnight and a minimum of about 0.5 ppbv in the later afternoon. However, HONO mixing ratios after fertilization became twice those before fertilization. In particular, the noontime HONO mixing ratio at 13:00 reached up to about 1.7 ppbv, which was unexpectedly three times higher than before fertilization (0.6 ppbv).

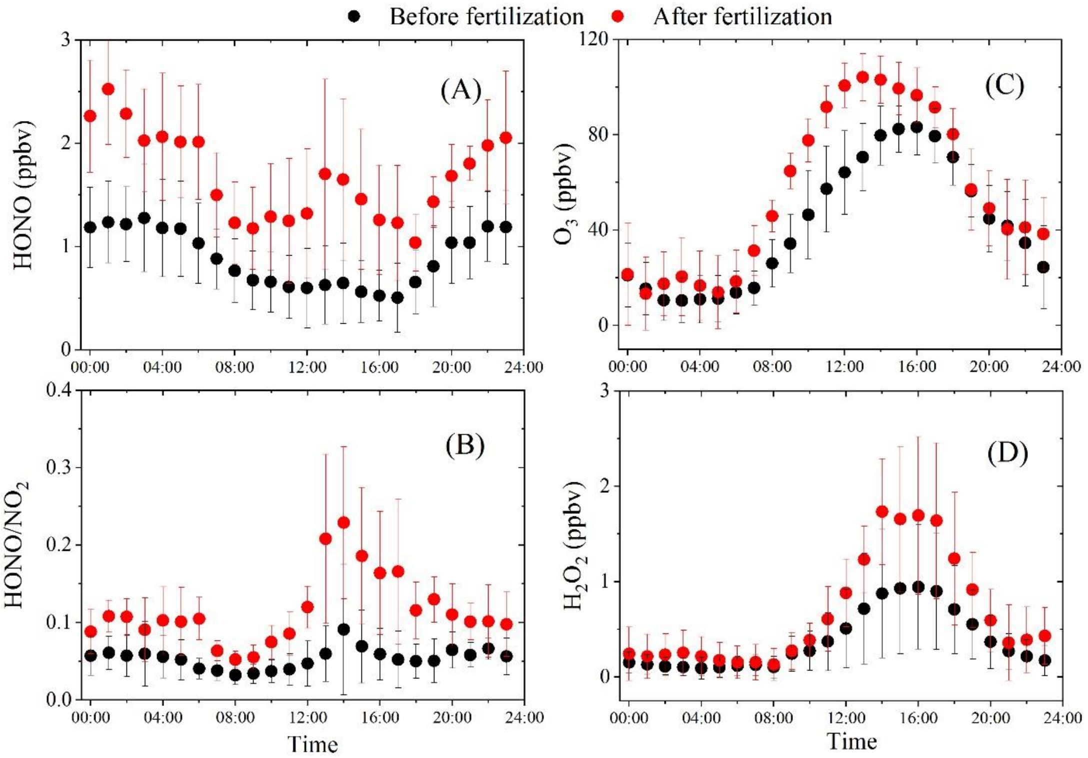

Figure 4.3 Diurnal variations of HONO, HONO/NO$_2$, O$_3$, and H$_2$O$_2$ during the periods before and after the intensive fertilization. The error bars represent the standard deviations (±1σ).

Figure 4.3B shows the diurnal variations of HONO/NO$_2$ during the periods before and after the intensive fertilization. Before fertilization, the average of HONO/NO$_2$ was (5.4±3.2)% (Table 4.1), which was comparable to other observations of about 1%-10%[20,23,26,45]. And the ratio started to increase after sunrise and reached the peak at noontime, which was majorly caused by the photosensitized heterogeneous reaction of NO$_2$ on surfaces[37,38,50]. After fertilization, although HONO/NO$_2$ exhibited the same diurnal variations, the values of HONO/NO$_2$ were unexpectedly higher with an average of HONO/NO$_2$ of (11.5±6.7)%, which was about the double of the observations before fertilization (Table 4.1). In particular, the maximum of daytime HONO/NO$_2$ reached 38%, which was much higher than the observations with NO$_2$-relevant reactions as the dominated source[20,23,26,45]. The NO$_2$ mixing ratios and diurnal variations (Figure 4.4) before and after fertilization were likewise comparable with averaged mixing ratios of 18.2 and 17.5 ppbv, respectively (Table 4.1), indicating that HONO formation from NO$_2$-relevant reactions was similar before and after fertilization. Therefore, the surprisingly high levels of HONO and HONO/NO$_2$ after fertilization suggested an additional strong HONO source not linked to atmospheric NO$_2$ but perhaps emitted by the fertilized soil.

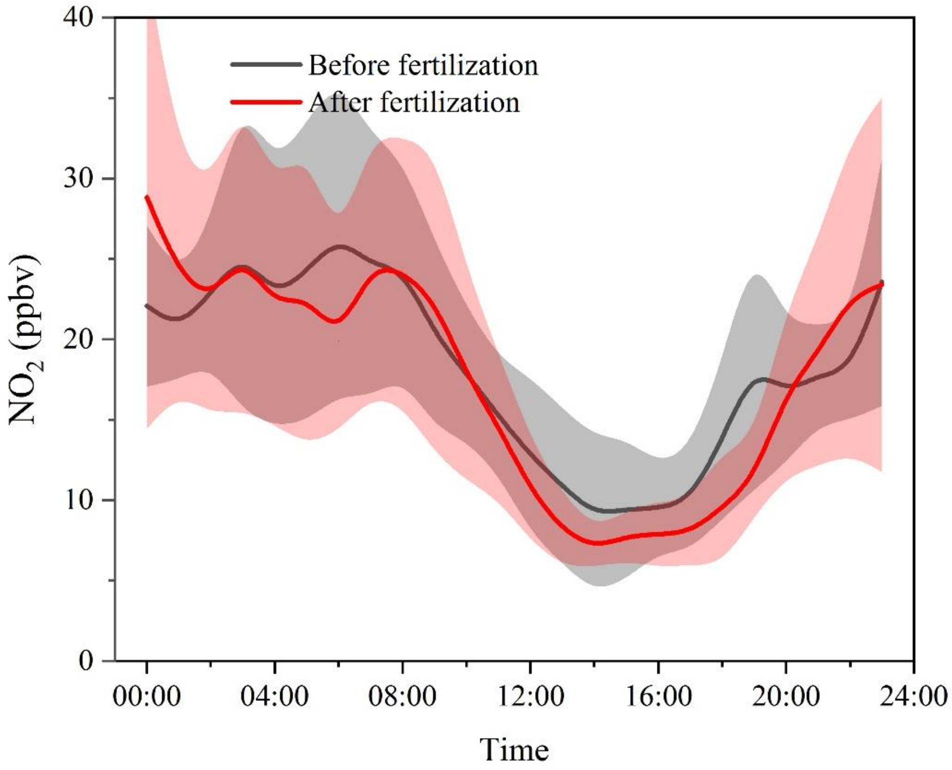

Figure 4.4 Diurnal variations of $NO_2$ mixing ratios before and after fertilization.

Figure 4.3C and D illustrate the diurnal patterns of $O_3$ and $H_2O_2$ during the periods before and after the intensive fertilization, respectively. Both $O_3$ and $H_2O_2$ exhibited a typical diurnal variation with a noontime peak and a nighttime minimum. And significant increases of $O_3$ and $H_2O_2$ were also observed after fertilization, which was similar to HONO observations after fertilization. During the daytime, averaged mixing ratios of $O_3$ and $H_2O_2$ increased from 53 to 70 ppbv and from 0.6 to 1.0 ppbv, respectively. Since daytime $H_2O_2$ was mainly formed by the self-reaction of $HO_2$, high $H_2O_2$ mixing ratios imply high levels of radicals as well as rapid radical production. Likewise, the occurrence time of peaks of $O_3$ and $H_2O_2$ after fertilization (13:00 and 14:00) exhibited 2-3 hours earlier than the observations before fertilization (16:00 and 16:00), which is 2-3 hours closer to HONO peaks (13:00), indicating the significant impact of the enhanced HONO after fertilization on the atmospheric oxidizing capacity, leading to severe secondary pollution, e.g., $O_3$ and $H_2O_2$.

Table 4.1 The statistical summary of HONO, $NO_2$, HONO/$NO_2$, $O_3$, $H_2O_2$, $P(OH)_{HONO}$, and $P(OH)_{O_3}$ before and after the intensive fertilization process. For each cell, the first and second numbers represent the data before and after the fertilization process, respectively. Ave, SD, Min, and Max represent the average, standard deviation, minimum, and maximum, respectively.

| Parameters | | HONO (ppbv) | $NO_2$ (ppbv) | HONO/$NO_2$ (%) | $O_3$ (ppbv) | $H_2O_2$ (ppbv) | $P(OH)_{HONO}$ (ppbv $h^{-1}$) | $P(OH)_{O_3}$ (ppbv $h^{-1}$) |
|---|---|---|---|---|---|---|---|---|
| All day | Ave | 0.9/1.7 | 18.2/17.5 | 5.4/11.5 | 47/57 | 0.4/0.7 | 1.2/2.6 | 0.4/0.5 |
| | SD | 0.4/0.7 | 7.9/9.4 | 3.2/6.7 | 27/31 | 0.4/0.6 | 1.7/3.3 | 0.6/0.8 |
| | Min | 0.05/0.4 | 4.1/5.4 | 0.4/3.1 | 1/4 | */* | 0/0 | 0/0 |
| | Max | 2.1/3.5 | 44/59 | 21.8/37.6 | 106/122 | 1.8/2.6 | 6.7/16.4 | 2.2/2.8 |
| Daytime<br>6:00-18:00 | Ave | 0.7/1.4 | 15.7/14.4 | 5.0/11.8 | 53/70 | 0.6/1.0 | 2.2/4.8 | 0.7/0.9 |
| | SD | 0.3/0.6 | 8.0/7.9 | 3.6/8.0 | 29/32 | 0.5/0.7 | 1.7/3.2 | 0.6/0.9 |
| | Min | 0.05/0.4 | 4.1/5.6 | 0.4/3.1 | 1/5 | */* | 0.1/0 | 0/0 |
| | Max | 1.5/3.1 | 40/39 | 22/38 | 106/122 | 2.2/2.8 | 6.7/16.3 | 2.2/2.8 |

*: $H_2O_2$ mixing ratios were lower than the detection limit of about 0.1 ppbv.

### 4.1.4 Discussion on soil HONO emissions and their impact

Our results propose evidence for strong HONO emissions from fertilized agricultural soil and potential impact on regional air pollution. The increase of the unknown HONO source strength ($P_{unknown}$) possibly represents the soil HONO emission strength. Exceptional growth of $P_{unknown}$ occurred at noontime, from 3.1 ppbv $h^{-1}$ to 8.4 ppbv $h^{-1}$ (Table 4.2). Assuming a mixing layer height of 100-1000 m, the increase of $P_{unknown}$ indicated a soil HONO emission flux of 84-840 ng N $m^{-2}$ $s^{-1}$, which is 2-3 orders of magnitude higher than observations in other places[50,53] but comparable to the strong emissions in laboratory studies[66]. Additionally, the soil HONO emissions might be more significant than expected because few fields had already been fertilized before intensive fertilization.

Table 4.2 HONO unknown sources before and after the intensive fertilization process. $HONO_{PSS}$ means the HONO concentration calculated by the photo-stationary steady-state (PSS). Note that the averaged variation of OH concentrations from a campaign conducted at the same place in June 2014 was used here.

| Date | Time | HONO (ppbv) | $HONO_{PSS}$ (ppbv) | $P_{unknown}$ (ppbv $h^{-1}$) | Average (ppbv $h^{-1}$) |
|---|---|---|---|---|---|
| **6.7-6.13** | **11:00** | 0.61 | 0.12 | 3.03 | 3.1 ± 0.1 |
| | **12:00** | 0.60 | 0.11 | 3.09 | |
| | **13:00** | 0.63 | 0.11 | 3.16 | |
| | **14:00** | 0.65 | 0.09 | 3.17 | |
| **6.14-6.20** | **11:00** | 1.25 | 0.09 | 7.20 | 8.4 ± 1.3 |
| | **12:00** | 1.32 | 0.14 | 7.40 | |
| | **13:00** | 1.70 | 0.07 | 9.96 | |
| | **14:00** | 1.65 | 0.06 | 9.04 | |

Nevertheless, our results proposed an important implication. High daytime mixing ratios of HONO due to potential soil HONO emissions could cause enhancements of atmospheric oxidants like $HO_x$ ($OH+HO_2$) through the photolysis of HONO (P(OH)). As shown in Figure 4.5, $P(OH)_{HONO}$ after fertilization with an average of 4.8 ppbv $h^{-1}$, ascended by a factor of >2 compared to before fertilization (2.2 ppbv $h^{-1}$), while both OH production from $O_3$ photolysis ($P(OH)_{O_3}$) before and after fertilization were less than 1 ppbv $h^{-1}$. The remarkable rise of OH production due to high HONO levels was expected to aggravate regional air quality, e.g., the increase of $O_3$ and $H_2O_2$ observed in this study.

Here we addressed the potentially significant HONO emissions from agricultural soil, which is in agreement with previous laboratory studies[66,68,69,155]. The new phenomenon observed here still needs to be explained, e.g., the potential high HONO emissions just after fertilization and flood irrigation when the soil water content was almost saturated. More research is required to explore the mechanism of soil HONO emissions in this region. We also suggest that soil HONO emissions in this or similar regions need to be considered in the model to quantify the impact on the regional air quality.

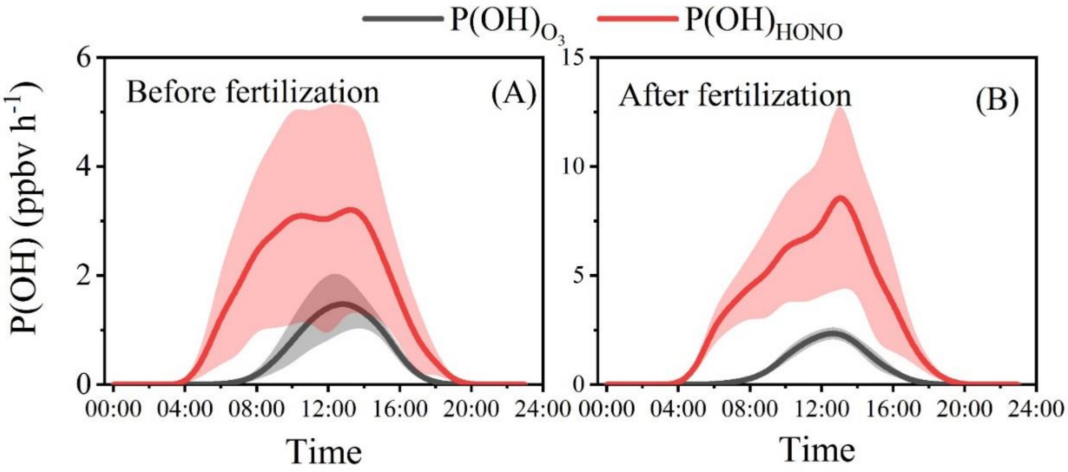

Figure 4.5 The diurnal variations and time series of the OH production rates from photolysis of HONO and $O_3$. The shadowed areas represent the standard deviations (±1σ).

## 4.2 Soil HONO emission flux measurement

In summer 2016, a campaign with measurements of soil HONO emission flux, HONO mixing ratio and related pollutants (NO, $NO_2$, $NO_y$, etc.), meteorological parameters (temperature, relative humidity, solar radiation, etc.), and soil parameters (water content, soil pH, soil temperature, soil ammonium, nitrate, and nitrite, etc.) was conducted at the SRE-CAS station.

### 4.2.1 Experimental

The field experiments were carried out at the Station of Rural Environment, Chinese Academy of Science (SRE-CAS), which is located in an agricultural field (38°71′N, 115°15′E) in Wangdu County, Hebei Province of China. Winter wheat and summer maize have been cultivated for several decades in the field. The soil pH (in a 1:2.5 soil to water), organic C and total N were 8.1, 8.34-9.43 g kg$^{-1}$ and 1.02-1.09 g kg$^{-1}$, respectively.

According to the cultivation habit of the local farmers for summer maize, compound fertilizer (1125 kg ha$^{-1}$, N($NH_4Cl$): $P_2O_5$: $K_2O$=22%: 8%: 15%) was evenly distributed into the agricultural field after planting the summer maize on 19 August 2016, and the field was immediately flood irrigated. The HONO concentrations in the experimental and reference chambers were continually measured from 18 August to 6 September 2016. The bottom of the experimental chamber covered one maize in the center, and the maize emerged from the soil approximately one week after planting.

For comparison with the values of soil water content (SWC) reported by the previous studies[69,150,155,156], the SWC in this study was calculated based on the water-holding capacities (WHC), which is derived from the equation:

$$WHC = \frac{m_{sat-water}}{m_{dry-soil}} \qquad (4.1)$$

where $m_{sat-water}$ is the weight of soil water under the condition of the soil saturated with water, and $m_{dry-soil}$ is the mass of the soil after heating at 105 °C for 24 hours. The SWC in % WHC is the proportion of the weight of soil water to $m_{sat-water}$.

During the period of the HONO flux measurements, the concentrations of atmospheric $NO_x$ (NO, $NO_2$) and $NO_y$ (the sum of the reactive nitrogen oxides, including NO, $NO_2$, $HNO_3$, and HONO, etc.) were measured by Model 42i-$NO_x$ analyzer (Thermo Scientific, USA) and Model 42i-$NO_y$ analyzer (Thermo Scientific, USA), respectively. The soil temperature and the air relative humidity (RH) were automatically measured and recorded by a meteorological station in the SRE-CAS station.

Soil HONO emission flux measured in the summer campaign of 2016 was assumed to represent the regional HONO emission from the agricultural soil because of the same land and same fertilizers. However, the fertilization on the soil was conducted in August, significantly later than local farmers' activities; therefore, the observed atmospheric pollutants were no expected to be affected by the regional HONO emissions. Then in the summer of 2017, a field campaign with measurements of various atmospheric pollutants was conducted exactly one week before and after the local intensive fertilization. Atmospheric HONO, $O_3$, $H_2O_2$, and $PM_{2.5}$ were measured by LOPAP, a Model 49i-$O_3$ analyzer (Thermo Scientific, USA), an $H_2O_2$ monitor (AERO laser model AL 2021, Germany) and a TEOM 1405 (Thermo Scientific, USA), respectively. The sampling height for the instruments was approximately 3.5 meters above the ground.

During the campaign, soil samples were collected every two days to measure the concentrations of soil water content (% WHC), soil nitrite, and soil pH. After sieving by a 2 mm sieve, the soil samples were divided into three parts: one for measuring the SWC by quantifying the soil weight before and after heating in an oven at 105 °C for 24 hours, one for measuring the soil pH based on the method of ISO 10390:2005-2012 and the other for measuring the soil nitrite concentration based on the method of ISO/TS 14256-1:2003 (E).

### 4.2.2 Overview of the measurements

As shown in Figure 4.6, the HONO concentrations in the experimental chamber (with its bottom covering the agricultural field) during the period of the flux measurements were evidently higher than those in the reference chamber (with its bottom covered by Teflon film). The HONO emission fluxes derived from the difference in the HONO concentrations between the twin chambers exhibited distinct diurnal variations with peak emission at noontime (approximately 13:00). The HONO emission peaks of about 350 ng N $m^{-2}$ $s^{-1}$ from the agricultural field were generally 1-2 orders of magnitude higher than those (<7 ng N $m^{-2}$ $s^{-1}$) from agricultural fields investigated in the only two previous studies[50,148]. Additionally, the noontime HONO emission peaks measured in this study were also inconsistent with the early morning emission peaks observed by the previous studies. The different fertilization rates during the flux measurements might be one of the reasons for the large difference in the HONO emission strengths between the two previous studies and our study, e.g., the fertilization rate of 100 kg N $ha^{-1}$ ($NH_4NO_3$ plus urea) for the field in Orleans[50], no mention of the fertilization rate for the field in California[148], and a large fertilization rate of 247 kg N $ha^{-1}$ (compound fertilizer with the nutrient N as $NH_4Cl$) in this study. In addition, the different flux measurement techniques used might also be partially responsible for the large difference. The two previous HONO flux measurements from the agricultural fields were conducted by using indirect methods such as the relaxed eddy accumulation method and the aerodynamic gradient method. The relatively slow response of the HONO measurements and the photolysis of HONO might influence the accuracy of HONO flux measurements by using the indirect methods, e.g., the aerodynamic gradient method for flux measurements has been recognized as less accurate due to the large scatter of the concentration measurements and the influence of chemical transformation during the turbulent transport process[157,158].

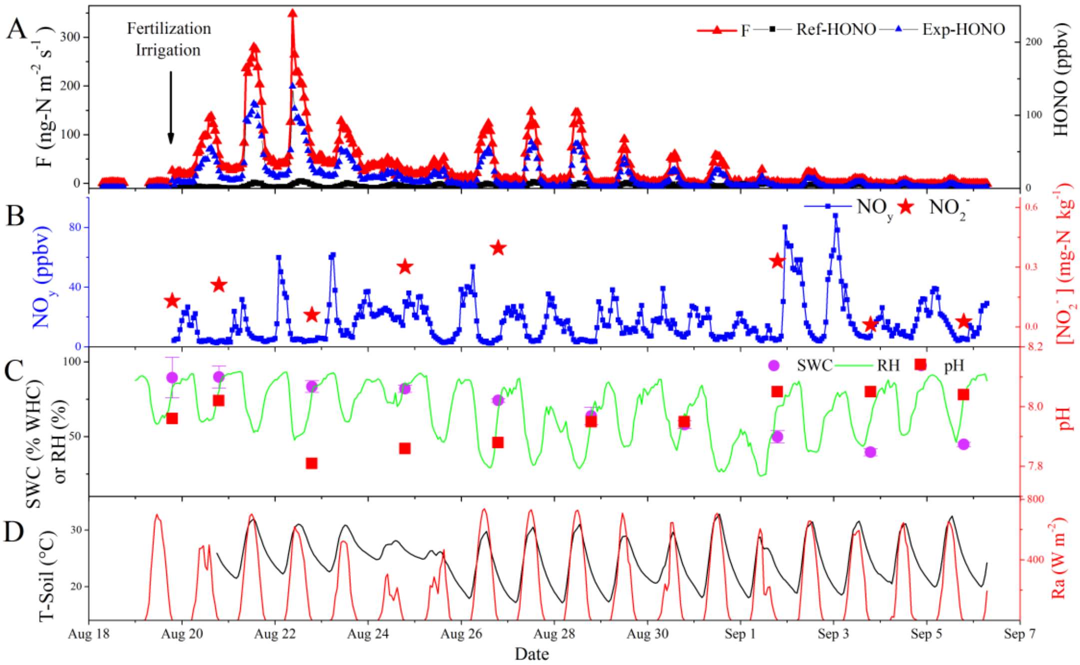

Figure 4.6 Time series of HONO emission fluxes and related parameters. (A) HONO emission fluxes (F) and HONO concentrations in the experimental chamber (Exp-HONO) or the reference chamber (Ref-HONO). (B) Concentrations of the ambient $NO_y$ ($NO_y$) and soil nitrite ($NO_2^-$). (C) Soil water content (SWC), relative humidity (RH) of the ambient air and soil pH (pH). (D) The soil temperature (T-soil) and the total radiation of sunlight (Ra).

### 4.2.3 Possible mechanisms

The two previous investigations found a significant correlation between the HONO emission fluxes and the products of $NO_2$ concentration with the sunlight intensity. They concluded that the light-induced reduction of atmospheric $NO_2$ on agricultural soils might be responsible for HONO emissions from the fields. However, even if the $NO_y$ compounds (the sum of reactive nitrogen compounds, including NO, $NO_2$, $HNO_3$, and PAN) observed in ambient air were assumed to be $NO_2$ and completely converted to HONO, their concentrations (Figure 4.6B) at noontime could not account for the high HONO levels measured in the experimental chamber (Figure 4.6A). Similarly, the mechanism proposed based on the field measurements regarding the exchange of HONO adsorbed in the soil surface by the deposition of strong acids (such as $HNO_3$) during the daytime could also be excluded.

Based on the prediction from the chemical acid-base equilibrium calculations[155], the maximal HONO flux from the agricultural soil (pH≈8, $[NO_2^-] < 0.5$ mg N $kg^{-1}$ soil, Figure 4.6B and C) would be less than 1 ng N $m^{-2}$ $s^{-1}$, which is a factor of about 350 less than the maximal HONO emission flux measured by this study. The large gap in the HONO emission fluxes between the predicted and field measurements might be because the prediction did not consider the acidification effect of the soil microenvironment due to ammonium nitrification[71]. Although ammonia-oxidizing bacteria has been found to directly release HONO from soils and the emission flux was larger than that expected from the chemical acid-base equilibrium[68,69,71,150], the narrow range of soil water content (SWC, 10-30% of the water holding capacity (WHC)) for HONO emissions found by the laboratory simulation experiments could not account for the noontime emission peaks of HONO from the present agricultural field with SWC values much greater than 30% WHC (Figure 4.6A and C). The relation between the HONO fluxes and the SWC derived from the laboratory experiments might be because the ammonium nitrification rate remarkably varies with increasing incubation time in soil. Additionally, the relatively high nitrification rate might coincidently occur at an SWC of 10-30% WHC under their experimental conditions of slowly drying the humidified soil samples in the chamber[68,69,71,150]. The maximal HONO emission peak from the field with an SWC of ~80% WHC (Figure 4.6A and C) indicated that HONO emission from the soil could occur in a wide range of soil water contents rather than the narrow range (10%-30% WHC) reported by the previous studies[68,69,71,150]. A new mechanism for soil HONO emission in the NCP needs to be proposed.

## 4.3 Laboratory experiments on soil HONO emission mechanism

### 4.3.1 Soil samples

During the campaign, about 50 kg of the surface soil at approximately 10 cm depth was collected by a scoop into a knitted bag and stored in a refrigerator at 4 °C after sieving with a 2 mm sieve before the laboratory simulations. The initial SWC of soil samples was measured by quantifying the soil weight before and after heating in the oven at 105 °C for 24 hours. Part of the soil was sterilized by an autoclave at a given pressure (0.1 MPa) and temperature (121 °C) for 1 hour. In addition, 75 g of the soil sample was filled into a half Plexiglas tube with a surface area of 0.08 $m^2$, humidified to 90% WHC by the water solutions of various fertilizers, and then incubated at room temperature (25±2 °C) for a period. The water loss during the incubation period was compensated by adding deionization before each experiment of the flow tube simulations, in order to keep the soil water content stable. The fertilization rate of the soil was 400 mg N $kg^{-1}$ soil, which is equal to 250 kg N $ha^{-1}$ assuming the distribution of N fertilizer was evenly distributed within 5 cm in the field.

### 4.3.2 Flow tube

As shown in Figure 4.7, we have invested HONO emissions from agricultural soil by a double casing quartz tube (length: 50 cm, inner diameter: 3 cm, outer diameter: 6 cm). Inside the tube was placed the quartz tank (length: 40 cm, width: 2 cm, height: 1 cm) filled with soil samples. The double combined casing symbolized by the orange color in Figure 4.7 is for the thermostatic water bath to keep or change the temperature of the flow tube. Two thermostatic water bathes controlled by two three-way valves, were used here to keep the flow tube at different temperature levels, respectively. A dark cover was used here to keep the system away from ambient light in order to control the radiation in the flow tube. Three black lights (average wavelength: 365 nm) were installed on the top of the cover, with a distance to the soil surface of 6 cm. Note that when we used black lights, we did not use the water bath in order to avoid the influence of water on the radiation but performed those experiments at room temperature (25 ± 2 °C). A relative humidity controller (RHC), which consisted of a thermostatic water bath, a water washing bottle with ultrapure water inside two three-way valves, and two flow controllers, was used here to control the RH in the flushing gas. Briefly, the dry flushing gas ($N_2$:$O_2$=4:1) was divided into two embranchments, and each of them was controlled by the flow controller. One of the embranchments went through the water washing bottle to get wetted and then mixed with the other one before their entrance into the flow tube. The thermostatic water bath was to keep the temperature of the water washing bottle stable (±0.5 °C) so that the flushing gas could get a stable RH, and it could provide different RH by changing the ratio of the two embranchments. At the outlet of the flow tube, the HONO measurement instrument (LOPAP or SC-IC system) was connected by glass tubes with a length of less than 10 cm. Also, a $NO_x$ analyzer (Model 42i NO-$NO_2$-$NO_x$ analyzer, USA) was connected to measure NO.

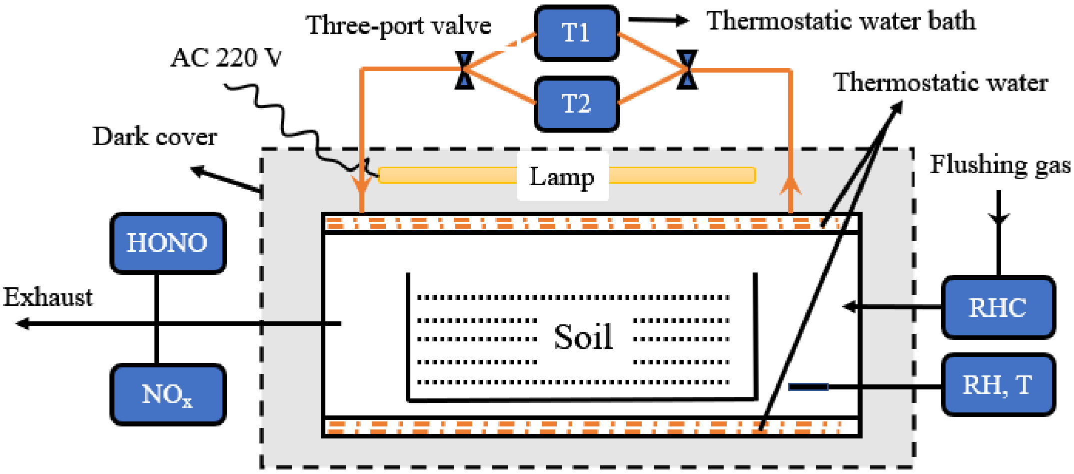

Figure 4.7 Diagram of the flow tube. RHC: relative humidity controller.

Before the laboratory simulation, we tested the sensitivity of the flow tube to the RH variation of flushing gas and the temperature variation of the thermostatic water bath. When changing RH in the flushing gas or changing the temperature of the water bath, the RH and temperature inside the flow tube reached the setting values in 2 min (±1 °C, ±3%). And the soil temperature reached the set temperature (±1 °C) of the thermostatic water bath in 3 min.

### 4.3.3 Treatments of the soil samples

#### *4.3.3.1 Temperature influence*

To investigate the influence of soil temperature on HONO emission (Figure 4.8A), the HONO emissions from the soil were measured during the process of soil temperature alternation between 18 °C and 35 °C with flushing air at an RH of 61.7% (25 °C). The soil temperatures of 18 °C and 35 °C were separately controlled by circulating water from two thermostat water baths. The synthetic air ($N_2$:$O_2$=4:1) directly passed through the water bubbler at room temperature (25±2 °C) to control the RH in the flushing air. The fertilized soil was incubated for 48 hours before the experiments.

RH influence

#### *4.3.3.2 Radiation influence*

To investigate the influence of radiation on HONO emission (Figure 4.8B), HONO emission from the soil were measured by alternating between dark and ultraviolet irradiation (310-370 nm) under flushing air at an RH of 58.5% (25 °C) and soil temperature of 35 °C. Two fluorescence lamps (30 W for each, Philips) with emissions of 310-370 nm ultraviolet light were mounted on the top of the flow tube. The fertilized soil sample was incubated for 48 hours before the experiments.

#### 4.3.3.3 RH of the flushing gas

To investigate the influence of RH on the HONO emission (Figure 4.8C), the variation in HONO emissions from the soil was measured by varying the RH from 48.8% (humidified air at 25 °C) to ~0% (dry air) in the flushing air at a soil temperature of 35 °C. The fertilized soil samples were incubated for 72 hours before the experiments, and triplicate experiments were conducted under each condition.

#### 4.3.3.4 Soil water evaporation influence

To investigate the influence of soil water loss from evaporation on HONO emission (Figure 4.8D), HONO emissions from one soil sample were continuously measured according to the sequence of RHs in the flushing air from high to low, and the amount of soil water loss ($\Delta m$) for each experiment was obtained by the difference of the soil weight before and after each HONO emission experiment during a period of 30 minutes at a soil temperature of 35 °C. The different RH in the flushing air was achieved through controlling the proportion of the dry air and humidified air or temperature of the bubbler. The fertilized soil sample was incubated for 88 h before the experiments.

#### 4.3.3.5 Fertilizer types

To investigate the influence of the soil with different treatments of fertilizers on the HONO emissions (Figure 4.9), the HONO and NO emissions were comparably investigated in the flow tube for the original soils sequentially treated by fertilization of $NH_4Cl$ (>99.5%, Sigma-Aldrich) and $KNO_3$ (>99%, Sigma-Aldrich) and by sterilization plus fertilization of $NH_4Cl$. The experiments were conducted by dry flushing air, and the soil temperature was maintained at 18 °C. The fertilized soil samples were incubated for ~12 hours before the first experiment. Additionally, the HONO emissions from the soil fertilized by three different concentrations of $NaNO_2$ were also investigated to reveal the influence of nitrite on the HONO emission. The experiments were conducted at soil temperatures of 18 °C and 35 °C, and the RH in the flushing air was controlled at 60% at 25 °C. The soil samples were incubated for 2 hours before the experiment.

#### 4.3.3.6 Nitrification inhibitors

To investigate the influence of nitrification inhibitors on HONO emissions, HONO and

NO emissions were comparably investigated in the flow tube for the original soils successively treated by fertilization of 100 mg-N ($NH_4Cl$) kg$^{-1}$ soil and 100 mg N ($NH_4Cl$) kg$^{-1}$ soil plus 10 mg DCD (Sigma Aldrich) kg$^{-1}$ soil. The soil temperature was controlled at 25 °C, and dry air was used in the experiment. The HONO and NO emissions were measured for 30 min every day.

### 4.3.4 Results of a new mechanism

As illustrated in Figure 4.6A, C, and D, the HONO emission positively correlated with soil temperature and sunlight intensity and negatively correlated with the air relative humidity (RH). To reveal which factors essentially affected HONO emissions from the field, the HONO emissions from the agricultural soil were further investigated by using a flow tube method under separated laboratory conditions. As shown in Figure 4.8A to C, an increase in the soil temperature or a decrease in the RH in the flushing air indeed resulted in a clear increase in the HONO emission, whereas ultraviolet irradiation (310-370 nm) had almost no effect on the HONO emission. Both the soil temperature and the RH of flushing air are the key factors affecting the water loss from the soil, and thus, the soil water loss was suspected of playing an important role in HONO emission from the soil. The exponential increase in the HONO emission with an increasing amount of soil water loss, as shown in Figure 4.8D, could support the above hypothesis. Because the amount of water loss during 30 min of the HONO emission measurements only accounted for <7.5% of the bulk soil water, the accumulation of liquid-phase HONO in the bulk soil due to the water loss could not explain the exponential increase in HONO emissions. HONO can be efficiently captured by neutral water as the method used for collecting gas-phase HONO in this study. Thus, the HONO formed in deep soil could be more easily intercepted by the soil water in alkaline soil. As shown in Fig in Figure 4.8C, the pulsed HONO emission after switching the humidified air to dry air indicated that HONO emission was mainly from the soil surface during the early stage of flushing and the deeper soil could only contribute to HONO emission as the surface soil became dry, resulting in the gradual increase in HONO emission during the later stage of flushing. For the field, the opposing variations in the soil temperature and RH (Figure 4.6C and D) favored a higher loss rate of surface soil water during the daytime and a lower loss rate during the nighttime, leading to a distinct diurnal variation in HONO emission from the agricultural field. Additionally, the relatively smaller daytime HONO emission peaks with approximately the same soil temperature but a relatively high RH during the cloudy days of 23-25 August (Figure 4.6A and C) (than in the neighboring clear days) also reveal the significant influence of soil water loss on HONO emission.

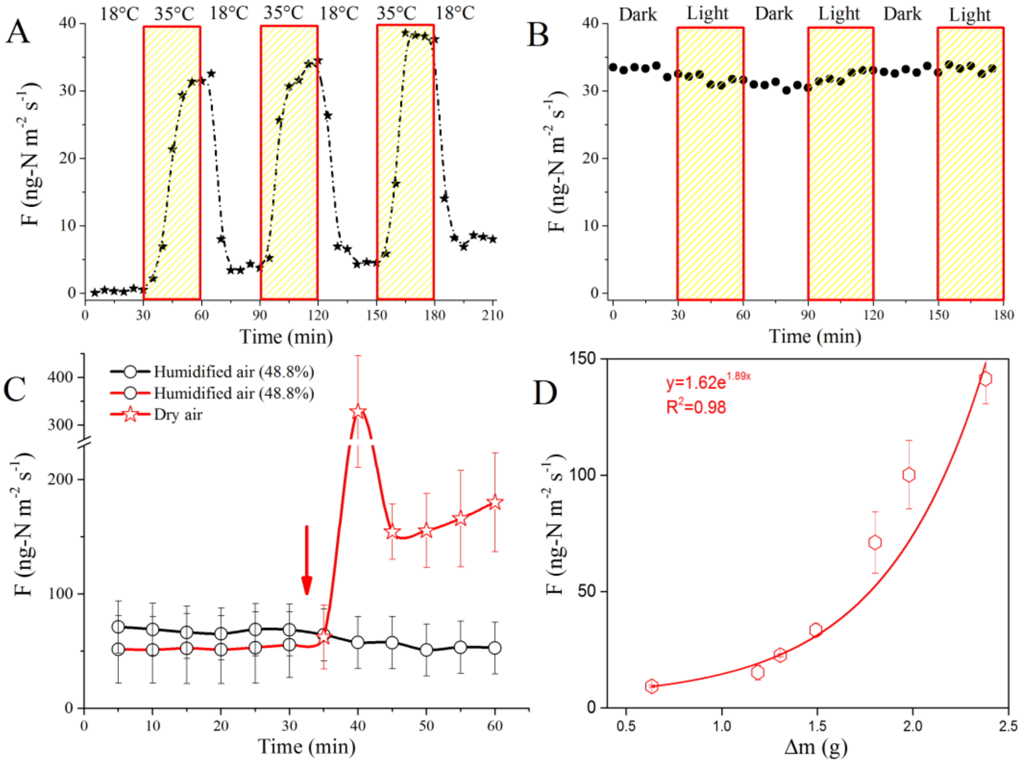

Figure 4.8 The influencing factors on HONO emission from the fertilized agricultural soil. (A) The variation in HONO emission from the soil during the process of the soil temperature alternating between 18 °C and 35 °C with flushing air at an RH of 61.7% (25 °C). (B) The variation in HONO emission from the soil alternating between dark and ultraviolet irradiation under flushing air at an RH of 58.5% (25 °C) and a soil temperature of 35 °C. (C) The variation in HONO emission from the soil with a varying RH in the flushing air at a soil temperature of 35 °C (the black cycles and the red stars represent the data measured under flushing with humidified air (RH=48.8% at 25 °C) and dry air, respectively. The red arrow is an indicator of the time for switching the humidified air to dry air, and the error bar is the standard division for triplicate experiments). (D) The correlation between the HONO emission and soil water loss (Δm) at a soil temperature of 35 °C. The error bar is the standard deviation for the five data points measured in each experiment.

The quick increase in the HONO emissions from the agricultural soil after the fertilization (Figure 4.6A) indicated that the available nitrogen from fertilization played a key role in the strong HONO emission from the soil. To further explore the origins of HONO emission after the fertilization, HONO and NO emissions from the agricultural soil with different treatments were investigated by using the flow tube method. As shown in Figure 4.9A, the emissions of HONO and NO from the original soil fertilized by $NH_4Cl$ exhibited similar trends, which were approximately a factor of 5-30 higher than those from the original soil sample fertilized by $KNO_3$ and the sterilization soil sample fertilized by $NH_4Cl$. Because the amount of N, the SWC, the RH in the flushing air and the soil temperature were all controlled in the same quantities for the three treatments, and the remarkably strong emissions of HONO and NO from the original soil fertilized by $NH_4Cl$ were rationally attributed to the nitrification of ammonium[68,150]. Although an SWC of 90% WHC was maintained in the experiments, the denitrification of nitrate was favored[159]. The relatively small HONO emission from the soil treated by nitrate implied that only the accumulation of $NO_2^-$ through denitrification without $H^+$ generation did not result in an increase in HONO emission. This was verified by the relatively small and stable HONO emission from the soil by only increasing the soil $NaNO_2$ concentration by a factor of five (Figure 4.10). Both $H^+$ and $NO_2^-$ can be produced through ammonium nitrification, and hence, the microenvironment around the nitrifier should be acidic and favors HONO emissions. Notably, the emissions of HONO and NO from the soil fertilized by $NH_4Cl$ increased approximately one order of magnitude from the first day to the fourth day (Figure 4.9), which was in line with the variation trend of HONO emissions from the field (Figure 4.6). The ammonium fertilization provided a substrate for propagating ammonia-oxidizing bacteria, resulting in an increase in HONO and NO emissions by increasing the ammonium nitrification rate during the incubation. The gradual decrease in HONO and NO emissions after the fourth day of fertilization indicated that the available ammonium in the soil might become the limiting factor for nitrification because a significant fraction of the ammonium applied might be consumed by the nitrifier.

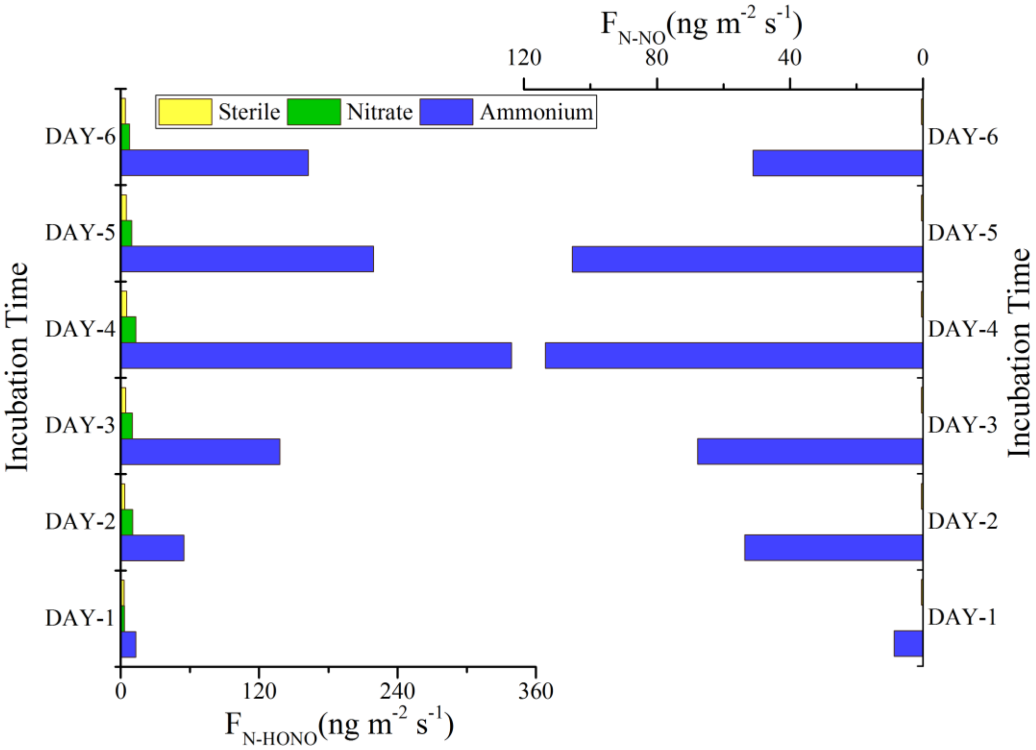

Figure 4.9 The emissions of HONO and NO from the agricultural soil with different treatments. The variations in HONO emissions ($F_{HONO\text{-}N}$, the left part) and NO emissions ($F_{NO\text{-}N}$, the right part) from the soil treated by sterilization plus $NH_4Cl$ (Sterile), by $KNO_3$ (Nitrate) and by $NH_4Cl$ (Ammonium) during the period of incubation. The soil temperature was 18 °C, and dry synthetic air was used for flushing.

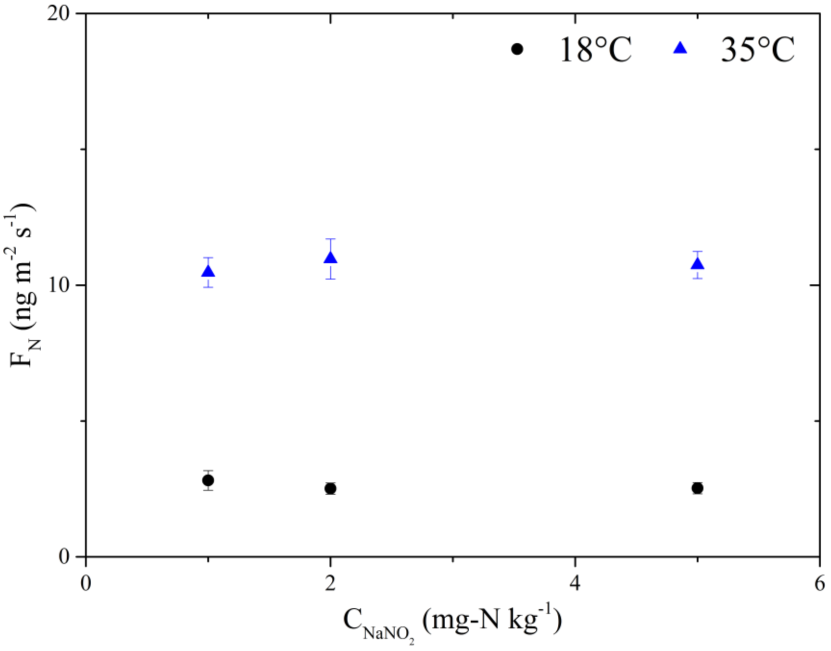

Figure 4.10 HONO emissions from the soil sample treated by $KNO_3$ (Nitrate) with increasing the soil $NO_2^-$ concentration by a factor of five under temperatures of 18 °C and 35 °C, respectively, and the RH was controlled at 60% at a temperature of 25 °C.

In all, as shown in Figure 4.11, soil HONO emissions from the agricultural soil in the NCP originated from the nitrification process where $NH_4^+$ was converted to $NO_3^-$ with the intermediate production of $NO_2^-$ and $H^+$. During a proper soil temperature range (18-35 °C), soil HONO emissions increase with soil temperature. The soil water evaporation accelerates the combination of $NO_2^-$ and $H^+$ leading to rapid HONO release from the soil during the daytime.

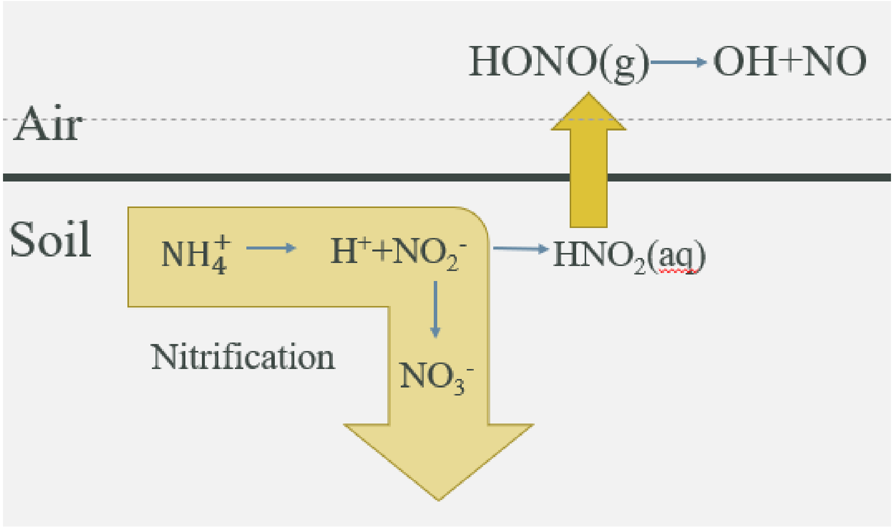

Figure 4.11 The schematic diagram of soil HONO emission mechanism.

## 4.4 Regional impact on $O_3$ pollution

### 4.4.1 CMAQ model configurations

CMAQ version 5.1 with the SAPRC07tic gas mechanism and AERO6i aerosol mechanism was applied in this study. The simulation domain covers China with a resolution of 36 × 36 km, based on a Lambert projection with two latitudes of 25°N and 40°N, as illustrated in Figure 4.12. The simulation period was 14 to 21 June 2017, with 4 days before as a spin-up time. The meteorological field was generated by the Weather Research & Forecasting Model (WRF) version 4.0, whose physical options and inputs are the same as Fu et al. (2019)[132]. The simulations well reproduced the observations of temperature, relative humidity, wind speed and wind direction at the Wangdu site (Figure 4.13). The Chinese anthropogenic emission data for 2015 were from Zhao et al. (2018)[160], which developed the emission inventory based on a bottom-up method with detailed Chinese local data. The 2017 anthropogenic emission data was generated by updating the 2015 data based on the ratio of 2017 emission to 2015 emission for China reported in Zheng et al. (2018)[161].

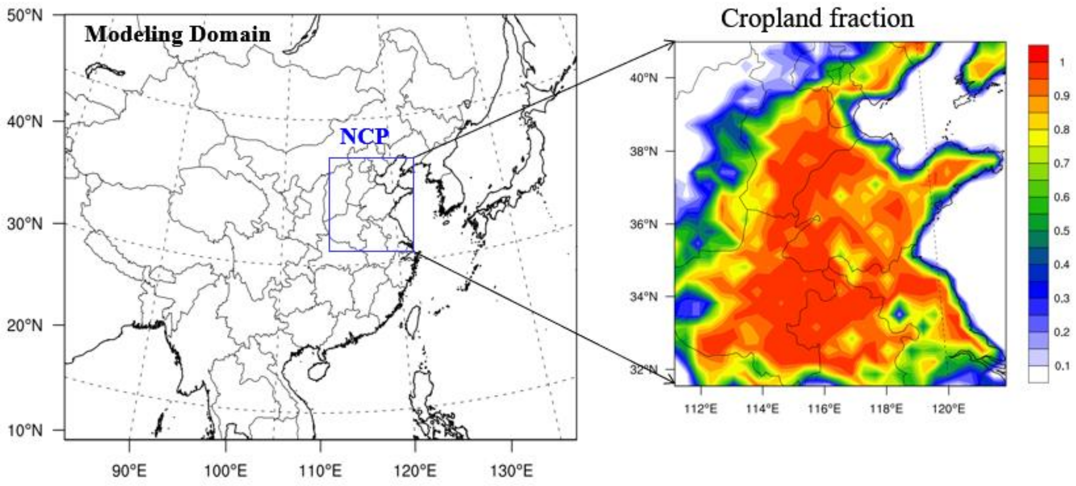

Figure 4.12 The modeling domain and cropland fraction for the model simulations.

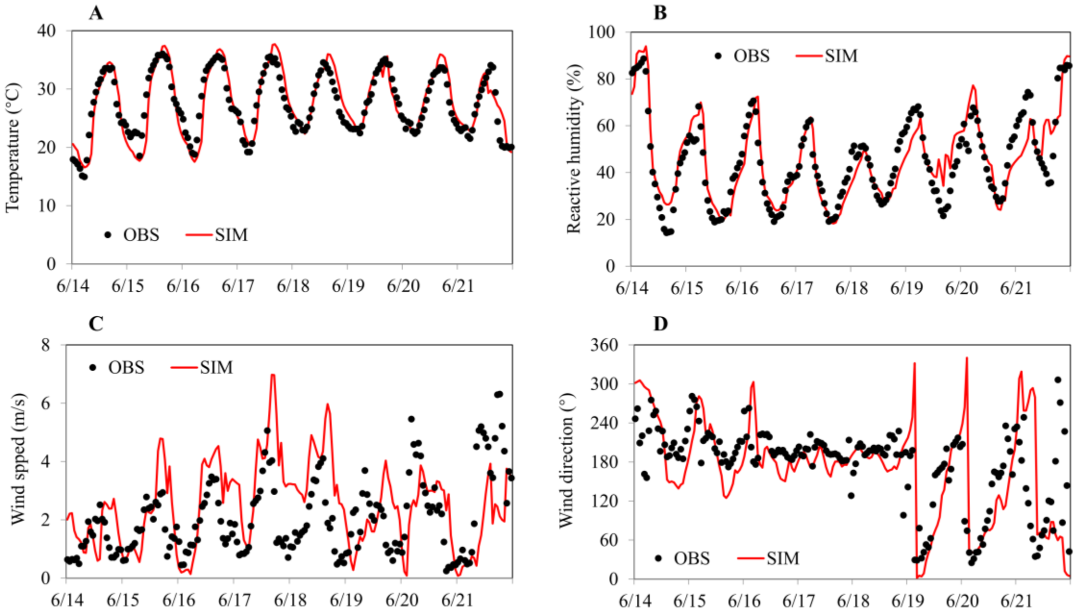

Figure 4.13 Comparison of the simulated and observed hourly temperature (A), reactive humidity (B), wind speed (C) and wind direction (D) during 14-21 June at the Wangdu site.

### 4.4.2 Simulation cases

In order to investigate the impacts of soil HONO emissions, two simulations were conducted: “without_soilHONO” and “with_soilHONO”. And to test the sensitivity, another case (2*with soil emissions) with double of the soil emissions was set. In the case "without_soilHONO", other major HONO sources have been considered, including HONO emissions from vehicles, the gas-phase reaction of NO and OH, the RH-dependent and light-enhancing heterogeneous reactions of $NO_2$ on the ground and particle surface and photolysis of particulate nitrate. In the case "with_soilHONO", besides the sources in "without_soilHONO", the soil HONO emissions during the daytime (7:00-17:00) were incorporated based on the parameterization derived in this study, as shown in an Arrhenius equation (4.2).

$$F_i = Ae^{-E_a/RT_i} \times f_i \qquad (4.2)$$

To show the impact of relative humidity, we define $A=x/RH_i$, then based on the measurement at Wangdu site, the results are:

$x=1.73e+27$

$E_a=147.4\ \mathrm{kJ\ mol^{-1}}$

Where $F_i$ is the soil HONO emission flux in the grid $i$; $RH_i$ and $T_i$ are the relative humidity and soil temperature in the grid $i$, which come from the output of WRF. Here, the simulated soil temperature is scaled down by 0.78 during the daytime based on the measured values at the Wangdu site. Fertilization is usually along with irrigation, which can lower the soil temperature, but the default model cannot represent this process. $f_i$ is the cropland fraction in the grid $i$. It's assumed that fertilizer is applied in the cropland, which can emit HONO with this high rate.

Figure 4.14 showed the calculated HONO emission flux and the observed HONO emission flux. It is clear that the same levels and variation trends were found between them, indicating that the equation obtained here can be used in the model.

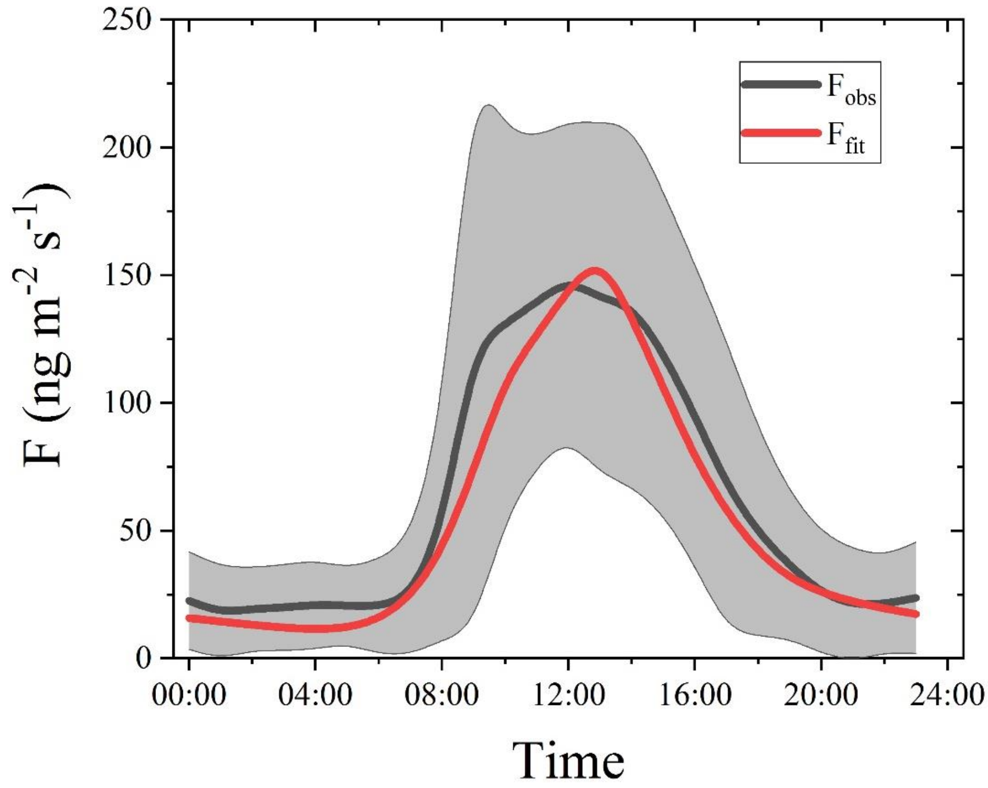

Figure 4.14 The diurnal variations of the observed and fitted HONO emission fluxes.

### 4.4.3 Impacts of soil HONO emissions on HONO and $O_3$ concentrations at the Wangdu site

As shown in Figure 4.15, the soil HONO emissions have significantly increased the daytime HONO concentrations at the Wangdu site, with the average daytime concentrations rising from 0.11 to 0.67 ppbv. The simulations with soil HONO emissions can generally reproduce the high daytime HONO concentrations on most days. The underestimation during 16-18 June may result from the overestimation of wind speed (Figure 4.13). With soil HONO emission as one of HONO sources, daytime HONO was significantly improved with the normalized mean bias (NMB) decreasing from -92% to -67% (Table 4.3). Even with the double of the HONO emissions (2*with soil emissions), HONO budget was still not closed, which might be because of the significant gradient distribution of HONO. The soil HONO emissions also led to a considerable increase of $O_3$ level, with the average maximum 1-h $O_3$ concentrations increasing from 109.9 to 123.1 ppbv, and the normalized mean bias (NMB) decreasing from -11% to -4% (Table 4.4).

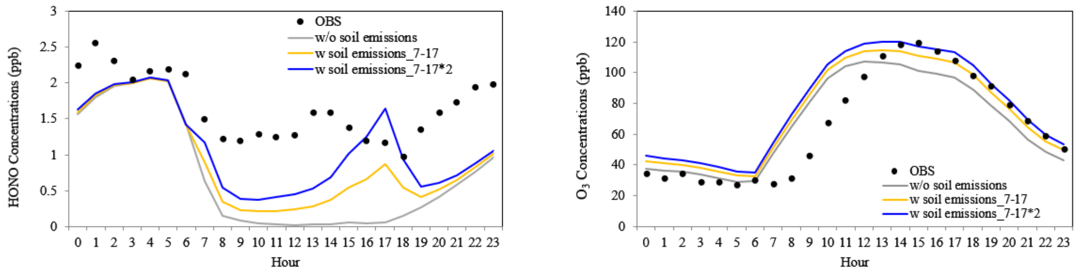

Figure 4.15 Model results for HONO and $O_3$ simulations with respect to the observations.

Table 4.3 Summary of modeled HONO and the observation in the daytime (7:00-17:00).

| | OBS | SIM | BIAS | NMB |
|---|---|---|---|---|
| no soil emissions | 1.32 | 0.11 | -1.21 | -92% |
| with soil emissions | 1.32 | 0.44 | -0.88 | -67% |
| 2*with soil emissions | 1.32 | 0.76 | -0.56 | -42% |

Table 4.4 Summary of modeled max-1hour $O_3$ and the observation in the daytime (7:00-17:00).

| | OBS | SIM | BIAS | NMB |
|---|---|---|---|---|
| no soil emissions | 123 | 110 | -13 | -11% |
| with soil emissions | 123 | 118 | -5 | -4% |
| 2*with soil emissions | 123 | 125 | 2 | 1% |

### 4.4.4 Regional impacts of soil HONO emissions in the NCP region

As shown in Figure 4.16, the soil HONO emissions increased the regional daytime average HONO concentrations by 0.22 ppbv (280%) and the largest enhancement can reach above 0.6 ppbv. Correspondingly, the regional max-1h $O_3$ and OH levels were increased by 7.56 ppbv (8%) and $5.18\times10^6$ molecules $cm^{-3}$ (37%), and the largest enhancements can reach above 15 ppbv and $15\times10^6$ molecules $cm^{-3}$, respectively.

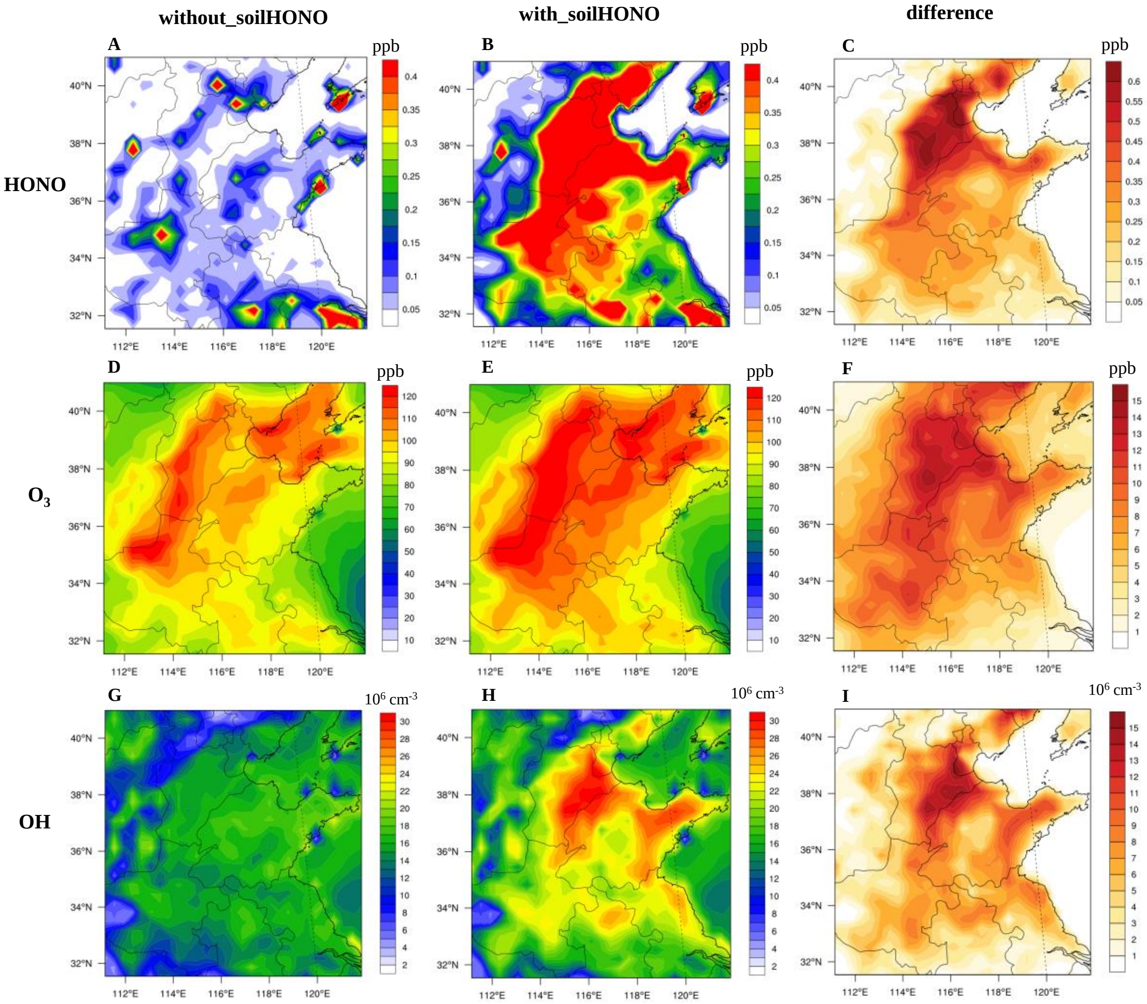

Figure 4.16 Regional distributions of daytime HONO concentrations (A-C), maximum 1h $O_3$ concentrations (D-F) and maximum 1h OH levels (G-I) for the simulations with and without soil HONO emissions and their difference.

## 4.5 Reduction strategy

As soil HONO emissions were originated from nitrification, nitrification inhibitors such as dicyandiamide (DCD) might reduce the emission. Figure 4.17 and Figure 4.18 showed the HONO and NO concentrations in the flow tube containing the fertilized soils with or without DCD, respectively. After ammonium fertilization (soil_f) or ammonium fertilization with DCD (soil_f_DCD), continuous measurement of HONO and NO emission was conducted for 7 days. Both the soil samples of soil_f and soil_f_DCD had no HONO or NO emissions on the first day just after the fertilization process. Soil_f_DCD showed peak emissions in the second day after fertilization with HONO and NO concentrations in the flow tube of about 20 ppbv and 10 ppbv, respectively. And since then, HONO and NO emissions started to reduce. After 7 days, there were no significant HONO or NO emissions. However, HONO and NO emissions by the soil_f continued to increase and reached peak emissions in the flow tube of about 120 ppbv HONO and 60 ppbv NO, respectively, on the third day after fertilization, which is in agreement of field campaigns. Since then, the emissions started to descend slowly but still had significant emissions after 7 days.

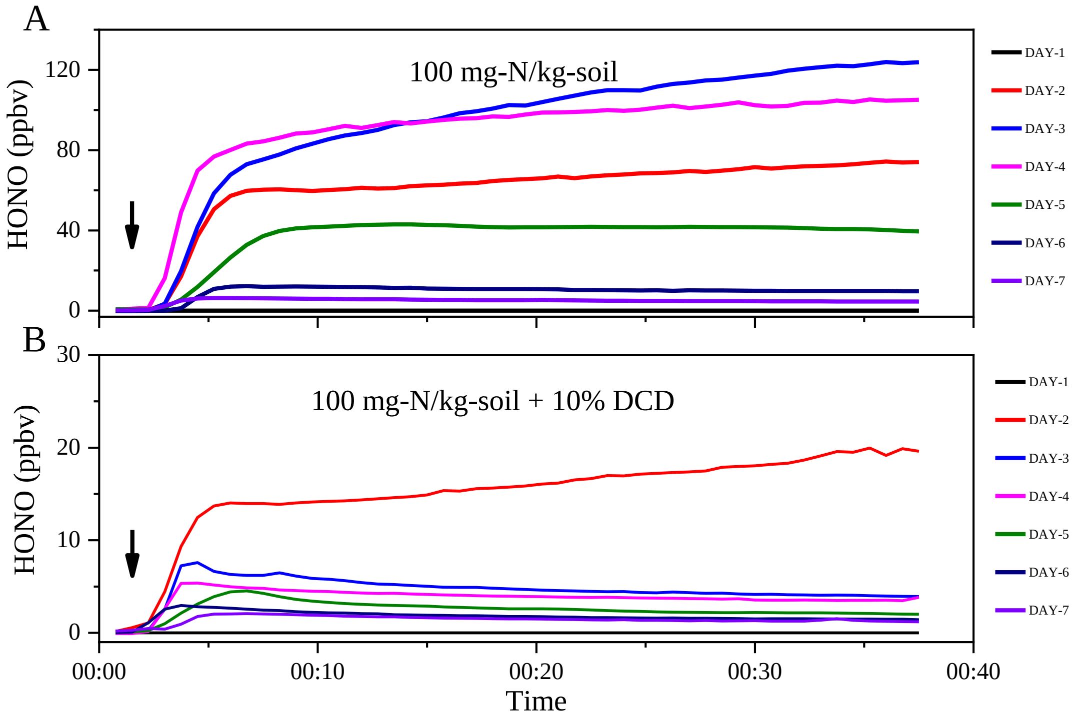

Figure 4.17 HONO concentrations in the flow tube containing the fertilized soils with or without nitrification inhibitor DCD. The black arrow represents the time when putting the soil samples into the flow tube.

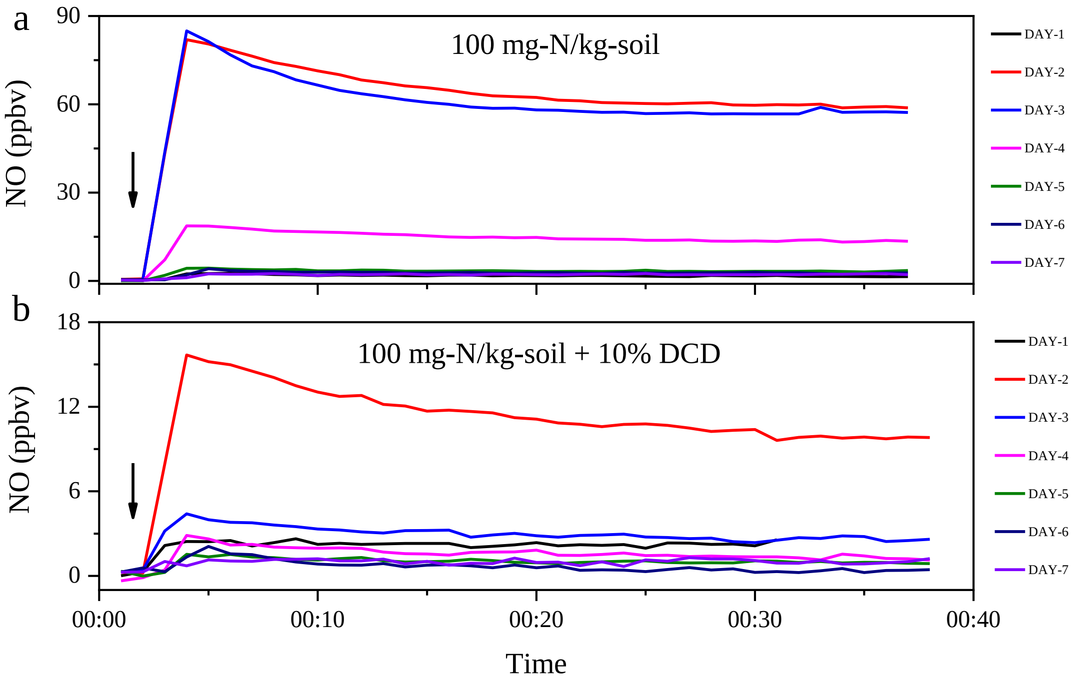

Figure 4.18 NO concentrations in the flow tube containing the fertilized soils with or without nitrification inhibitor DCD. The black arrow represents the time when putting the soil samples into the flow tube.

Figure 4.19 illustrated the daily variations in the HONO and NO concentrations measured at the exit of the flow tube during the period of emission measurements from the two treatments. Compared with soil_f, HONO and NO emissions from soil_f_DCD were clearly 5 times lower in every day of the 1-week measurement. In all, HONO and NO emissions with soil samples treated with DCD were reduced by 95% and 86%, respectively. If fertilization with DCD is popularly promoted and applied in the NCP, the reactive nitrogen gases, including HONO and NO, will be remarkably reduced, which is expected to mitigate the air pollution in the NCP. Likewise, the control measure proposed in this study might also be used in other agricultural regions with the application of chemical fertilizers.

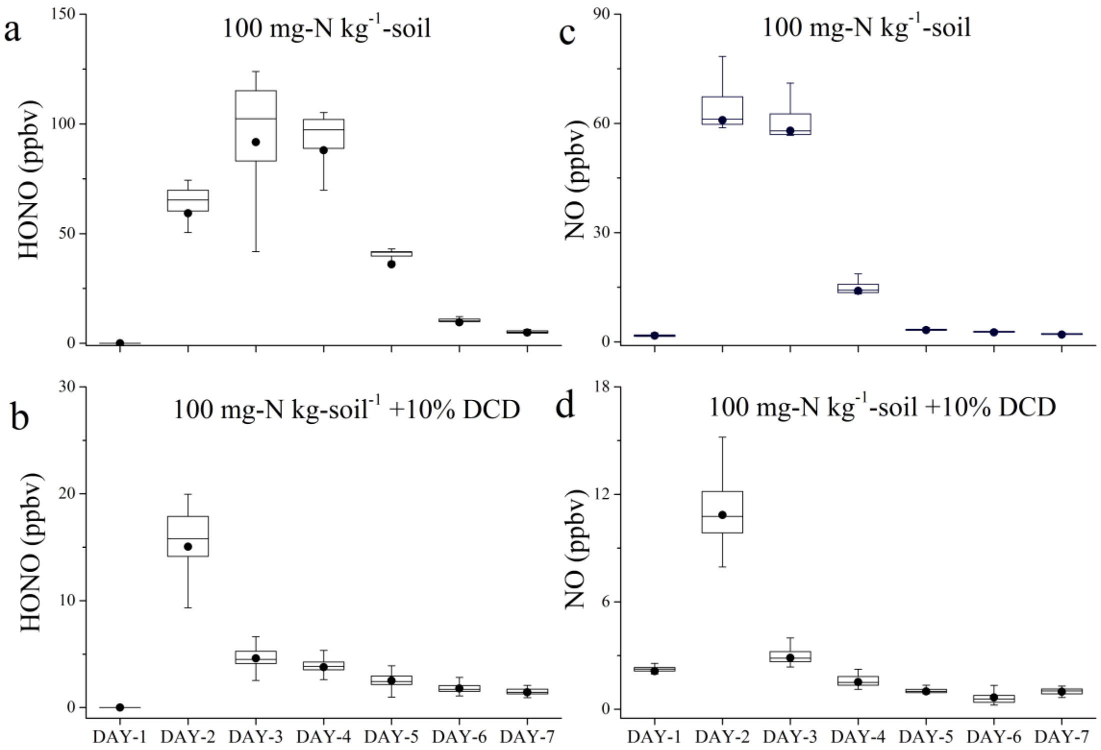

Figure 4.19 Daily variations in the HONO and NO concentrations measured at the exit of the flow tube during the period of emission measurements from the two treatments. The black boxes represent the 25th and 75th percentiles, and the whiskers provide the 10th and 90th percentiles of the HONO or NO concentrations. The black line and dot inside the box represent the median and average values, respectively. (A) & (B): HONO and NO concentrations for $NH_4Cl$ treatment. (C) & (D): HONO and NO concentrations for the treatment of $NH_4Cl$ plus DCD.

## 4.6 Summary and conclusions

Exceptional increases of HONO, $HONO/NO_2$, and $P_{unknown}$ were found over the agricultural field after the intensive fertilization, suggesting a strong additional HONO source that is not $NO_2$-related reactions. The high rise of $P_{unknown}$ occurred at noontime, from 3.1 ppbv $h^{-1}$ to 8.4 ppbv $h^{-1}$ (Table 4.2). Assuming a mixing layer height of 100-1000 m, the growth of $P_{unknown}$ indicated a soil HONO emission flux of 84-840 ng N $m^{-2}$ $s^{-1}$, which is 2-3 orders of magnitude higher than observations in other places[50,53] but comparable to the strong emissions in laboratory studies[66].

By using the SC-IC and OTC systems developed in this study, two field campaigns were carried out to measure soil HONO emission flux and related parameters in the summer of 2016 and 2017 in Dongbaituo Village, Baoding, Hebei. HONO emission flux from typical agricultural soil in the NCP was obtained by the OTCs system, and its impact on regional air quality was quantified by a chemistry transport model (CMAQ). The observations showed that the HONO emission flux rapidly increased after fertilization on the agricultural soil, and significant HONO emission was continuously observed in 15 days after fertilization. Besides, the observed emission flux exhibited an evident diurnal variation with a peak at noontime and a minimum at nighttime. The largest HONO emission reached 350 ng N $m^{-2}$ $s^{-1}$ after fertilization, which was 1-2 orders of magnitude higher than the reported values from limited studies. According to the relationship of HONO emission fluxes and the observed soil temperature and relative humidity (RH), the averaged diurnal variation of HONO emission flux was well reproduced by an Arrhenius equation. The parameterization was then adopted to the CMAQ model to explore the impact of soil HONO emission on regional air quality. Model results showed that daytime averaged levels of $O_3$ and OH in the NCP increased by about 8 ppbv and $5\times10^6$ molecules $cm^{-3}$, respectively, indicating the significant impact of the intensive fertilization process on agricultural soil on regional air pollution and atmospheric oxidizing capacity in the summertime of the NCP. More similar studies need to be conducted in this region or similar regions.

A new mechanism for soil HONO emission was proposed. Based on flow tube techniques, laboratory experiments were conducted to measure HONO and NO emission from a) original soil samples with ammonium fertilizers, b) sterilized soil samples with nitrate fertilizers, c) sterilized soil samples with ammonium fertilizers, and d) original soil samples with ammonium fertilizers and nitrification inhibitors. We found that only the original soil samples with ammonium fertilizers could significantly emit HONO and NO, indicating that the HONO emission was mainly from the nitrification process. During the nitrification process, $NH_4^+$ was converted to $NO_3^-$ by the nitrifying bacteria with intermediate products of $NO_2^-$ and $H^+$. The combination of $NO_2^-$ and $H^+$ increased the concentration of HONO in the soil solution environment, which promoted the release of HONO to the atmosphere.

Additionally, HONO and NO emissions increased with soil temperature in the range of 18-35 °C. Still, they decreased with the relative humidity of the flushing gas, which could well explain the observed diurnal variation of soil HONO emissions. On the one hand, the increase in soil temperature could accelerate nitrification activities; on the other hand, it reduced the solubility of HONO in soil solution and accelerate water evaporation from soil surfaces, which promoted the release of HONO from the soil. Similarly, high relative humidity of the flushing gas suppressed water evaporation from soil surfaces, leading to low HONO emissions from the soil.

The HONO emission investigated from the agricultural field might be representative of the NCP because of the similar soil characteristics and agricultural cultivation manners, which could be indirectly supported by the similar NO and $N_2O$ emissions from five different agricultural soils in the NCP. The extremely great HONO emission from the agricultural field must significantly contribute to atmospheric OH radicals to accelerate harmful secondary pollutant formation, e.g., under similar sunlight intensity, the levels of atmospheric HONO, $O_3$, $H_2O_2$ and $PM_{2.5}$ over the agricultural field remarkably increased after the focused fertilization event with respect to those levels before the event in June 2017. $O_3$ pollution in the NCP has become the most prominent atmospheric pollution problem during summer. The control measure for mitigating regional $O_3$ pollution is currently focusing on the $O_3$-VOCs-$NO_x$ sensitive chemistries. Still, it is facing a great challenge for rationally reducing VOCs or $NO_x$ due to their complex sources and the different reactivities of various VOCs. Tropospheric $O_3$ formation is essentially determined by the level of atmospheric OH radicals that initiate oxidation of the VOCs to form peroxy radicals, which accelerates the conversion efficiency of NO to $NO_2$ for $O_3$ formation. Whichever regional $O_3$ formation is sensitive to VOCs or $NO_x$, a reduction in the atmospheric OH level can efficiently mitigate the regional $O_3$ concentration. Considering the large fraction of OH radicals was from HONO photolysis, e.g., more than 56% in June 2014[7,162], and extremely strong HONO emissions from the agricultural fields during summer in the NCP, the reduction in HONO emissions from the agricultural fields is thought to be a good choice for mitigating $O_3$ pollution in this region because it is easy to implement through combination applications of the fertilizer with nitrification inhibitors. For example, a more than 90% reduction in HONO emission could be achieved with an application of $NH_4Cl$ (100 mg-N $kg^{-1}$-soil) and a nitrification inhibitor (dicyandiamide, DCD, 10 mg-DCD $kg^{-1}$-soil).

Because the soil nitrification process occurs in most soil environments and the diurnal variation trend of soil water loss is the same for various continental soils, the highest HONO emissions from the continental soils at noontime could be expected. They may be an essential reason for the strong daytime missing HONO sources reported in different areas. We suggest further direct HONO flux measurements from various fields to scientifically evaluate the influence of HONO emissions from soils on the regional air quality, global oxidizing capacity, and global N cycle.

# Chapter 5 HONO budget and its role in nitrate formation in the wintertime

In this chapter, a comprehensive field campaign with measurements on HONO, VOCs, J values, etc. and box model results are presented. Briefly, based on the winter field campaign conducted at a rural site of the North China Plain, a box model (MCM v3.3.1)[163] was used to simulate the daytime HONO budget and nitrate formation. We found that HONO photolysis acted as the dominant source for primary OH with a contribution of more than 92%. The observed daytime HONO could be well explained by the known sources in the model. The heterogeneous conversion of $NO_2$ on ground surfaces and the homogeneous reactions of NO with OH were the dominant HONO sources with contributions of more than 36% and 34% to daytime HONO, respectively. The contribution from the photolysis of particulate nitrate and the reactions of $NO_2$ on aerosol surfaces were found to be negligible in clean periods (2%) and slightly higher during polluted periods (8%). The relatively high OH levels due to fast HONO photolysis at the rural site remarkably accelerated gas-phase reactions, resulting in the fast formation of nitrate as well as other secondary pollutants in the daytime.

The work has been submitted to Environment Science & Technology. Details are as follows:

## 5.1 Field measurements

### 5.1.1 Site description and instrumentation

Field observation of HONO and related pollutants were conducted at the station of Rural Environmental, Chinese Academy of Sciences (SRE-CAS), located in Dongbaituo village (38°42′N, 115°15′E), Hebei province, China. The station was surrounded by agricultural fields planted with winter wheat. It is about 30 km in the southwest of Baoding city and 170 km to the southwest of Beijing. The nearest county seat, Wangdu, is about 10 km northwest to the station. The detailed information about the station has been well documented in our previous studies[7,162,164,165]. During the campaign from 3rd to 24th in December of 2017, a commercial LOPAP (QUMA, Model LOPAP-03) was used to measured HONO concentrations[86,87,166]. Other instruments for key-related species (VOCs, OVOCs, NO, $NO_2$, $NH_3$, $O_3$, $H_2O_2$, CO, $PM_{2.5}$, particle size distribution, and composition, etc.) and meteorological parameters (pressure, temperature, relative humidity (RH), J($NO_2$), etc.) are summarized in Table 5.1. The external sampling unit of LOPAP and inlets of other instruments were installed about 3.4 m above the ground level. The distance between every two inlets or sampling units were less than 20 m. Note that $NO_2$ measured by chemiluminescent technology used in this campaign may overestimate ambient $NO_2$ by the interference from HONO, $HNO_3$, etc., and the validation of $NO_2$ was therefore conducted in section 5.1.2.

Table 5.1. Instruments used during the campaign. WSIs: the water-soluble ions including $NO_3^-$, $Cl^-$, $SO_4^{2-}$, $NH_4^+$, $Na^+$, etc.

| Parameters | Measurement techniques | Time resolution |
|---|---|---|
| HONO | LOPAP-03, QUMA, Germany | 5 min |
| NO, $NO_2$ | Thermo Scientific 42i, USA | 1 min |
| CO | Thermo Scientific 48i, USA | 1 min |
| $SO_2$ | Thermo Scientific 43i, USA | 1 min |
| $O_3$ | Thermo Scientific 49i, USA | 1 min |
| J($NO_2$) | 4-π J($NO_2$) filter radiometer, Metcon Company | 1 min |
| WD, WS, RH, P, T | auto meteorological station, China | 1 min |
| $H_2O_2$ | AL2021, Aero-Laser, Germany | 1 min |
| VOCs | GC-MS/FID, ZF-PKU-VOC007 | 1 hour |
| OVOC | DNPH-Cartridge-HPLC, Wayeal, China | 2 hours |
| $PM_{2.5}$ | Thermo Scientific Sharp 5030i, USA | 1 min |
| WSIs | Tof-ACSM, Aerodyne Inc. | 10 min |
| $NH_3$ | homemade DOAS | 1 min |
| Aerosol size distribution | SMPS-TSI 3082, USA | 5 min |

### 5.1.2 $NO_2$ correction

The accurate quantification of $NO_2$ concentration is of significant importance for $NO_2$-

involved HONO formation paths. During the campaign, $NO_2$ was measured by Thermo Scientific Model 42i NO-$NO_2$-$NO_x$ analyzer using chemiluminescence technology to measure NO directly and a molybdenum $NO_2$-to-NO converter. A filter is used before sampling to remove particles. However, other nitrogen-contained gases such as HONO, nitric acid ($HNO_3$), peroxyacetyl nitrate (PAN), etc., could also be reduced to NO by the molybdenum converter, which overestimates atmospheric $NO_2$ concentrations. Thus, other $NO_y$ species like HONO, $HNO_3$, and PAN should be subtracted from measured $NO_2$ concentration. We measured HONO during the whole campaign and PAN from 15 December on, while no measurements for $HNO_3$ were available. Since PAN was found to be highly correlated to the measured $NO_2$ (r=0.82), we used this relationship to estimate PAN concentrations when they were experimentally not available before 15 December. The $HNO_3$ concentration, was expected to be lower than 1 $\mu g\ m^{-3}$ observer by Song et al. (2018) at an urban site of the NCP[167], which was too low to have an impact on the average $NO_2$ concentration of ca. 27 ppbv. Note that PAN concentrations were in the range of 0.1-1.5 ppbv, which were also much lower than $NO_2$ concentration. During all our analysis and modeling, the corrected $NO_2$ was used rather than the measured $NO_2$.

## 5.2 Model description

### 5.2.1 MCM

A 0-D box model MCM v3.3.1[163,168] was used to simulate the radical concentration and budget, the HONO budget and the potential particulate nitrate formation rate, P($pNO_3$), from gas-phase reaction $NO_2$+OH. The chemical mechanistic information was taken from the MCM v3.3.1 website (http://mcm.leeds.ac.uk/MCM)[163] as the basic mechanism for the simulation. The model was run from 3rd to 24th December 2017 with a time step resolution of 1 hour and initiated by a 2-day spin-up for the first day. All the photolysis frequencies, except J($NO_2$) that was scaled by the observations, were calculated by the model and were scaled by the ratio measured to modeled J($NO_2$).

Although atmospheric OH concentration is important for the HONO budget analysis, no radical measurements were available during this campaign. Therefore, we run the model with constraints on all measured parameters (case name: with HONO) to simulate the OH concentrations through the budget of its production rate and loss rate from each source. To reveal the contribution of atmospheric HONO to OH concentration and $P(pNO_3)$, another case with the constraints on all the measured parameters but without HONO (case name: without HONO) was also conducted.

### 5.2.2 Model Configurations

The basic mechanism for MCM v3.3.1 was obtained from http://mcm.leeds.ac.uk/MCM/. The model was constrained by the measured parameters including 71 VOCs and OVOCs, 7 inorganic gases (HONO, NO, $NO_2$, CO, $O_3$, $SO_2$, $H_2O_2$) and 4 meteorological parameters (temperature, pressure, RH, $J(NO_2)$).

Additionally, the ground surface area density ($S/V_{ground}$) is an important parameter to characterize ground-based HONO formation/emission in a box model. Here $S/V_{ground}$) is defined in this study as the inverse value of the mixing layer height (MLH)[169,170]. And the boundary layer height (BLH) is necessary to parameterize the deposition of trace gases in a box model. As BLH is the top of the boundary layer, a well-mixed layer was usually bellow BLH especially for ground-derived species because of their strong gradients[171–173]. Unfortunately, there were no measurements of MLH and BLH during the campaign. As the campaign happened in wintertime with an average temperature of ca. 0 °C and low wind speed with an average of $1.7 \pm 1.1$ m $s^{-1}$, a low MLH and a low BLH are suggested. Besides, our measurements were performed at ground level (sampling height = 3.4 m) for which ground surface process (emissions, deposition, etc.) are typically under-weighted in a box model. Therefore, the MLH varying from 25 m during the night to 50 m in the afternoon were used here. The comparable MLHs have been used or inferred from numerous studies[27,44,49,65,174,175], e.g., Lee et al. (2015)[174] used an MLH of 75 m in the summertime and they still found the contribution of the heterogeneous reaction of $NO_2$ on ground surface was underestimated because of the high MLH. In our study, we address the importance of ground-based HONO sources including $NO_2$ reaction on the ground surfaces and its contribution could be even larger under lower MLH conditions like winter stable atmospheric conditions. Similarly, relatively low BLHs of 200 m during the night and 500 m during the day were used here to scale the box height which will be used in the characterization of the deposition processes. Low BLH may overestimate the deposition process, however, the HONO loss through deposition was still almost negligible compared to photolysis during the daytime, which will be discussed in section 5.3.2.

Then we parameterized the proposed HONO sources and added each of them in the basic mechanism separately for sensitivity tests. Briefly, Table 5.2 summarizes the model configuration for HONO simulations of which 10 model scenarios from S-0 to S-9 were set. The scenario S-0 was the base case which only contained the default HONO source NO+OH. The scenarios from S-1 to S-6 were to test the sensitivity of each HONO source including direct emission, the dark $NO_2$ uptake on ground surfaces, the dark $NO_2$ uptake on aerosol surfaces, the photosensitized $NO_2$ uptake on ground surfaces, the photosensitized $NO_2$ uptake on aerosol surfaces, and the photolysis of particulate nitrate. For the photolysis frequency of $pNO_3$, $J(pNO_3)$, the same diurnal shape as the gas-phase photolysis of $HNO_3$ ($J(HNO_3)$) was assumed. Therefore, an enhancement factor ($EF = J(pNO_3)/J(HNO_3)$) due to faster particulate nitrate photolysis than gas-phase $HNO_3$[56] was deployed in the model to characterize the photolysis of particulate nitrate as well as the HONO production. For the sensitivity tests, a typical parameter (emission ratio for direct emission, $NO_2$ uptake coefficients for heterogeneous reaction and EF for particulate nitrate) and the upper/lower limit for each source were scaled by the proposed larger/smaller parameters or a variation factor (see section 5.2.3).

The photosensitized heterogeneous reaction of $NO_2$ on ground surfaces has been proved to possibly have a large impact on HONO budget[23,60,132], especially for ground base measurements like this study with a sampling height (3.4 m) close to the ground source. However, the impact may depend on the $NO_2$ levels, e.g., recent laboratory studies found that the photo-enhanced uptake coefficient of $NO_2$ on surfaces remarkably slowed down with increasing $NO_2$ concentration[23,25,26,65]. Considering atmospheric $NO_2$ concentrations at the sampling site were usually high during the most sampling periods, two additional scenarios S-8 and S-9 with reducing photosensitized $NO_2$ uptake coefficients by 30% and 60% were also tested.

Table 5.2. Configurations of the model simulations for different HONO source scenarios. α: the emitted ratio of HONO to $NO_x$ for direct emission; EF: enhancement factor of the photolysis frequency of particulate nitrate compared to that of gas-phase $HNO_3$ (EF= $J(pNO_3)/J(HNO_3)$). From S-1 to S-6, sensitivity tests on the sources were conducted with the corresponding parameters scaled by the typically used, the lower limit and the upper limit values.

| Scenarios | Configuration |
|---|---|
| S-0 | $NO + OH + M \rightarrow HONO + M$ |
| S-1 | S-0 + direct emission (α = 0.8%, 0.3%, 1.6%)[30–32,178] |
| S-2 | S-0 + dark $NO_2$ uptake on ground surfaces ($\gamma_1 = 1\times10^{-6}$, $0.2\times10^{-6}$, $5\times10^{-6}$)[23,46,61,64,179] |
| S-3 | S-0 + dark $NO_2$ uptake on aerosol surfaces ($\gamma_2 = 1\times10^{-6}$, $0.2\times10^{-6}$, $5\times10^{-6}$)[23,46,61,64,179] |
| S-4 | S-0 + photosensitized $NO_2$ uptake on ground surfaces ($\gamma_3 = 1.35\times10^{-5}$, $0.27\times10^{-5}$, $6.75\times10^{-5}$)[35,37] |
| S-5 | S-0 + photosensitized $NO_2$ uptake on aerosol surfaces ($\gamma_4 = 1.35\times10^{-5}$, $0.27\times10^{-5}$, $6.75\times10^{-5}$)[35,37] |
| S-6 | S-0 + photolysis of particulate nitrate (EF = 30, 1, 100)[53–56,180,181] |
| S-7 | S-0 + all the proposed sources |
| S-8 | S-7 with $0.7 \times \gamma_3$ |
| S-9 | S-7 with $0.4 \times \gamma_3$ |

### 5.2.3 Parameterization of HONO sources/sinks

#### *5.2.3.1 Conversion of $NO_2$ on the ground surfaces*

The heterogeneous conversion of $NO_2$ on ground surfaces can be a significant HONO source both in the dark[33,34,37,38] and also via photosensitized conversion[37,38,176]. The simplified reaction as shown in Eq (5.1) was parameterized in the model by the Eq (5.2).

$$NO_2 \rightarrow HONO \qquad (5.1)$$

$$P(HONO) = \frac{v(NO_2)\times[NO_2]}{4\times MLH}\times\gamma_1 \qquad (5.2)$$

Here P(HONO) is the average HONO production rate (molecules $cm^{-3}$ $s^{-1}$) for a homogeneous box of the MLH (mixing layer height), $\nu(NO_2)$ is the molecule speed of

$NO_2$ (m $s^{-1}$), $\gamma_1$ is the uptake coefficient of $NO_2$ on the ground surface, $[NO_2]$ is the corrected $NO_2$ concentrations with the unit converted from ppbv to molecules $cm^{-3}$. Here we use a $NO_2$ uptake coefficient of $1\times10^{-6}$ as the input in the model[30] and a variation by a factor of 5 to test the sensitivity of this process.

HONO formation by photosensitized conversion of $NO_2$ on the ground surfaces was parameterized by Eq (5.3):

$$P(HONO) = \frac{v(NO_2)\times[NO_2]}{4\times MLH} \times [\gamma_2 \times \frac{J(NO_2)_{measured}}{J(NO_2)_{noon}}] \qquad (5.3)$$

Here $\gamma_2$ is the light-enhance uptake coefficient of $NO_2$ on the ground surface and scaled by measured $NO_2$ photolysis frequency. Here we use a maximum noontime value of $1.35\times10^{-5}$ to explore this process on the HONO budget[38,39,176] and a variation by a factor of 5 to test the sensitivity.

### 5.2.3.2 Conversion of $NO_2$ on aerosol surfaces

The conversion of $NO_2$ on the aerosol surfaces can also be a HONO source by a dark reaction and by a photosensitized conversion as shown in Eq (5.1). The characterization of the dark and the photosensitized reactions are shown in equations (5.4) and (5.5).

$$P(HONO) = \frac{v(NO_2)\times PS\times[NO_2]}{4} \times \gamma_3 \qquad (5.4)$$

$$P(HONO) = \frac{v(NO_2)\times PS\times[NO_2]}{4} \times [\gamma_4 \times \frac{J(NO_2)_{measured}}{J(NO_2)_{noon}}] \qquad (5.5)$$

Here $\gamma_3$ and $\gamma_4$ represent the uptake coefficients of $NO_2$ on the aerosol surfaces for the dark reaction and the photosensitized reaction, respectively. PS represents the aerosol surface density ($m^{-1}$) based on the measured aerosol size distribution. Similar to the reactions on the ground surfaces, the same kinetic values ($\gamma_3 = \gamma_1$, $\gamma_4 = \gamma_2$) and variation factor for sensitivity study were applied in the model simulations.

### 5.2.3.3 Particulate nitrate photolysis

Photochemical HONO production from particulate nitrate ($pNO_3$) photolysis can be a source as is shown in the simplified reaction (5.6). The parameterization was expressed by equation (5.7):

$$\mathrm{pNO_3} + \mathrm{h\upsilon} \rightarrow \mathrm{HONO} \qquad (5.6)$$

$$P(HONO) = [\mathrm{pNO_3}] \times J(HNO_3) \times \mathrm{EF} \qquad (5.7)$$

Here $[pNO_3]$ is the observed particulate nitrate concentration with the unit converted from μg $m^{-3}$ to molecule $cm^{-3}$. $J(HNO_3)$ is the photolysis frequency of gas-phase $HNO_3$ calculated by the MCM model and scaled by the measured $J(NO_2)$. EF is the enhancement factor of the photolysis frequency of $pNO_3$ to that of gas-phase $HNO_3$. Laboratory studies[52,55,56] have revealed that $J(pNO_3)$ is in the range of $6.2\times10^{-6}$ to $5\times10^{-4}$ $s^{-1}$, which could be 1-3 orders of magnitude higher than the photolysis frequency of $HNO_3$ in the gas phase or adsorbed on pure glass substrates (few times $10^{-7}$ $s^{-1}$ in MCM model)[51]. However, a recent study found $J(pNO_3)$ was only 1-30 times faster than gas-phase photolysis[58]. Therefore, we use an EF of 30 for model simulation and two EFs of 1 and 100 were used to test the sensitivities of this process. Note that the lower limit of EF = 1 means the photolysis frequency of particulate nitrate is the same as $HNO_3$ in the gas phase.

#### 5.2.3.4 Soil emissions

According to the studies of Oswald et al. (2013)[150] and Scharko et al. (2015)[68], the microbiologic formation of nitrite was proposed as a ground source of HONO. Proper temperature (20-40 °C), nitrogen fertilizer (mainly ammonium fertilizer) and low soil water content (<30% water holding capacity) were the key factors influencing this process in their laboratory studies. However, during the present winter campaign, the average temperature was near 0 °C and there was no fertilization. Additionally, the previous studies have revealed that the water content was high and there were almost no NO and $N_2O$ emissions at this site in winter[144]. Therefore, HONO emissions from the soil were not considered in the model.

#### 5.2.3.5 Other sources

Direct emission from the combustion process has been proved to be a source for HONO and the emission ratio of HONO to $NO_x$ was found to be in the range of 0.3%-1.6%[30,182]. Here we obtained the $NO_x$ emission flux from a WRF-Chem inventory from Zhang et al. (2019)[136] and the inventory was proved to well reproduce the observed $NO_x$ concentration in the NCP. The medium direct emission ratio of HONO to $NO_x$, 0.8%, was used here to represent the direct HONO emission contribution[30,182]. Besides, the emission ratios of 0.3% and 1.6%, were also used here to represent the lower limit and upper limit of the contribution of direct HONO emission, respectively.

The displacement of HONO by atmospheric strong acids such as $HNO_3$ and HCl was also proposed as a daytime HONO source[59]. However, concentrations of inorganic acids including HCl and $HNO_3$ in the NCP in winter were found to be very low and sometimes below the detection limit measured by Song et al. (2018)[116] The photolysis of adsorbed $HNO_3$ on ground surface was not included in our model simulation because of the following two reasons: a) the concentration of $HNO_3$ was too low compared to other HONO precursors such as NO, $NO_2$, and $pNO_3$, and b) the photolysis of $HNO_3$(g), as well as adsorbed $HNO_3$ and the displacement of HONO by the deposition of atmospheric strong acids were proved to have a negligible impact on HONO budget in summer at this site[60] and the concentrations of the acids were expected to be lower than in summer.

Based on measurements in the free troposphere, the reaction of $NO_2$ with $HO_2{\cdot}H_2O$ complex was proposed as a significant HONO source[72]. However, a recent field campaign found a negligible impact of this reaction on the HONO budget[73]. Photolysis of ortho-nitrophenols[74] can also produce HONO while it has been proved to have a negligible impact on the HONO budget at this site and other sites[60]. The reaction of excited $NO_2$ with $H_2O$ ($NO_2^*$+$H_2O$) could be a HONO source but it is still rebutted by other studies[75,76]. Therefore, these processes are not included in our model.

#### 5.2.3.6 HONO sinks

By default, the mechanism (MCM v3.3.1) contains two HONO sinks: photolysis and the reaction with OH. The deposition was added in the mechanism based on the HONO deposition velocity and boundary layer height (BLH). Note that the HONO deposition velocity, ν(HONO), was obtained from a temperature-dependent equation from Laufs et al. (2015)[64]:

$$\nu(\mathrm{HONO}) = \exp\left(\frac{23920}{T} - 91.5\right) \quad (5.8)$$

where T is the temperature in K. For the average temperature of the present campaign, ν(HONO) was 0.016 m $s^{-1}$.

## 5.3 Results and discussion

### 5.3.1 Overview of the observations

Figure 5.1 shows the time series of temperature (Temp, pink line) and relative humidity (RH, green line), wind direction (WD, dark yellow line) and wind speed (WS, black line) concentrations measured during the campaign. The atmospheric temperature during the measurement period varied from -6 to 12 °C. It is relatively low with an average of ca. 0.6 °C. Atmospheric RH varied from 20% to 80% with an average of 37%. The highest RH appeared at midnight of 15th December when the temperature and wind speed was relatively low.

Figure 5.2 shows the wind rose of the observed wind direction and wind speed. The main wind direction during the campaign was from southwest to northwest. Most of the wind speed was less than 4 m $s^{-1}$ with a small average of 2 m $s^{-1}$, which was not in favor of the diffusion of pollutants but in favor of the regional accumulation of pollution.

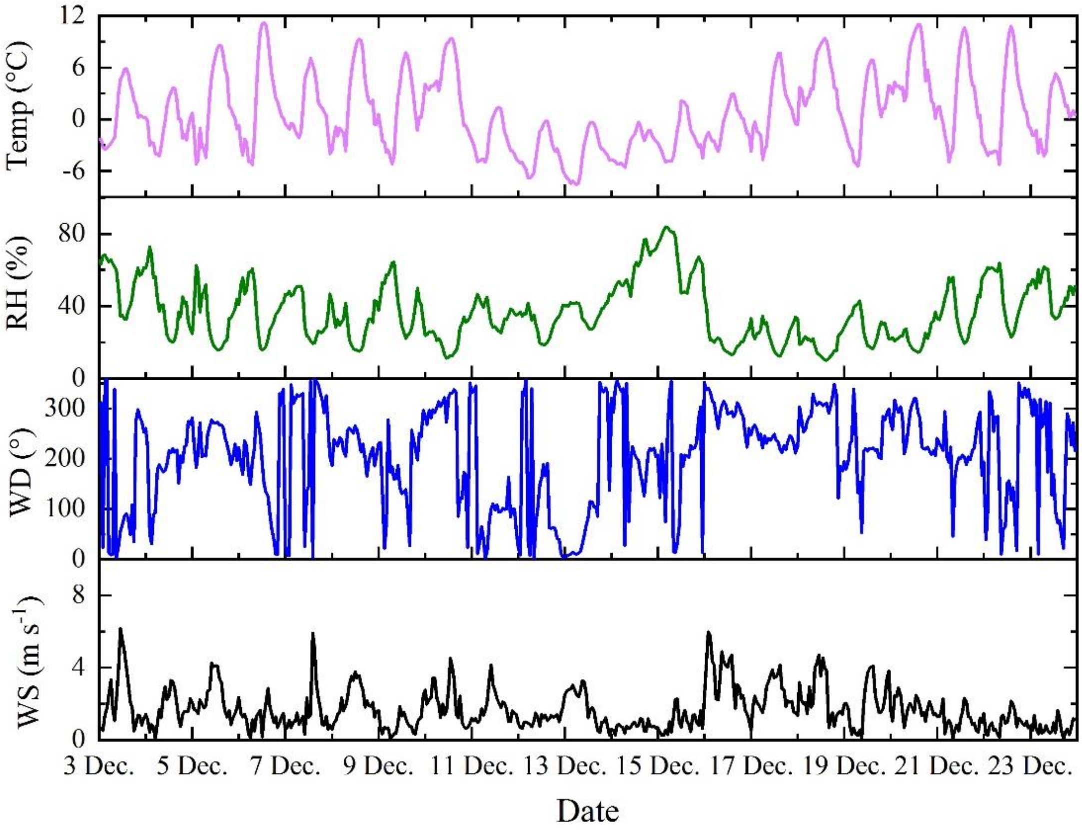

Figure 5.1 Time series of temperature (Temp, pink line) and relative humidity (RH, green line), wind direction (WD, dark yellow line) and wind speed (WS, black line) concentrations measured during the campaign.

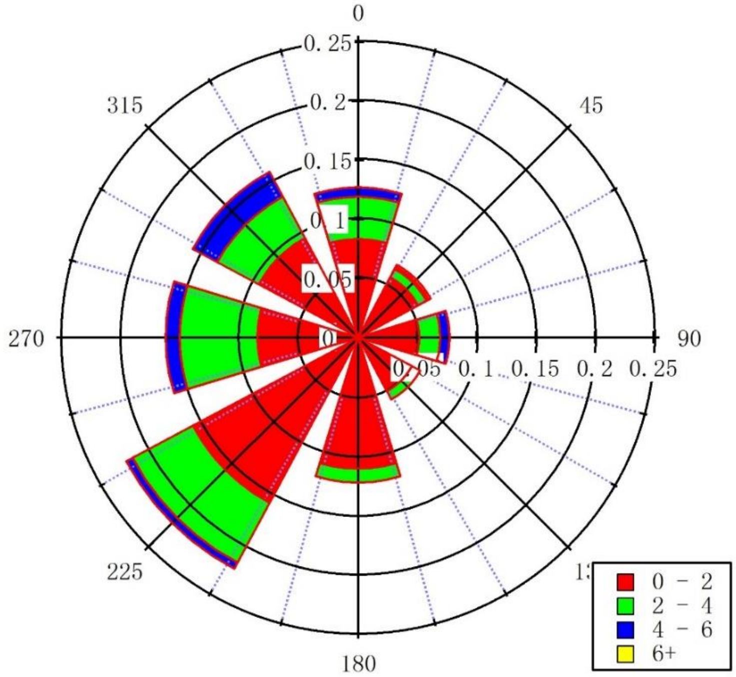

Figure 5.2 The wind rose diagrams during the campaign.

Figure 5.3 shows the time series of CO (pink line) and $SO_2$ (green line), particle surface density (PS, dark yellow line) and ammonia ($NH_3$, black line) concentrations measured during the campaign. High CO mixing ratios were frequently observed with a variation from 0.3 to 8 ppmv and an average of ca. 2 ppmv. $SO_2$ mixing ratios were normally lower than 20 ppbv while high mixing ratio up to 90 ppbv was also found at midnight of 7 December. $NH_3$ mixing ratios were normally lower than 50 ppbv while high mixing ratio up to 140 ppbv was also found at night of 9, 23 and 24 December.

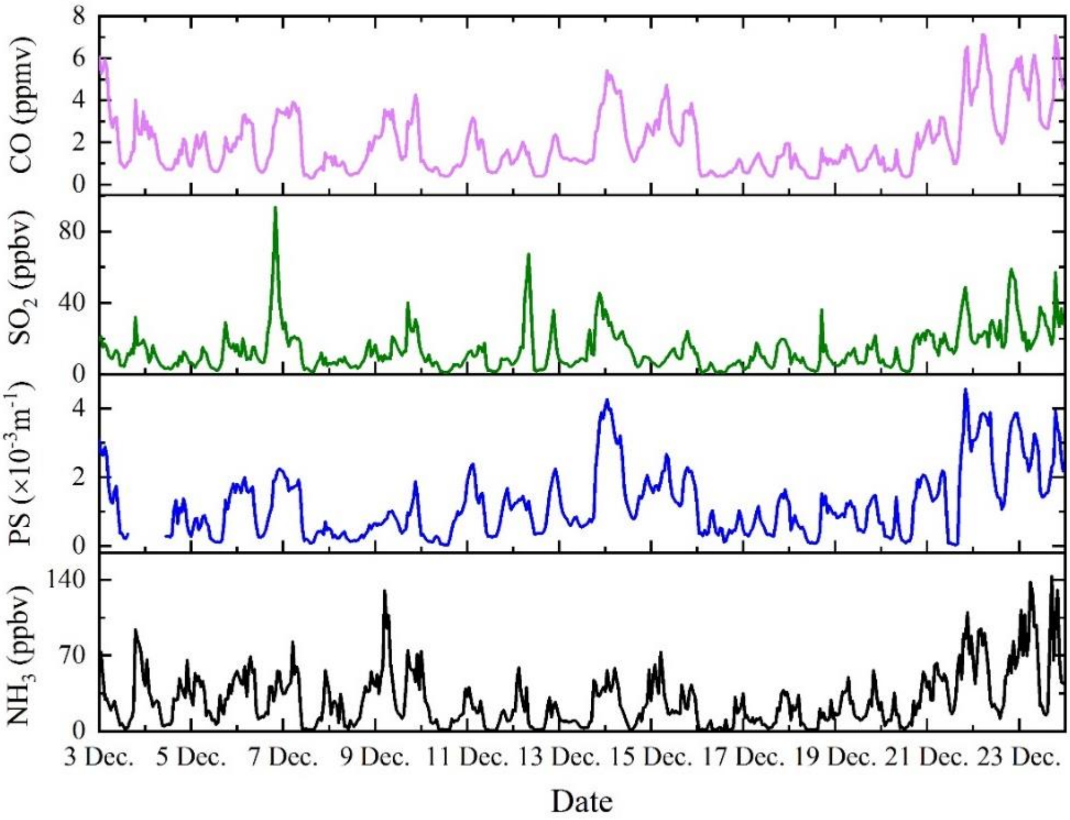

Figure 5.3 Time series of CO (pink line) and $SO_2$ (green line), particle surface density (PS, dark yellow line) and ammonia ($NH_3$, black line) concentrations measured during the campaign.

Time series of HONO, particulate matter with a diameter of less than 2.5 µm ($PM_{2.5}$), particulate nitrate ($pNO_3$), NO, $NO_2$, $O_3$, photolysis frequency of $NO_2$ ($J(NO_2)$) and NOR (nitrogen oxidation ratio, $NOR = \frac{n\,NO_3^-}{n\,NO_3^- + n\,NO_2}$)[183] are shown in Figure 5.4. Air pollution at this rural site was very serious, e.g., the hourly levels of $PM_{2.5}$ and $NO_x$ ($NO+NO_2$) frequently exceeded 100 µg $m^{-3}$ and 100 ppbv, respectively. The daily average levels of HONO, $PM_{2.5}$, $pNO_3$, NO and $NO_2$ were 1.8±1.4 ppbv, 98±112 µg $m^{-3}$, 8.0±7.0 µg $m^{-3}$, 45±62 ppbv and 27±14 ppbv, respectively. In particular, the averaged daytime (7:00-17:00 local time) HONO mixing ratio at this site could achieve as high as 1.3±1.3 ppbv, which was remarkably higher than those observed in European cities[184,185], American cities[186], but comparable to those observed in the NCP[8,9] and Santiago de Chile[5]. The averaged daytime HONO/$NO_x$ ratio was 3.3% ± 1.7% which was much higher than those from direct emission (0.3%-1.6%)[30–32,178], suggesting atmospheric HONO at the rural site was dominated by the sources other than direct emission especially after considering the much longer lifetime of $NO_x$ than HONO during the daytime. The relatively high levels of HONO at the rural site were suspected to be the dominant source for atmospheric OH, and thus played an important role in the formation of secondary pollutants, e.g., evident and frequent increase of NOR and $pNO_3$ concentrations during the daytime could be identified in Figure 5.4.

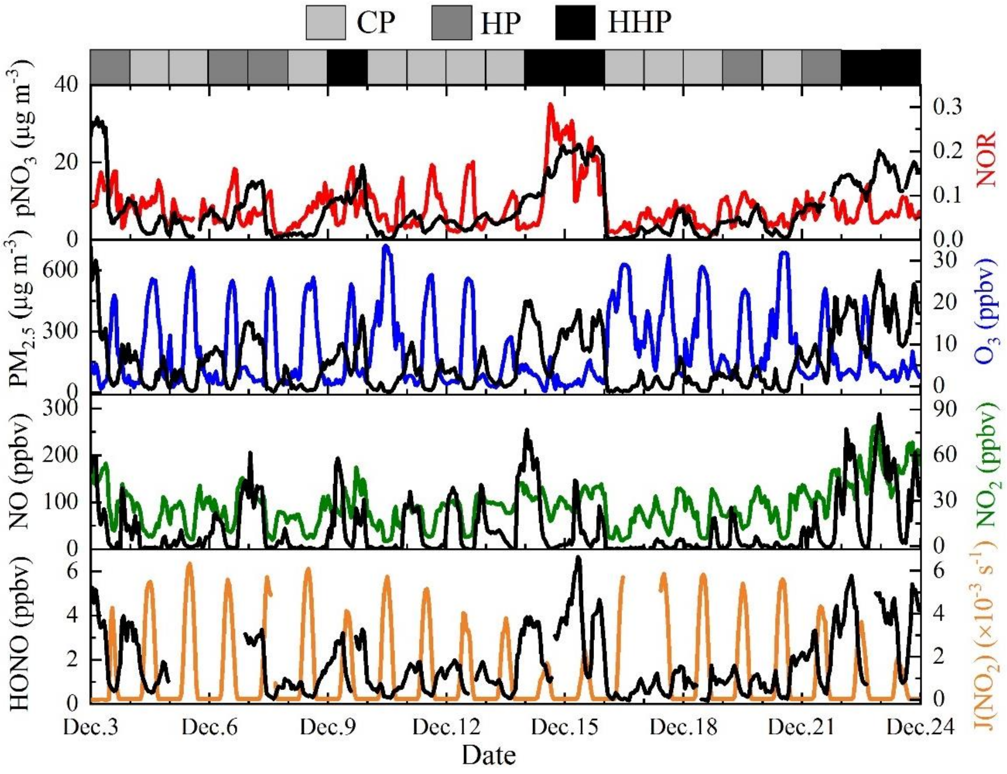

Figure 5.4 Time series of HONO and related parameters measured during the campaign. The light gray, dark gray and black areas on the top part represent the pollution levels of the clean periods (CP), haze periods (HP) and heavy haze periods (HHP), respectively. On the left axis, HONO, NO, $PM_{2.5}$ and $pNO_3$ (particulate nitrate) are shown in black lines in each layer from bottom to the top. $J(NO_2)$ (photolysis frequency of $NO_2$), $NO_2$, $O_3$, and NOR (nitrogen oxidation ratio) are shown in yellow, green, blue and red lines on the right axis, respectively.

To better understand the daytime sources for HONO as well as the interaction between HONO and nitrate, the field data were classified into three classes: clean periods (CP, 11 days) when the averaged $PM_{2.5}$ concentrations during daytime were below 50 μg $m^{-3}$, haze periods (HP, 5 days) when $PM_{2.5}$ concentrations were in the range of 50-150 μg $m^{-3}$ and heavy haze periods (HPP, 5 days) when $PM_{2.5}$ concentrations were above 150 μg $m^{-3}$. The averaged diurnal variations and concentrations of HONO and related parameters during different pollution periods are shown in Figure 5.5 and Table 5.3.

Daytime HONO increased by a factor of 3 during the HPP relative to the CP. Hence, more OH radicals could be produced through HONO photolysis in the HPP even though the solar intensity decreased by a factor of 2. Besides, $NO_2$ during the HPP also increased by a factor of 3 relative to the CP, which would promote the reaction of $NO_2$ with OH, leading to the faster daytime particulate nitrate formation during the HHP. Furthermore, the extremely high mixing ratios of HONO precursors, including $NO_x$ and particulate nitrate during the HHP might also accelerate HONO formation through the heterogeneous reactions of $NO_x$ or photolysis of particulate nitrate, resulting in a remarkable increase of HONO during HPP.

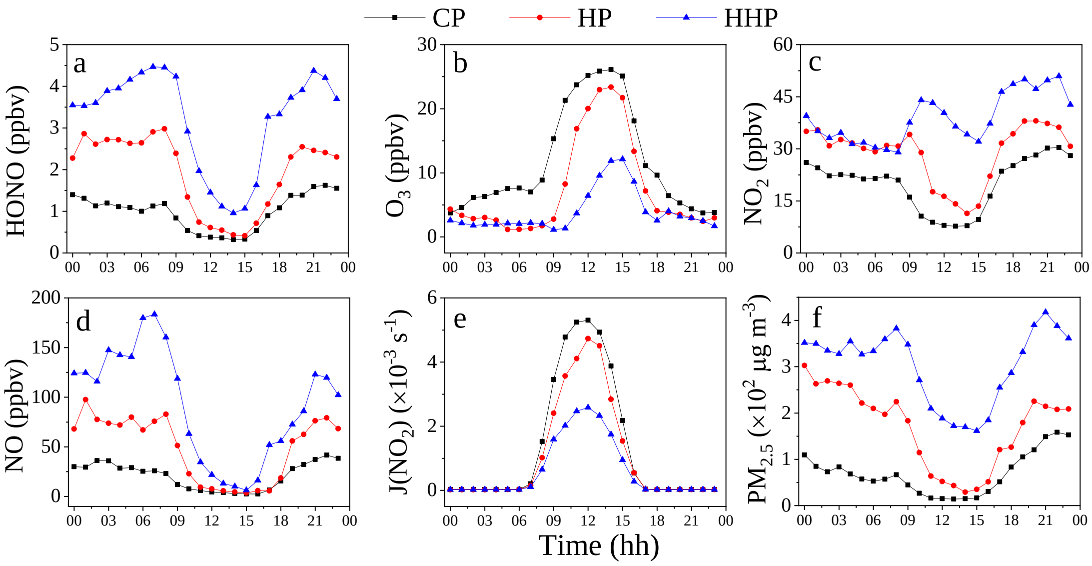

Figure 5.5 Diurnal profiles of HONO and other related parameters ($O_3$, $NO_2$, NO, J($NO_2$) and $PM_{2.5}$) averaged from all data of the three periods. CP: clean periods; HP: haze periods; HHP: heavy haze periods.

Table 5.3 Averaged concentrations of HONO and related parameters at different pollution levels. CP: clean periods; HP: haze periods; HHP: heavy haze periods.

| Periods | CP | | HP | | HHP | |
|---|---|---|---|---|---|---|
| Parameters | Daytime | All-day | Daytime | All-day | Daytime | All-day |
| NO (ppbv) | 9±16 | 21±36 | 27±34 | 49±52 | 63±68 | 92±83 |
| $NO_2$ (ppbv) | 13±8 | 20±10 | 22±12 | 29±12 | 36±11 | 39±14 |
| $O_3$ (ppbv) | 20±9 | 12±10 | 13±9 | 7.4±7.9 | 5.9±7.0 | 3.9±5.0 |
| HONO (ppbv) | 0.6±0.4 | 1.0±0.7 | 1.3±1.1 | 2.0±1.4 | 2.5±1.7 | 3.3±1.5 |
| HCHO (ppbv) | 2.3±0.5 | 2.7±1.0 | 3.8±1.2 | 4.2±1.4 | 6.2±2.2 | 5.6±2.5 |
| $H_2O_2$ (ppbv) | 0.19±0.16 | / | 0.32±0.27 | / | 0.33±0.37 | / |
| $J(NO_2)$ ($10^{-3}$ $s^{-1}$) | 3.2±2.0 | / | 2.5±2.0 | / | 1.5±1.1 | / |
| $pNO_3$ (μg $m^{-3}$) | 2.1±1.6 | 3.5±2.4 | 7.3±6.6 | 9.1±7.4 | 15.3±4.4 | 16.6±4.7 |
| $PM_{2.5}$ (μg $m^{-3}$) | 30±26 | 69±64 | 99±88 | 169±141 | 244±107 | 301±120 |

### 5.3.2 OH simulations

Radical levels were not directly measured in the present study. However, as the knowledge about OH levels is of paramount importance for HONO simulation, we modeled the OH concentrations and compared them with direct OH measurements in winter of the NCP and other places from other studies. The time series of simulated OH concentrations are shown in Figure 5.6. The averaged noontime OH concentrations of $3.3\times10^6$, $3.1\times10^6$, and $1.3\times10^6$ molecules $cm^{-3}$ in clean (CP), haze periods (HP), and heavy haze periods (HHP), respectively, are comparable with direct winter noontime OH observations in Beijing Huairou district ($2.8\times10^6$ molecules $cm^{-3}$)[6], Beijing downtown ($2\times10^6$ molecules $cm^{-3}$ for clean periods and $1.5\times10^6$ molecules $cm^{-3}$ for polluted periods)[187], Birmingham ($1.7\times10^6$ molecules $cm^{-3}$)[184] and Boulder ($2.7\times10^6$ molecules $cm^{-3}$)[4].

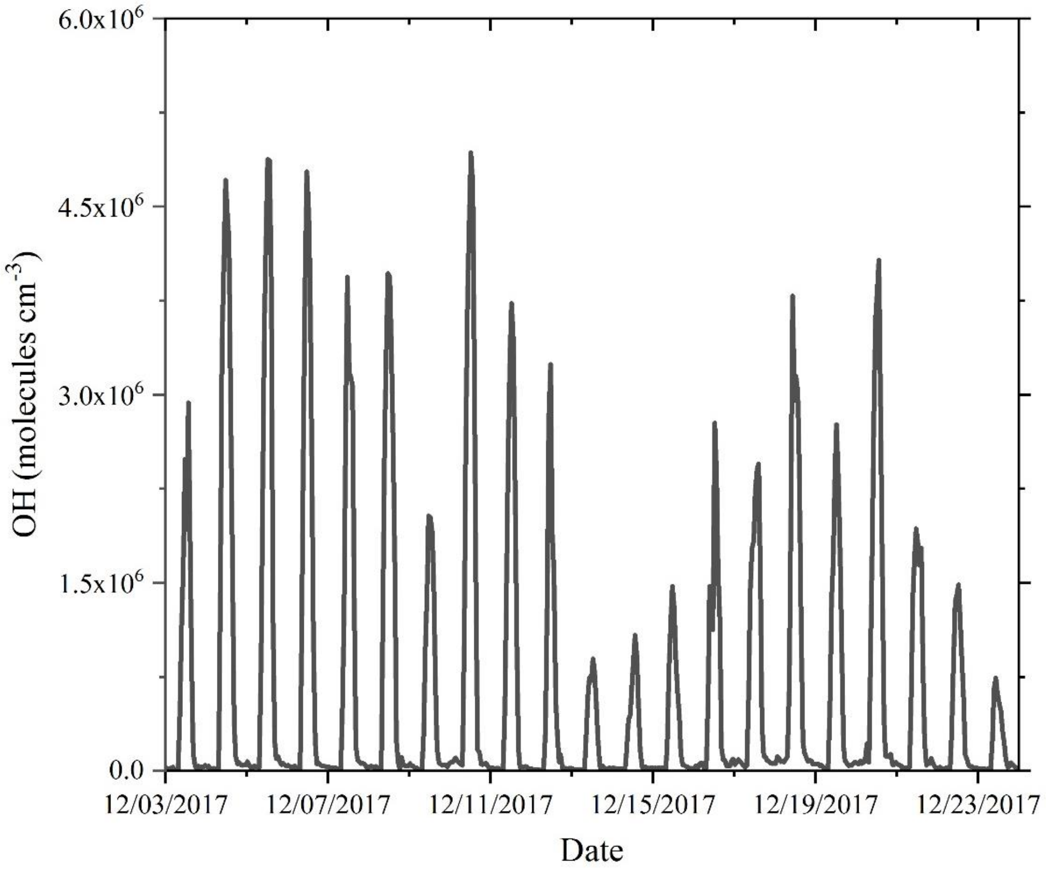

Figure 5.6 Time series of the simulated OH concentration.

### 5.3.3 HONO simulations and budget

Model results from the base case (S-0) and sensitivity tests on each HONO source (S-1 to S-6) are shown in Figure 5.7 and Figure 5.8. Obviously, the default HONO source from the homogeneous reaction of NO with OH (S-0) was too small to explain the observations (Figure 5.7), suggesting additional daytime HONO sources. With the presence of direct emission (S-1), the dark heterogeneous reactions of $NO_2$ on the ground surfaces (S-2), or aerosol surfaces (S-3), the modeled daytime HONO was still much lower than the observations (Figure 5.7). The modeled HONO concentrations were basically in line with the observations during most of the daytime (from 10:00 to 15:00) when a median value of the uptake coefficient was adopted for the photosensitized heterogeneous reaction of $NO_2$ on ground surfaces. However, there were still large overestimations by using the upper limit and underestimations by using the lower limit of the uptake coefficients (Figure 5.8 (A), (B), (C)). In contrast, both the photo-enhanced sources of the photosensitized heterogeneous reaction of $NO_2$ on aerosol surfaces and the photolysis of particulate nitrate showed a negligible impact on daytime HONO formation even when the uptake coefficient or EF were enlarged (from Figure 5.8 (D) to (I)). The large difference for the sensitivities between the photosensitized heterogeneous reactions of $NO_2$ on ground surfaces and particle surfaces was mainly ascribed to the much larger S/V ratio of ground surfaces than that of particle surfaces (e.g., an average of $1.2\times10^{-3}$ $m^{-1}$ in this study)[47,174,188] with the similar $NO_2$ uptake kinetics on particle and ground surfaces.

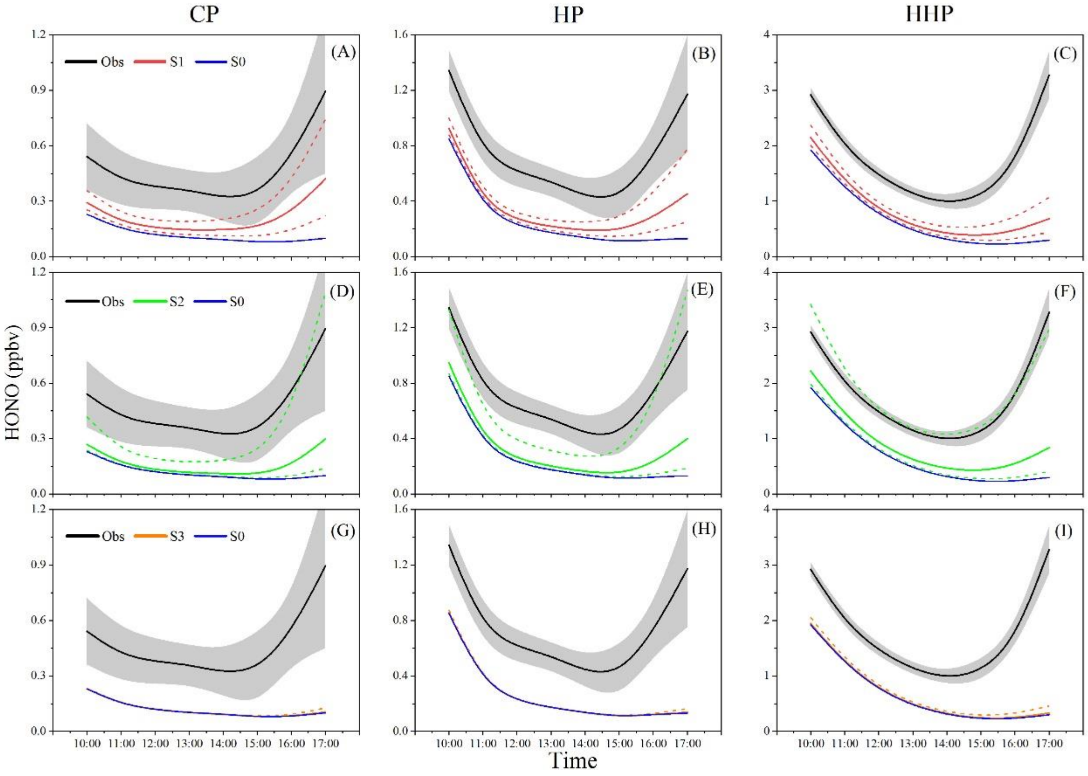

Figure 5.7 Model results of diurnal profiles of simulated HONO from sensitivity tests S-1 to S-3 with respect to the base case S-0 and the observation. Throughout the whole graph, the black lines represent the observed diurnal HONO variation with the standard deviation as the shaded area and the blue lines show the modeled HONO concentrations in S-0. The red, green and orange lines represent the modeled HONO results in the sensitivity tests S-1 for direct emission, S-2 for dark $NO_2$ uptake on the ground surfaces, and S-3 for the dark $NO_2$ uptake on the aerosol surfaces, respectively. The dashed lines represent the upper and lower HONO concentrations of the sensitivity tests. Similar to the observation, all the model results were classified into three periods to assess the model performance in different pollution levels (CP: clean periods, HP: haze periods, HHP: heavy haze periods).

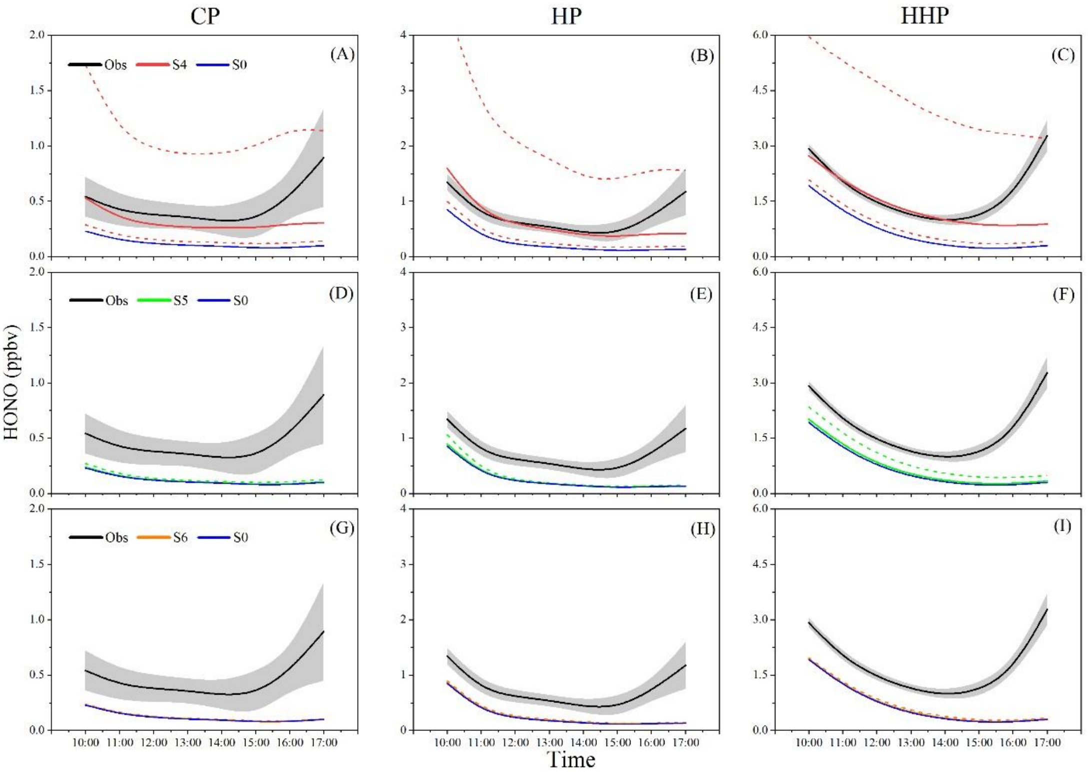

Figure 5.8 Model results of diurnal profiles of simulated HONO from sensitivity tests S-4 to S-6 with respect to the base case S-0 and the observation. Throughout the whole graph, the black lines represent the observed diurnal HONO variation with the standard deviation as the shaded area and the blue lines show the modeled HONO concentrations in S-0. The red, green and orange lines represent the modeled HONO results in the sensitivity tests S-4 for the photosensitized $NO_2$ uptake on the ground surfaces, S-5 for the photosensitized $NO_2$ uptake on the aerosol surfaces, and S-6 for the photolysis of particulate nitrate, respectively. The dashed lines represent the upper and lower HONO concentrations during the sensitivity tests. Similar to the observation, all the model results were classified into three periods to assess the model performance in different pollution levels (CP: clean periods, HP: haze periods, HHP: heavy haze periods).

Figure 5.9 shows the model results of scenarios from S-7 to S-9 with inputting all the additional sources. With the normal photosensitized $NO_2$ uptake coefficient on the ground surfaces (S-7), the model could well reproduce the observed daytime HONO during the CP (Figure 5.9A) but distinctly overestimated HONO during the HP and HHP (Figure 5.9B and C). In the scenario S8, the photosensitized $NO_2$ uptake coefficient was reduced by 30%, for which modeled HONO was much closer to the observation during the HP (Figure 5.9E) but still higher than the observation during the HHP (Figure 5.9F) before 15:00 and lower than the observation after 15:00. The observed HONO during the HHP could be partially reproduced when the photosensitized $NO_2$ uptake coefficient was reduced by another 30% in S-9 (Figure

5.9I). The modeled HONO in S-9 could well explain the observation in the morning and noontime but still underestimated HONO in the late afternoon, which was perhaps caused by an overestimation of MLH leading to the underestimation of HONO formation from the $NO_2$ uptake on the ground surfaces.

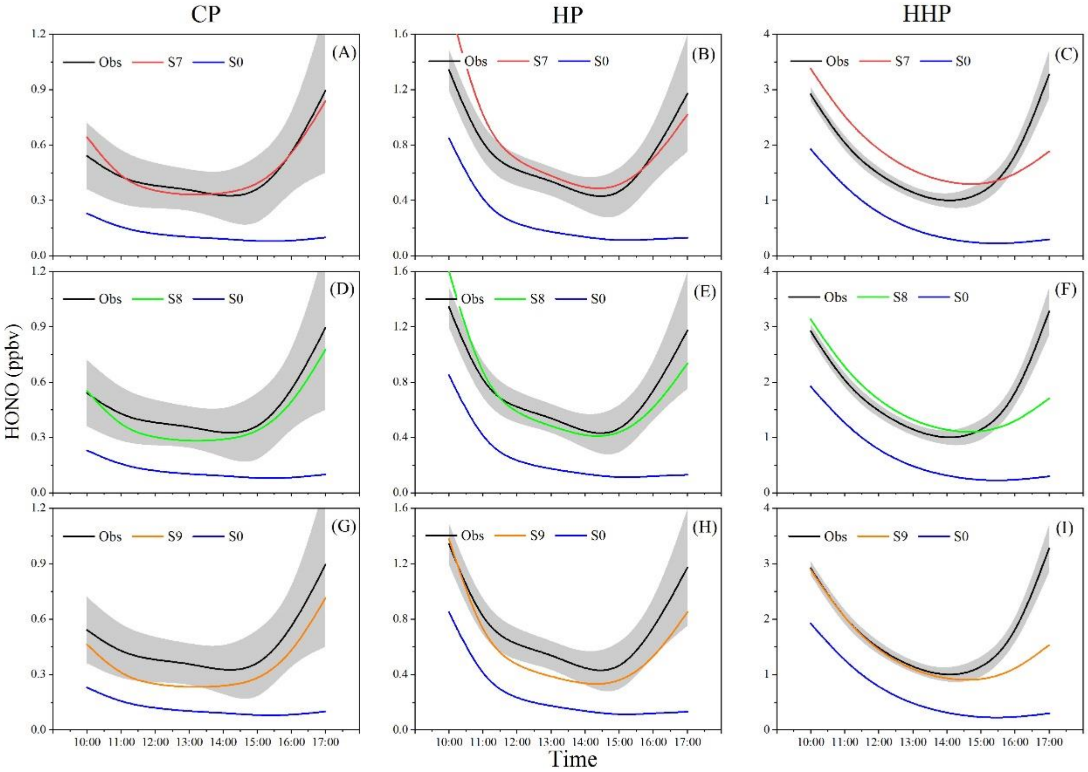

Figure 5.9 Model results of diurnal profiles of simulated and observed daytime HONO during different periods (CP: clean periods, HP: haze periods, HHP: heavy haze periods). Throughout the whole graph, the black lines represent the observed average diurnal HONO variation with the standard deviation as the shaded area. The blue lines represent the model HONO mixing ratios in the base case S0. The red, green and orange lines represent the model HONO results in the case S7, S8 and S9, respectively. Similar to the observation, all the model results were classified into three periods to assess the model performance during different pollution periods.

With gradually reducing the photosensitized $NO_2$ uptake coefficients, the model performance on HONO simulations for the polluted periods (HP and HHP) was largely improved, verifying that the $NO_2$ uptake coefficients depended on the pollution levels of $NO_2$ as observed in laboratory studies[23,25,26]. Although in some model studies the uptake coefficients were already scaled by RH and light-intensity[47,135] leading to a significant improvement to explore the HONO budget and the SOA formation[132,135], etc., the still existing differences between observations and simulations are possibly caused by the missing parameterization of the $NO_2$ uptake kinetics by the pollution levels as discussed in the present study for the first time. The observed HONO in different pollution periods was well reproduced by the model, implying that more similar analysis is still necessary to better understand HONO formation by the models in the polluted areas like the NCP.

The diurnal HONO budget and the relative contribution from each source during each period are shown in Figure 5.10. Contributions to the HONO budget from each source at different daytime hours (local time) and the HONO budget are shown in Figure 5.11 and Figure 5.12, respectively. Apparently, the total HONO sink strength was slightly larger than the total source strength in the daytime, which was consistent with the daytime decreasing trend of the observed HONO. Among the six HONO sources, the homogeneous HONO formation from the gas phase reaction of NO+OH always acted as one of the most important sources for HONO, accounting for 33.6%, 41.2% and 48.4% of daytime HONO formation during the CP, HP, and HHP, respectively. The significant increase of the contribution for the gas phase reaction to atmospheric HONO from the CP to the HHP was mainly ascribed to the remarkable increase of daytime NO, e.g., the NO concentration increased by a factor of ca. 7 from the CP to the HHP (Table 5.3) while the OH concentration only declined by a factor of less than 3 (Figure 5.13). Additionally, the reaction of NO + OH made a more significant contribution to HONO at noontime during the CP and in the early morning during the HP and HHP (Figure 5.11) which could be explained by the relatively high OH concentrations at noontime during the CP (Figure 5.13) and the relatively high NO in the early morning during the HP and HHP (Figure 5.5). The significant contribution from the homogeneous formation of HONO was also found at other high-$NO_x$ sites such as Beijing, Tai Wan, and Santiago de Chile[48,69,72]. Nevertheless, the formation of HONO by this gas-phase reaction does not represent a net OH source, since the same quantity of OH radicals is consumed compared to the OH formation by the subsequent HONO photolysis. Thus, for the future, additional measurements of OH radical concentrations are recommended to better quantify net OH initiation by HONO photolysis.

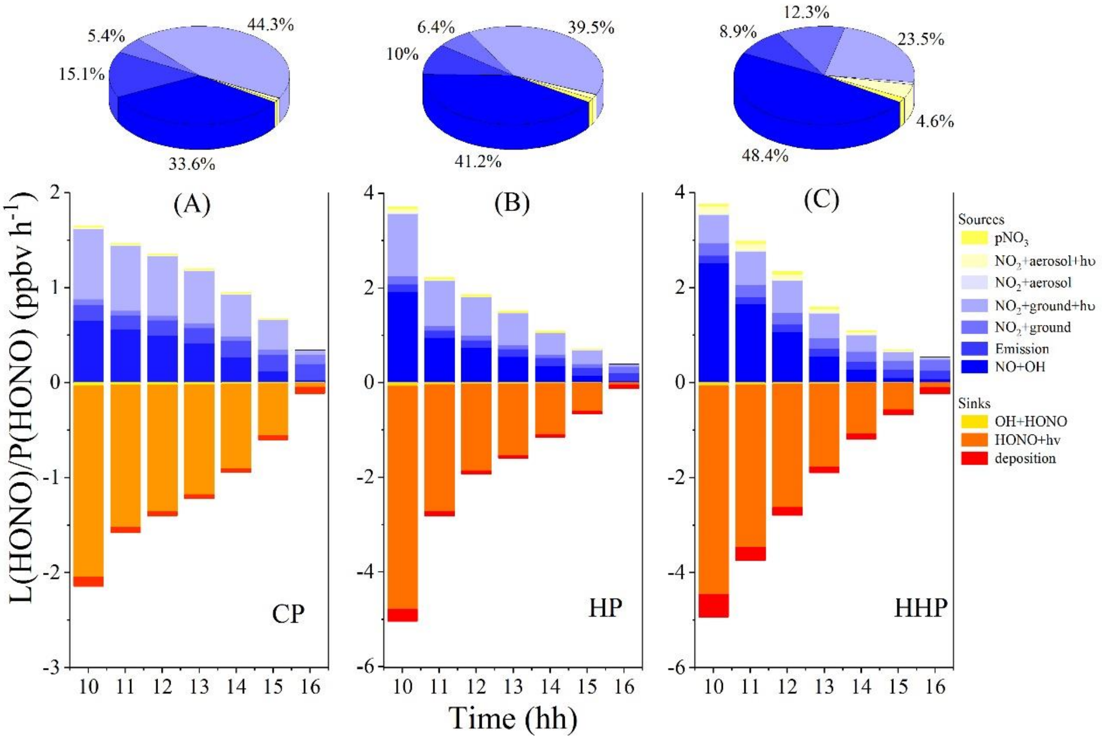

Figure 5.10 Diurnal HONO budget and the relative contribution from each source during different periods (CP: clean periods, HP: haze periods, HHP: heavy haze periods). The histograms and the pie charts contain the HONO source (positive) and sink (negative) strengths, and the corresponding relative contributions from each HONO source. The pie charts show the averaged relative contribution of each HONO source to HONO formation (10:00-17:00) during CP, HP, and HHP, respectively. Only the contribution larger than 2% is marked in the pie charts.

In contrast to the gas phase reaction of NO+OH, the contribution of the photosensitized heterogeneous reactions of $NO_2$ on ground surfaces to atmospheric HONO exhibited a declining trend from the CP to the HPP, with the contributions of 44.3%, 39.5% and 23% during the CP, HP, and HPP, respectively. The contribution of the dark heterogeneous reaction of $NO_2$ on the ground surfaces to atmospheric HONO increased with increasing $NO_2$ concentrations from the CP to the HHP, with a contribution of 5.4% in the CP, 6.4% in the HP and 12.3% in the HHP. The proportion of the direct HONO emission to the total daytime HONO formation gradually decreased from 15.1% in the CP to 10% in the HP and 8.9% in the HHP, which was mainly ascribed to the significant increase of HONO source from the gas phase reaction of NO with OH. Both the dark heterogeneous reaction and the photosensitized heterogeneous reaction of $NO_2$ on aerosol surfaces made small contributions to HONO formation, with the largest contribution of about 4.6% during HHP when both aerosol and $NO_2$ concentrations were very high, which is in agreement with previous studies[47,60]. Although the photolysis of $pNO_3$ has been proposed as one important source for atmospheric HONO, the contribution from $pNO_3$ photolysis to HONO formation was found to be negligible (<2%) even during the HHP with high $pNO_3$ concentrations. As discussed before, the photolysis of $pNO_3$ was not sensitive to EF in the range of 1 to 100 (Figure 5.8) and the modeled HONO in S-6 was much lower than the observation (Figure 5.8), suggesting that the photolysis of $pNO_3$ is not expected to play an important role in the HONO budget during wintertime at polluted regions such as the rural NCP in this study.

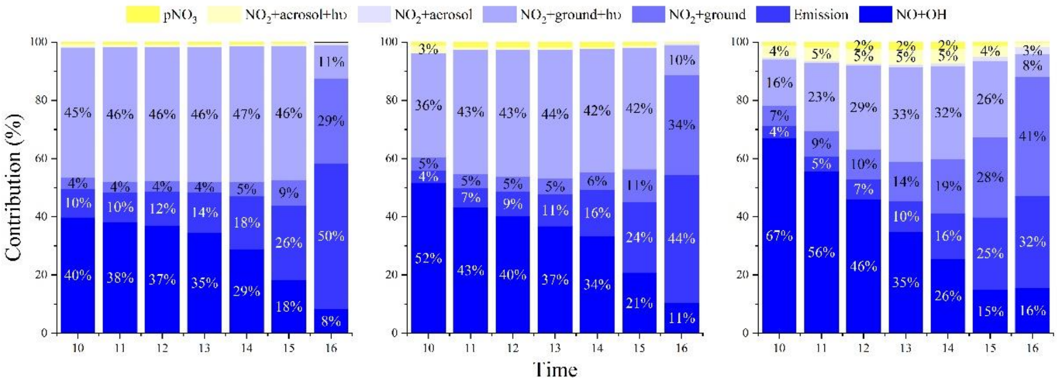

Figure 5.11 Contributions to the HONO budget from each source at different daytime hours (local time). In each histogram, the seven colors from the bottom to the top represent HONO contribution from NO+OH, emission, $NO_2$+ground, $NO_2$+ground+hν, $NO_2$+aerosol, $NO_2$+aerosol+hν, and $pNO_3$+hν, respectively. Only the contribution >2% was marked in the graph. (CP: clean periods, HP: haze periods, HHP: heavy haze periods).

The HONO loss through photolysis was the major sink, accounting for more than 90% of the HONO loss during the daytime. The reaction of HONO+OH contributed ca. 3.5% to the HONO loss during the CP, 1.5% during the HP and 1.4% during the HHP because of the relatively higher OH during the CP than the HP and HHP (Figure 5.10 and Figure 5.13). In contrast, the deposition contributed to more significant loss of HONO during the HHP (9%) than the CP (3%) and the HP (5%) because of the relatively higher HONO concentrations during HHP than CP and HP (Figure 5.5).

Based on HONO budget results, the photosensitized heterogeneous reaction of $NO_2$ on ground surfaces played the dominant role in the HONO budget, suggesting that gradient HONO measurements should be conducted in the NCP to better quantify the impact of HONO on $HO_x$ chemistry and regional air pollution such as $O_3$, SOA, and nitrate pollution. The aerosol-derived HONO sources, including heterogeneous reactions on aerosol surfaces and the photolysis of $pNO_3$ did not make a significant contribution to HONO formation even using large EF up to a factor of 100. Besides, the $pNO_3$ loss by photolysis was not expected to be a significant sink compared to the deposition on ground surfaces[190,191]. Extremely large EFs for $pNO_3$ photolysis up to a factor of 1000 should be carefully considered in model studies and more detailed, perhaps in-situ research at ambient conditions[181], especially in the high $NO_x$ and high nitrate polluted areas e.g., the NCP and other similar regions are recommended.

### 5.3.4 Implications on $HO_x$ chemistry and nitrate formation

To explore the role of HONO in radical formation, we summarized the net primary OH production from five sources in the model, i.e. HONO photolysis (subtracted by the OH loss through NO+OH and HONO+OH), $O_3$ photolysis, HCHO photolysis (here only primary emitted HCHO (37%) was considered[69]), $H_2O_2$ photolysis, ozonolysis of alkenes. The diurnal net OH production rate, P(OH), from each source and its corresponding contribution to the total daytime OH production during each pollution period are shown in Figure 5.12. It is apparent that the net OH production from HONO photolysis, $P(OH)_{HONO}$, was always more than 1 orders of magnitude larger than those from the other four sources, especially in the morning when $P(OH)_{HONO}$ was 2-3 orders of magnitude larger than others, dominating the total OH initiation. As a result, $P(OH)_{HONO}$ maintained at a high level (between $10^6$-$10^7$ molecules $cm^{-3}$ $s^{-1}$) and played the most important role in OH formation throughout the daytime. Although solar radiation decreased by a factor of about 2 during the HHP compared to the CP (Figure 5.5E), $P(OH)_{HONO}$ during the HHP was comparable to even faster than that during the CP, which was mainly ascribed to remarkable increase HONO levels during the polluted periods, e.g., the average HONO level in noontime increased by a factor of about 3 (Figure 5.5A). The mean daytime primary OH production rates were $5.6\times10^6$, $8.0\times10^6$ and $7.0\times10^6$ molecules $cm^{-3}$ $s^{-1}$ during CP, HP, and HHP, respectively, which were comparable to winter measurements in Weld Country[4], Birmingham[184], Santiago de Chile[5], and suburban Beijing[6], and also to some summer measurements at this place[7,162], Birmingham[184], and a suburban site near Paris[192], etc. The daytime OH radical concentrations (Figure 5.6), however, were much lower than those in summer measurements, suggesting much higher OH reactivity ($k_{OH}$) from the elevated levels of atmospheric pollutants including $NO_x$ (Figure 5.4 and Figure 5.5) and VOCs, leading to enhanced formation of secondary pollutants (e.g., nitrate and SOA[193], etc.).

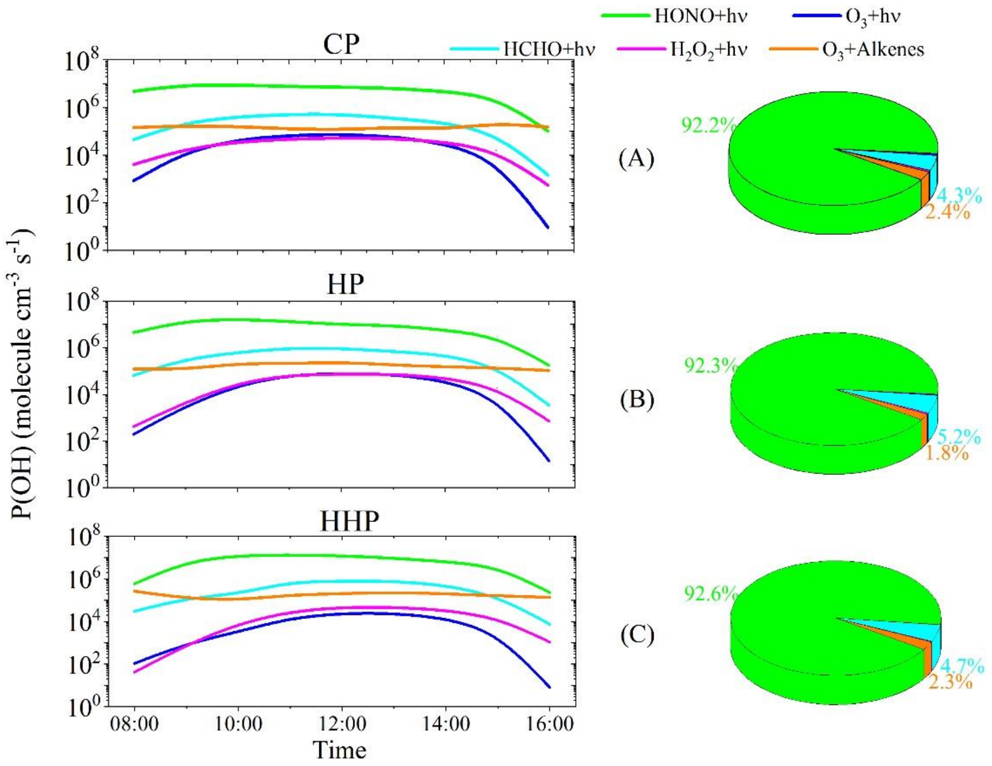

Figure 5.12 Modeled net OH production rates from five sources and their corresponding relative contribution. The colors of green, blue, cyan-blue, pink and orange represent the primary OH production from HONO photolysis, $O_3$ photolysis, HCHO photolysis, $H_2O_2$ photolysis and the ozonolysis of alkenes ($O_3$+Alkenes), respectively. Both the contributions of $O_3$ photolysis and $H_2O_2$ photolysis are less than 2% during the three periods. Note that net primary OH production from HONO was the production of OH through HONO photolysis subtracted by the OH loss through NO+OH and HONO+OH. Only direct emitted HCHO could produce primary OH and the contribution of direct HCHO emission to the observation was 37% during the campaign estimated by multiple linear regression (unpublished).

Throughout the whole campaign, the contribution to the total primary OH production from HONO photolysis was about 92% (Figure 5.12). To the best of our knowledge, the largest contribution of HONO to OH reported by previous non-polar[194] studies was 80.4% with $P(OH)_{HONO}$ of $3.1\times10^6$ molecules $cm^{-3}$ $s^{-1}$ in Weld Country, Colorado[4], both of which are, however, much lower than those in this study, suggesting a stronger oxidizing capacity and more active photochemistry in the winter at this site. The second-largest primary OH source was the photolysis of HCHO and its contribution was always between 4%-5%, which was because of the adverse trends of HCHO concentrations (low values during CP and high values during HHP) and photolysis frequency (high values during CP and low values during HHP) during the three periods.

Compared to HONO photolysis, the ozonolysis of alkenes, $O_3$ photolysis or $H_2O_2$ photolysis made a negligible contribution (less than 2%) to OH production due to their low concentrations or low photolysis frequencies.

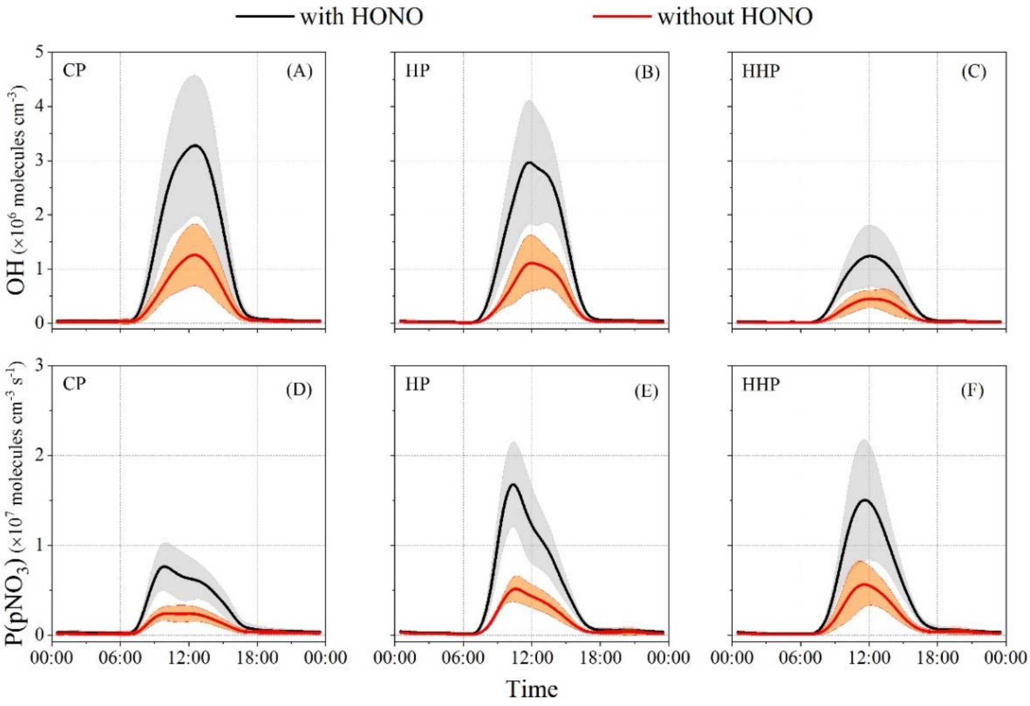

Figure 5.13 Diurnal profiles of OH concentrations and potential total nitrate formation rate from gas-phase reaction $NO_2$+OH (P($pNO_3$)) with or without constraint on HONO. The shaded areas represent the standard deviation.

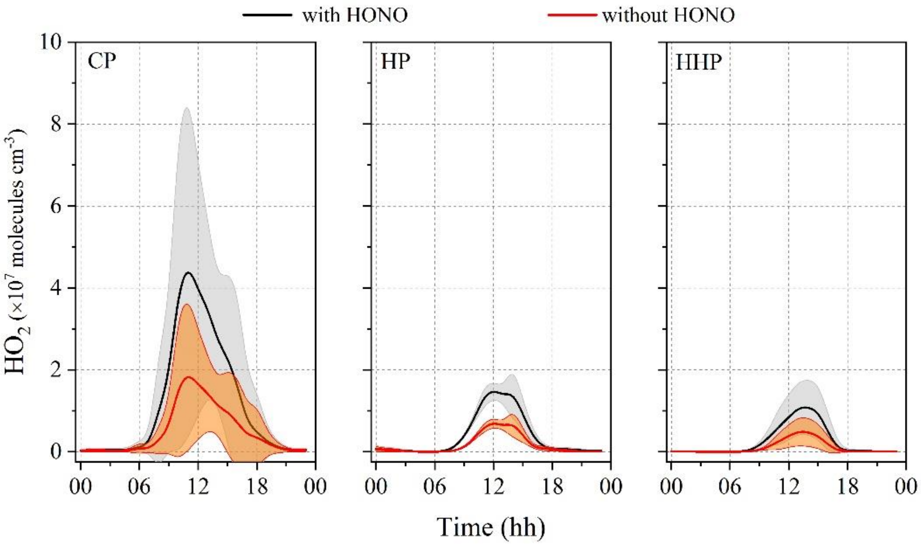

Figure 5.14 Diurnal patterns of simulated $HO_2$ in the three periods. The shadowed areas represent the standard deviation in different cases. (CP: clean periods, HP: haze periods, HHP: heavy haze periods).

High OH production rates due to fast HONO photolysis lead to high oxidizing capacity with maximum averaged OH concentrations of $3.3\times10^6$, $3.1\times10^6$ and $1.3\times10^6$ molecules $cm^{-3}$ at noontime during CP, HP, and HHP, respectively, as shown in Figure 5.13A, B and C. High OH concentrations would accelerate the homogeneous formation of nitrate precursor $HNO_3$ through the reaction $NO_2$+OH, resulting in potential daytime integrated gross nitrate production of 1.7, 3.1 and 2.9 μg $m^{-3}$ $h^{-1}$ in the three periods, respectively, as calculated in the simulations. Note that the potential daytime gross nitrate production was the upper limit of the particulate nitrate production through this path because not all the $HNO_3$(g) was transformed into particulate nitrate. Then we estimated the $HNO_3$ partitioning ratio ($HPR=pNO_3/(pNO_3+HNO_3)$)[113] using the measured nitrate and average $HNO_3$ concentration from a winter measurement[116] (Figure 5.15). High daytime HPR was found during the campaign, and HPR was higher during HHP (>0.95) than CP (>0.8), in agreement with the increasing average of NOR (nitrogen oxidation ratio: $\frac{n\,NO_3^-}{n\,NO_3^- + n\,NO_2}$) from CP (0.07) to HHP (0.2) (Figure 5.16). Meanwhile, one study used the ISORRPIA II model also found a high $HNO_3$ partitioning ratio in the NCP with an average of 0.8[113]. In our study, $NH_3$ concentration was higher, and the temperature was much lower than in Wang et al. (2018)[113] (Figure 5.1 and Figure 5.3), and therefore, the $HNO_3$ partitioning ratio was expected to be higher than 0.8[113,195]. Even scaled by 0.8, $P(pNO_3)$ is still comparable to or even more than that in the summertime at this site (ca. 2.5 μg $m^{-3}$ $h^{-1}$)[7], suggesting the significant nitrate formation from the unexpectedly active photochemistry in winter at this site. Additionally, nitrate production was able to explain the observed particulate nitrate concentrations of 2.1, 7.3, and 15.3 μg $m^{-3}$ during the three periods (Table 5.3), which provides further insight on nitrate pollution in this region. Here we did not consider $N_2O_5$ formed by $NO_3$+$NO_2$, because the modeled $N_2O_5$ concentrations and production rate were always 1-2 orders of magnitude lower than those by the reaction of $NO_2$+OH in the model.

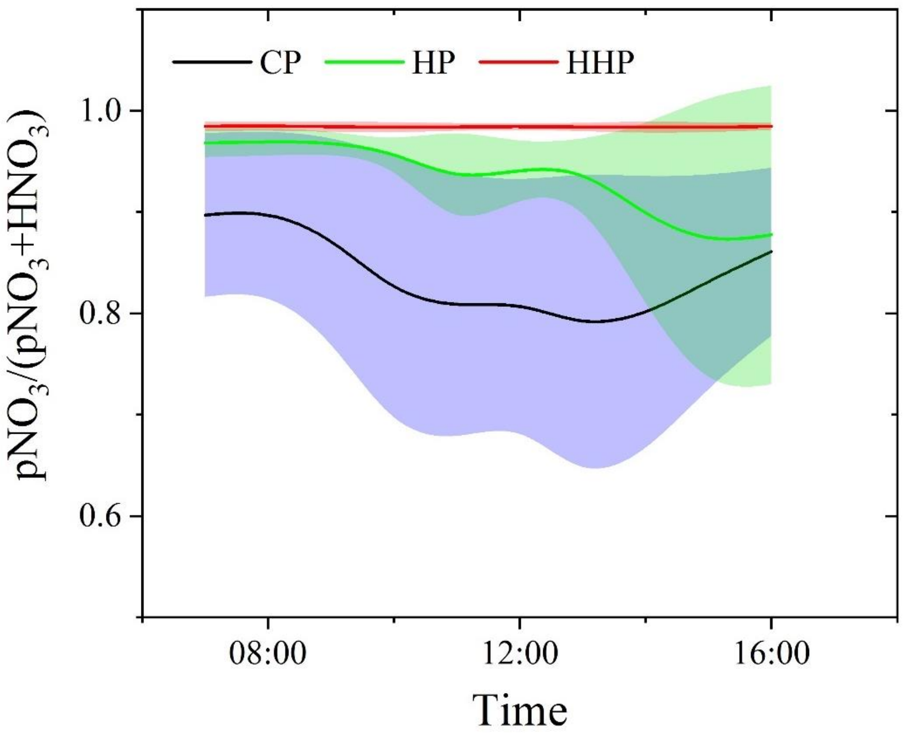

Figure 5.15 Diurnal $HNO_3$ partitioning ratio ($pNO_3/(pNO_3+HNO_3)$) in different pollution periods: CP: clean periods, HP: haze periods, and HHP: heavy haze periods. Averaged $HNO_3$ concentration of 0.08 ppbv measured by Song et al. (2018)[116] in the NCP was used here. The shadowed areas represent the standard deviation in different periods. (CP: purple, HP: green, HHP: red).

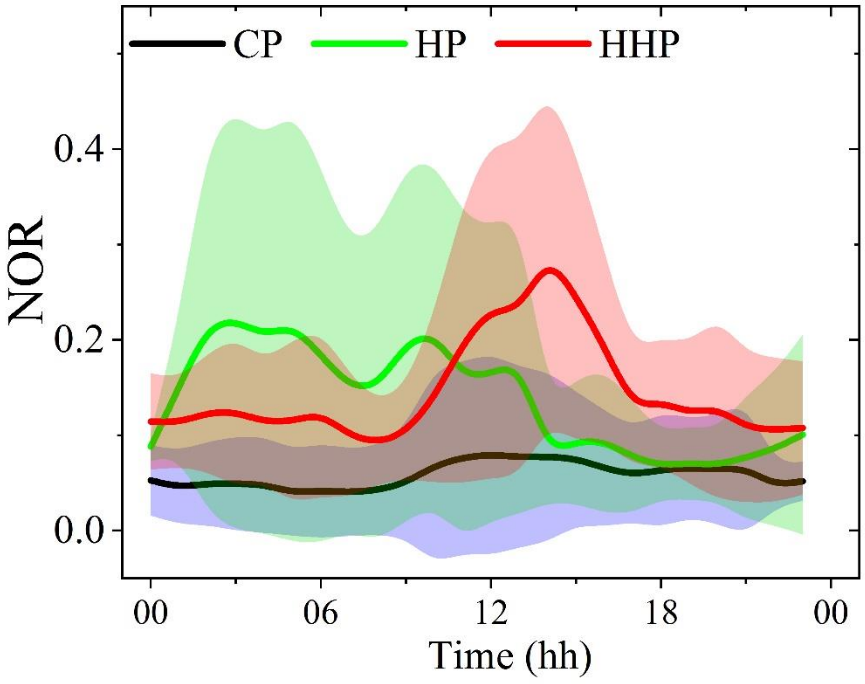

Figure 5.16 Diurnal variations of NOR in different periods : CP: clean periods, HP: haze periods, and HHP: heavy haze periods. The shadowed areas represent the standard deviation in each period (CP: purple, HP: green, HHP: red).

The dominant contribution of HONO to the OH production gave HONO an indispensable role in the atmospheric oxidizing capacity and hence the secondary pollution such as nitrate (Figure 5.13) during wintertime in the NCP. Without constraints by the measured HONO, the OH and $HO_2$ concentrations are underestimated by a factor of at least 2, which could further result in a huge underestimation of total nitrate formation rates by a factor of more than 2 (Figure 5.13 and Figure 5.14) and the formation rates of other secondary pollution, e.g., $O_3$ and SOA, reinforcing the important role of HONO in regional photochemistry and hence the formation of the regional air pollution.

Moreover, particulate nitrate pollution not only was severe but also showed an increasing trend in the NCP[195]. Take the measurement at this rural site as an example (Figure 5.17), particulate nitrate concentrations in heavy haze periods were continuously high during the whole day with an average of about 18 μg $m^{-3}$. The proportion of nitrate in the four major inorganic ions ($NO_3^-$, $SO_4^{2-}$, $Cl^-$, $NH_4^+$) of $PM_{2.5}$ was about 32% during the campaign in 2017, which was much higher than that obtained during the campaign in 2015 (27.5%).

Considering the increasing particulate nitrate pollution (Figure 5.17) and the high HONO levels (Figure 5.4) at this site and other places in the NCP[195] during wintertime, our study highlights the important role of HONO in nitrate formation and the radical budget and helps to understand the formation of HONO at different pollution levels in the NCP and other similar regions as well.

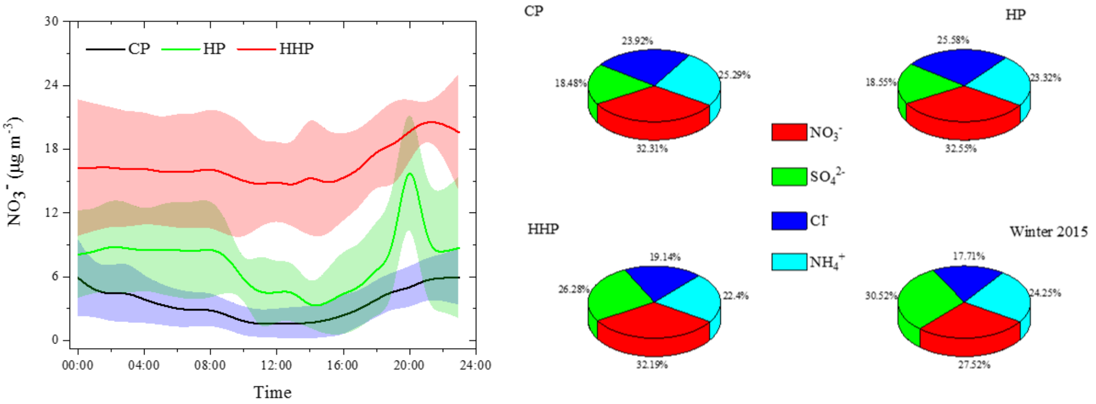

Figure 5.17 Diurnal $pNO_3$ concentration and its contribution to the inorganic composition of $PM_{2.5}$ compared to other ions during the winter campaigns in 2017 and 2015. The shadowed areas represent the standard deviation in different periods. The diurnal variations of $pNO_3$ and the three pie charts for clean periods (CP, purple), haze

periods (HP, green), heavy haze periods (HHP, red) were obtained from this campaign in the winter of 2017 and only the last pie chart was obtained from the winter campaign in 2015 at the same site[196].

## 5.4 Summary

HONO formation in the rural NCP and its impact on the formation of atmospheric OH and particulate nitrate were studied and quantified. Based on a comprehensive winter field campaign from November 2017 to January 2018 conducted at a rural site of the North China Plain, a box model (MCM v3.3.1) was used to simulate the daytime HONO budget and nitrate formation. We found that the observed daytime HONO could be well explained by the known sources in the model. The heterogeneous conversion of $NO_2$ on ground surfaces and the homogeneous reactions of NO with OH were the dominant HONO sources with contributions of more than 36% and 34% to daytime HONO, respectively. The contribution from the photolysis of particulate nitrate and the reactions of $NO_2$ on aerosol surfaces was negligible in clean periods (2%) and slightly higher in polluted periods (8%). Besides, the gradual decrease of $NO_2$ uptake coefficient on ground surfaces with pollution levels could better explain the observed HONO under different pollution levels.

The photolysis of HONO acted as the dominant source for primary OH with a contribution of more than 92%, much higher than other OH sources such as the photolysis of $O_3$, $H_2O_2$, HCHO, etc. The relatively high OH levels due to fast HONO photolysis at the rural site remarkably accelerated gas-phase reactions, resulting in the rapid formation of nitrate as well as other secondary pollutants in the daytime. For example, $HO_x$ ($OH+HO_2$) mixing ratios and potential nitrate formation were 1-8 times and 1-2 times underestimated by the model if HONO was not constrained by the observation, implying the critical role of HONO in atmospheric oxidizing capacity and nitrate formation in the wintertime of this region.

# Chapter 6 Conclusions and perspectives

Air pollution is still an environmental problem that urgently needs to be solved in the North China Plain (NCP). With the aim to explore HONO formation and its impact on regional air quality in the NCP, the present study described the development of instruments to measure atmospheric HONO and soil HONO emission flux. Based on field measurement on atmospheric HONO and soil HONO emission flux, a chemistry transport model (The Community Multiscale Air Quality Modeling System, CMAQ) and a box model (Master Chemical Mechanism, MCM) were used to explore the HONO budget and its impact on regional air pollution, e.g., summer $O_3$ pollution and winter haze pollution. We found that HONO plays an important role in atmospheric oxidizing capacity and deteriorating regional air quality.

**Main conclusions** are as follows:

1. An SC-IC method using ultrapure water as the absorption solution was developed to measure atmospheric HONO. The detection limit and time resolution could reach 4 pptv and in 2.5 min. Chamber studies proved that wet chemical methods, especially those using alkaline absorption solutions, might suffer from small interference from the co-existence of $SO_2$ and $NO_2$. HONO might be overestimated in low $SO_2$ conditions and underestimated in high $SO_2$ conditions with the existence of $NO_2$. Our study showed that the SC-IC method using ultrapure water as the absorption solution was able to collect atmospheric HONO and avoid interference from the co-existence of $SO_2$ and $NO_2$ in typical pollution areas. Statistical analysis of the field comparisons of SC-IC with CEAS or two LOPAPs also confirms the reliability of SC-IC to be applied in the field measurements.

2. A twin open-top dynamic chambers (OTC) system was developed to accurately quantify HONO emission fluxes from agricultural soil in the NCP. Laboratory research and field measurement confirmed the excellent performance of the OTCs system to measure soil HONO emission fluxes. The interference from the wall effect, the greenhouse effect, and photolysis were rationally discussed. We found that the HONO emission flux (up to 3.21 ng N $m^{-2}$ $s^{-1}$) before fertilization could account for about 200 pptv $h^{-1}$ of the missing HONO source under an assumed mixing layer height of 100 m. The emission fluxes from agricultural soil in the NCP were largely enhanced by ammonium fertilization, which was possibly attributed to biological processes,

including nitrification. Soil HONO emission was significantly affected by the fertilization rate. Our present results highlight the critical need to measure HONO emission fluxes from agricultural soil in the NCP and other similar.

3. HONO emission fluxes from typical agricultural soil in the NCP were obtained by the OTC system and the impact on regional air quality was quantified by a chemistry transport model (CMAQ). The observations showed that the HONO emission flux rapidly increased after fertilization on the agricultural soil, and significant HONO emission was continuously observed in 15 days after fertilization. Besides, the observed emission flux exhibited an evident diurnal variation with a peak at noontime and a minimum at nighttime. The largest HONO emission reached 350 ng N $m^{-2}$ $s^{-1}$ after fertilization, which was 1-2 orders of magnitude higher than the reported values from limited studies. Meanwhile, a remarkable increase of atmospheric HONO mixing ratio with a noontime peak was found after fertilization, which confirmed strong soil HONO emissions again. According to the relationship of HONO emission fluxes and the observed soil temperature and relative humidity (RH), the averaged diurnal variation of HONO emission flux was well reproduced by an Arrhenius equation. The parameterization was then adopted to the CMAQ model to explore the impact of soil HONO emission on regional air quality. Model results showed that daytime averaged levels of $O_3$ and OH in the NCP increased by about 8 ppbv and $5\times10^6$ molecules $cm^{-3}$, respectively, indicating the significant impact of the intensive fertilization on regional air pollution and atmospheric oxidizing capacity in the summertime of the NCP. More similar studies need to be conducted in this region or similar regions.

4. A new mechanism for soil HONO emission was proposed. Based on flow tube techniques, laboratory experiments were conducted to measure HONO and NO emissions from a) original soil samples with ammonium fertilizers, b) sterilized soil samples with nitrate fertilizers, c) sterilized soil samples with ammonium fertilizers, and d) original soil samples with ammonium fertilizers and nitrification inhibitors. We found that only the original soil samples with ammonium fertilizers could significantly emit HONO and NO, indicating that the HONO emission was mainly from the nitrification process. During the nitrification process, $NH_4^+$ was converted to $NO_3^-$ by the nitrifying bacteria with intermediate products of $NO_2^-$ and $H^+$. The combination of $NO_2^-$ and $H^+$ increased the concentration of HONO in the soil solution environment, which promoted the release of HONO to the atmosphere. Additionally, HONO emissions increased with soil temperature in the range of 18-35 °C but decreased with

the relative humidity of the flushing gas, which could well explain the observed diurnal variation of soil HONO emissions. On the one hand, the increase in soil temperature could accelerate nitrification activities; on the other hand, it reduced the solubility of HONO in soil solution and accelerate water evaporation from soil surfaces, which promoted the release of HONO from the soil. Similarly, high relative humidity of the flushing gas suppressed water evaporation from soil surfaces, leading to low HONO emissions from the soil.

5. HONO formation in the rural NCP and its impact on the formation of atmospheric OH and particulate nitrate were quantified. Based on a comprehensive winter field campaign from November 2017 to January 2018 conducted at a rural site of the North China Plain, a box model (MCM v3.3.1) was used to simulate the daytime HONO budget and nitrate formation. We found that the observed daytime HONO could be well explained by the known sources in the model. The heterogeneous conversion of $NO_2$ on ground surfaces and the homogeneous reactions of NO with OH were the dominant HONO sources with contributions of more than 36% and 34% to daytime HONO, respectively. The contributions from the photolysis of particulate nitrate and the reactions of $NO_2$ on aerosol surfaces were negligible in clean periods (2%) and slightly higher in polluted periods (8%). Besides, the gradual decrease of $NO_2$ uptake coefficient on ground surfaces with pollution levels could better explain the observed HONO under different pollution levels.

The photolysis of HONO acted as the dominant source for primary OH with a contribution of more than 92%, much higher than other OH sources such as the photolysis of $O_3$, $H_2O_2$, HCHO, etc. The relatively high OH levels due to fast HONO photolysis at the rural site remarkably accelerated gas-phase reactions, resulting in the rapid formation of nitrate as well as other secondary pollutants in the daytime. For example, $HO_x$ ($OH+HO_2$) mixing ratios and potential nitrate formation rate were 1-8 timed and 1-2 times underestimated by the model, respectively, if HONO was not constrained by the observation, implying the critical role of HONO in atmospheric oxidizing capacity and nitrate formation in the wintertime of this region.

**Main perspectives** are as follows:

1. Different types of soil in other regions of China and other countries in the world may have different HONO emission characteristics with different emission mechanisms. For example, agricultural soil in the NCP was mainly alkaline, while in south China might be acidic. Soil HONO emissions in south China was expected to be different from the

NCP. More field campaigns and laboratory research are still needed in further studies to better understand soil HONO emissions and the regional impact.

2. DCD was found to efficiently reduce soil HONO and NO emissions, which could significantly improve regional air quality, as discussed in Chapter 4. However, DCD may accelerate $NH_3$ emissions, which was expected to be one of the reasons for regional air pollution in the NCP. In my opinion, more systematic experiments are needed to be conducted to better assess the impact of DCD on regional air quality.

3. Ground-based HONO sources were mostly proved to be an important HONO source. Therefore, gradient HONO distribution was expected, which means the observations on the ground level might mislead the understanding of HONO budget as well as its impact. By far, few gradient HONO measurement was conducted in China. It may be an important research topic in the future.

4. In our opinion, comprehensive field campaigns are urgently needed in China to better understand air pollution. Take HONO as an example, different studies had different conclusions and some of them were caused by the lack of measurements on important related parameters like radicals, boundary layer height, mixing layer height, etc. The estimation of related parameters may cause a discrepancy between different studies. Hence, comprehensive field campaigns with measurements on various parameters are still needed to be conducted in the future.

## References

(1) Seinfeld, J. H. S. N. P. *Atmospheric Chemistry and Physics: From Air Pollution to Climate Change*; John Wiley & Sons, 2016.

(2) Lu, K.; Guo, S.; Tan, Z.; Wang, H.; Shang, D.; Liu, Y.; Li, X.; Wu, Z.; Hu, M.; Zhang, Y. Exploring the Atmospheric Free Radical Chemistry in China: The Self-Cleansing Capacity and the Formation of Secondary Air Pollution. *Natl. Sci. Rev.* **2018**, nwy073–nwy073. https://doi.org/10.1093/nsr/nwy073.

(3) Alicke, B.; Geyer, A.; Hofzumahaus, A.; Holland, F.; Konrad, S.; Pätz, H. W.; Schäfer, J.; Stutz, J.; Volz-Thomas, A.; Platt, U. OH Formation by HONO Photolysis during the BERLIOZ Experiment. *J. Geophys. Res. D Atmos.* **2003**, *108* (4), 3–1. https://doi.org/10.1029/2001jd000579.

(4) Kim, S.; Vandenboer, T. C.; Young, C. J.; Riedel, T. P.; Thornton, J. A.; Swarthout, B.; Sive, B.; Lerner, B.; Gilman, J.; Warneke, C.; et al. The Primary and Recycling Sources of OH during the NACHTT-2011 Campaign: HONO as an Important OH Primary Source in the Wintertime. *J. Geophys. Res.* **2014**, *119* (11), 6886–6896. https://doi.org/10.1002/2013JD019784.

(5) Elshorbany, Y. F.; Kleffmann, J.; Kurtenbach, R.; Lissi, E.; Rubio, M.; Villena, G.; Gramsch, E.; Rickard, A. R.; Pilling, M. J.; Wiesen, P. Seasonal Dependence of the Oxidation Capacity of the City of Santiago de Chile. *Atmos. Environ.* **2010**, *44* (40), 5383–5394. https://doi.org/10.1016/j.atmosenv.2009.08.036.

(6) Tan, Z.; Rohrer, F.; Lu, K.; Ma, X.; Bohn, B.; Broch, S.; Dong, H.; Fuchs, H.; Gkatzelis, G. I.; Hofzumahaus, A.; et al. Wintertime Photochemistry in Beijing: Observations of $RO_x$ Radical Concentrations in the North China Plain during the BEST-ONE Campaign. *Atmos. Chem. Phys.* **2018**, *18* (16), 12391–12411. https://doi.org/10.5194/acp-18-12391-2018.

(7) Tan, Z.; Fuchs, H.; Lu, K.; Hofzumahaus, A.; Bohn, B.; Broch, S.; Dong, H.; Gomm, S.; Häseler, R.; He, L.; et al. Radical Chemistry at a Rural Site (Wangdu) in the North China Plain: Observation and Model Calculations of OH, $HO_2$ and RO2 Radicals. *Atmos. Chem. Phys.* **2017**, *17* (1), 663–690. https://doi.org/10.5194/acp-17-663-2017.

(8) Li, D.; Xue, L.; Wen, L.; Wang, X.; Chen, T.; Mellouki, A.; Chen, J.; Wang, W. Characteristics and Sources of Nitrous Acid in an Urban Atmosphere of

Northern China: Results from 1-Yr Continuous Observations. *Atmos. Environ.* **2018**, *182*, 296–306. https://doi.org/10.1016/j.atmosenv.2018.03.033.

(9) Zhang, W.; Tong, S.; Ge, M.; An, J.; Shi, Z.; Hou, S.; Xia, K.; Qu, Y.; Zhang, H.; Chu, B.; et al. Variations and Sources of Nitrous Acid (HONO) during a Severe Pollution Episode in Beijing in Winter 2016. *Sci. Total Environ.* **2019**, *648*, 253–262. https://doi.org/10.1016/j.scitotenv.2018.08.133.

(10) Finlayson-Pitts, B. J. Tropospheric Air Pollution: Ozone, Airborne Toxics, Polycyclic Aromatic Hydrocarbons, and Particles. *Science.* **2002**, *276* (5315), 1045–1051. https://doi.org/10.1126/science.276.5315.1045.

(11) Stone, D.; Whalley, L. K.; Heard, D. E. Tropospheric OH and $HO_2$ Radicals: Field Measurements and Model Comparisons. *Chem. Soc. Rev.* **2012**, *41* (19), 6348–6404. https://doi.org/10.1039/c2cs35140d.

(12) Crosley, D. R. The Measurement of OH and $HO_2$ in the Atmosphere. *J. Atmos. Sci.* **1995**, *52* (19), 3299–3314. https://doi.org/10.1175/1520-0469(1995)052<3299:TMOOAH>2.0.CO;2.

(13) Burkholder, J. B.; Abbatt, J. P. D.; Barnes, I.; Roberts, J. M.; Melamed, M. L.; Ammann, M.; Bertram, A. K.; Cappa, C. D.; Carlton, A. G.; Carpenter, L. J.; et al. The Essential Role for Laboratory Studies in Atmospheric Chemistry. *Environ. Sci. Technol.* **2017**, *51* (5), 2519–2528. https://doi.org/10.1021/acs.est.6b04947.

(14) Stone, D.; Whalley, L. K.; Heard, D. E. Tropospheric OH and HO2 Radicals: Field Measurements and Model Comparisons. *Chem. Soc. Rev.* **2012**, *41* (19), 6348–6404. https://doi.org/10.1039/c2cs35140d.

(15) Friedfeld, S.; Fraser, M.; Ensor, K.; Tribble, S.; Rehle, D.; Leleux, D.; Tittel, F. Statistical Analysis of Primary and Secondary Atmospheric Formaldehyde. *Atmos. Environ.* **2002**, *36* (30), 4767–4775. https://doi.org/10.1016/S1352-2310(02)00558-7.

(16) Elshorbany, Y. F.; Kurtenbach, R.; Wiesen, P.; Lissi, E.; Rubio, M.; Villena, G.; Gramsch, E.; Rickard, A. R.; Pilling, M. J.; Kleffmann, J. Oxidation Capacity of the City Air of Santiago, Chile. *Atmos. Chem. Phys.* **2009**, *9* (6), 2257–2273. https://doi.org/10.5194/acp-9-2257-2009.

(17) Criegee, R. Mechanism of Ozonolysis. *Angew. Chemie Int. Ed. English* **1975**. https://doi.org/10.1002/anie.197507451.

(18) Paulson, S. E.; Chung, M. Y.; Hasson, A. S. OH Radical Formation from the

Gas-Phase Reaction of Ozone with Terminal Alkenes and the Relationship between Structure and Mechanism. *J. Phys. Chem. A* **1999**, *103* (41), 8125–8138. https://doi.org/10.1021/jp991995e.

(19) Platt, U.; Perner, D.; Harris, G. W.; Winer, A. M.; Pitts, J. N. Observations of Nitrous Acid in an Urban Atmosphere by Differential Optical Absorption. *Nature* **1980**, *285* (5763), 312–314. https://doi.org/10.1038/285312a0.

(20) Acker, K.; Möller, D.; Wieprecht, W.; Meixner, F. X.; Bohn, B.; Gilge, S.; Plass-Dülmer, C.; Berresheim, H. Strong Daytime Production of OH from $HNO_2$ at a Rural Mountain Site. *Geophys. Res. Lett.* **2006**, *33* (2). https://doi.org/10.1029/2005GL024643.

(21) Kanaya, Y.; Cao, R.; Akimoto, H.; Fukuda, M.; Komazaki, Y.; Yokouchi, Y.; Koike, M.; Tanimoto, H.; Takegawa, N.; Kondo, Y. Urban Photochemistry in Central Tokyo: 1. Observed and Modeled OH and $HO_2$ Radical Concentrations during the Winter and Summer of 2004. *J. Geophys. Res. Atmos.* **2007**, *112* (21). https://doi.org/10.1029/2007JD008670.

(22) Kleffmann, J.; Gavriloaiei, T.; Hofzumahaus, A.; Holland, F.; Koppmann, R.; Rupp, L.; Schlosser, E.; Siese, M.; Wahner, A. Daytime Formation of Nitrous Acid: A Major Source of OH Radicals in a Forest. *Geophys. Res. Lett.* **2005**, *32* (5). https://doi.org/ArtnL0581810.1029/2005gl022524.

(23) Kleffmann, J.; Kurtenbach, R.; Lörzer, J.; Wiesen, P.; Kalthoff, N.; Vogel, B.; Vogel, H. Measured and Simulated Vertical Profiles of Nitrous Acid - Part I: Field Measurements. *Atmos. Environ.* **2003**, *37* (21), 2949–2955. https://doi.org/10.1016/S1352-2310(03)00242-5.

(24) Tan, Z.; Fuchs, H.; Lu, K.; Hofzumahaus, A.; Bohn, B.; Broch, S.; Dong, H.; Gomm, S.; Häseler, R.; He, L.; et al. Radical Chemistry at a Rural Site (Wangdu) in the North China Plain: Observation and Model Calculations of OH, $HO_2$ and $RO_2$ Radicals. *Atmos. Chem. Phys.* **2017**, *17* (1), 663–690. https://doi.org/10.5194/acp-17-663-2017.

(25) Su, H.; Cheng, Y. F.; Shao, M.; Gao, D. F.; Yu, Z. Y.; Zeng, L. M.; Slanina, J.; Zhang, Y. H.; Wiedensohler, A. Nitrous Acid (HONO) and Its Daytime Sources at a Rural Site during the 2004 PRIDE-PRD Experiment in China. *J. Geophys. Res.* **2008**, *113* (D14), D14. https://doi.org/ArtnD1431210.1029/2007jd009060.

(26) Qin, M.; Xie, P.; Su, H.; Gu, J.; Peng, F.; Li, S.; Zeng, L.; Liu, J.; Liu, W.; Zhang, Y. An Observational Study of the HONO-$NO_2$ Coupling at an Urban Site in

Guangzhou City, South China. *Atmos. Environ.* **2009**, *43* (36), 5731–5742. https://doi.org/10.1016/j.atmosenv.2009.08.017.

(27) Li, X.; Brauers, T.; Häseler, R.; Bohn, B.; Fuchs, H.; Hofzumahaus, A.; Holland, F.; Lou, S.; Lu, K. D.; Rohrer, F.; et al. Exploring the Atmospheric Chemistry of Nitrous Acid (HONO) at a Rural Site in Southern China. *Atmos. Chem. Phys.* **2012**, *12* (3), 1497–1513. https://doi.org/10.5194/acp-12-1497-2012.

(28) Hou, S.; Tong, S.; Ge, M.; An, J. Comparison of Atmospheric Nitrous Acid during Severe Haze and Clean Periods in Beijing, China. *Atmos. Environ.* **2016**, *124*, 199–206. https://doi.org/10.1016/j.atmosenv.2015.06.023.

(29) Ryan, R. G.; Rhodes, S.; Tully, M.; Wilson, S.; Jones, N.; Frieß, U.; Schofield, R. Daytime HONO, $NO_2$ and Aerosol Distributions from MAX-DOAS Observations in Melbourne. *Atmos. Chem. Phys. Discuss.* **2018**, No. 2, 1–27. https://doi.org/10.5194/acp-2018-409.

(30) Kurtenbach, R.; Becker, K. H.; Gomes, J. A. G.; Kleffmann, J.; Lörzer, J. C.; Spittler, M.; Wiesen, P.; Ackermann, R.; Geyer, A.; Platt, U. Investigations of Emissions and Heterogeneous Formation of HONO in a Road Traffic Tunnel. *Atmos. Environ.* **2001**, *35* (20), 3385–3394. https://doi.org/10.1016/S1352-2310(01)00138-8.

(31) Liu, Y.; Lu, K.; Ma, Y.; Yang, X.; Zhang, W.; Wu, Y.; Peng, J.; Shuai, S.; Hu, M.; Zhang, Y. Direct Emission of Nitrous Acid (HONO) from Gasoline Cars in China Determined by Vehicle Chassis Dynamometer Experiments. *Atmos. Environ.* **2017**, *169*, 89–96. https://doi.org/10.1016/j.atmosenv.2017.07.019.

(32) Trinh, H. T.; Imanishi, K.; Morikawa, T.; Hagino, H.; Takenaka, N. Gaseous Nitrous Acid (HONO) and Nitrogen Oxides ($NO_x$) Emission from Gasoline and Diesel Vehicles under Real-World Driving Test Cycles. *J. Air Waste Manag. Assoc.* **2017**, *67* (4), 412–420. https://doi.org/10.1080/10962247.2016.1240726.

(33) Finlayson-Pitts, B. J.; Wingen, L. M.; Sumner, A. L.; Syomin, D.; Ramazan, K. A. The Heterogeneous Hydrolysis of $NO_2$ in Laboratory Systems and in Outdoor and Indoor Atmospheres: An Integrated Mechanism. *Phys. Chem. Chem. Phys.* **2003**, *5* (2), 223–242. https://doi.org/10.1039/b208564j.

(34) Kleffmann, J.; Becker, K. H.; Wiesen, P. Heterogeneous $NO_2$ Conversion Processes on Acid Surfaces: Possible Atmospheric Implications. *Atmos. Environ.* **1998**, *32* (16), 2721–2729. https://doi.org/10.1016/S1352-2310(98)00065-X.

(35) Monge, M. E.; D’Anna, B.; Mazri, L.; Giroir-Fendler, A.; Ammann, M.;

Donaldson, D. J.; George, C. Light Changes the Atmospheric Reactivity of Soot. *Proc. Natl. Acad. Sci.* **2010**, *107* (15), 6605–6609. https://doi.org/10.1073/pnas.0908341107.

(36) Ammann, M.; Kalberer, M.; Jost, D. T.; Tobler, L.; Rössler, E.; Piguet, D.; Gäggeler, H. W.; Baltensperger, U. Heterogeneous Production of Nitrous Acid on Soot in Polluted Air Masses. *Nature* **1998**, *395* (6698), 157–160. https://doi.org/10.1038/25965.

(37) George, C.; Strekowski, R. S.; Kleffmann, J.; Stemmler, K.; Ammann, M. Photoenhanced Uptake of Gaseous $NO_2$ on Solid Organic Compounds: A Photochemical Source of HONO? *Faraday Discuss.* **2005**, *130*, 195–210. https://doi.org/10.1039/b417888m.

(38) Stemmler, K.; Ammann, M.; Donders, C.; Kleffmann, J.; George, C. Photosensitized Reduction of Nitrogen Dioxide on Humic Acid as a Source of Nitrous Acid. *Nature* **2006**, *440* (7081), 195–198. https://doi.org/10.1038/nature04603.

(39) Han, C.; Yang, W.; Yang, H.; Xue, X. Enhanced Photochemical Conversion of $NO_2$ to HONO on Humic Acids in the Presence of Benzophenone. *Environ. Pollut.* **2017**, *231* (2), 979–986. https://doi.org/10.1016/j.envpol.2017.08.107.

(40) Han, C.; Yang, W.; Wu, Q.; Yang, H.; Xue, X. Heterogeneous Photochemical Conversion of $NO_2$ to HONO on the Humic Acid Surface under Simulated Sunlight. *Environ. Sci. Technol.* **2016**, *50* (10), 5017–5023. https://doi.org/10.1021/acs.est.5b05101.

(41) Ma, Q.; Wang, T.; Liu, C.; He, H.; Wang, Z.; Wang, W.; Liang, Y. $SO_2$ Initiates the Efficient Conversion of $NO_2$ to HONO on MgO Surface. *Environ. Sci. Technol.* **2017**. https://doi.org/10.1021/acs.est.6b05724.

(42) Liu, J.; Li, S.; Mekic, M.; Jiang, H.; Zhou, W.; Loisel, G.; Song, W.; Wang, X.; Gligorovski, S. Photoenhanced Uptake of $NO_2$ and HONO Formation on Real Urban Grime . *Environ. Sci. Technol. Lett.* **2019**, *6* (2), 413–417. https://doi.org/10.1021/acs.estlett.9b00308.

(43) Aumont, B.; Chervier, F.; Laval, S. Contribution of HONO Sources to the $NO_x/HO_x/O_3$ Chemistry in the Polluted Boundary Layer. *Atmos. Environ.* **2003**, *37* (4), 487–498. https://doi.org/10.1016/S1352-2310(02)00920-2.

(44) Vogel, B.; Vogel, H.; Kleffmann, J.; Kurtenbach, R. Measured and Simulated Vertical Profiles of Nitrous Acid - Part II. Model Simulations and Indications for

a Photolytic Source. *Atmos. Environ.* **2003**, *37* (21), 2957–2966. https://doi.org/10.1016/S1352-2310(03)00243-7.

(45) Wong, K. W.; Lefer, B. L.; Rappenglück, B.; Stutz, J. Vertical Profiles of Nitrous Acid in the Nocturnal Urban Atmosphere of Houston, TX. *Atmos. Chem. Phys.* **2011**, *11* (8), 3595–3609. https://doi.org/10.5194/acp-11-3595-2011.

(46) Spataro, F.; Ianniello, A.; Esposito, G.; Allegrini, I.; Zhu, T.; Hu, M. Occurrence of Atmospheric Nitrous Acid in the Urban Area of Beijing (China). *Sci. Total Environ.* **2013**, *447*, 210–224. https://doi.org/10.1016/j.scitotenv.2012.12.065.

(47) Zhang, L.; Wang, T.; Zhang, Q.; Zheng, J.; Xu, Z.; Lv, M. Potential Sources of Nitrous Acid (HONO) and Their Impacts on Ozone: A WRF-Chem Study in a Polluted Subtropical Region. *J. Geophys. Res.* **2016**, *121* (7), 3645–3662. https://doi.org/10.1002/2015JD024468.

(48) Harrison, R. M.; Kitto, A.-M. N. Evidence for a Surface Source of Atmospheric Nitrous Acid. *Atmos. Environ.* **1994**, *28* (6), 1089–1094. https://doi.org/10.1016/1352-2310(94)90286-0.

(49) Honrath, R. E.; Lu, Y.; Peterson, M. C.; Dibb, J. E.; Arsenault, M. A.; Cullen, N. J.; Steffen, K. Vertical Fluxes of $NO_x$, HONO, and $HNO_3$ above the Snowpack at Summit, Greenland. *Atmos. Environ.* **2002**, *36* (15–16), 2629–2640. https://doi.org/10.1016/S1352-2310(02)00132-2.

(50) Laufs, S.; Cazaunau, M.; Stella, P.; Kurtenbach, R.; Cellier, P.; Mellouki, A.; Loubet, B.; Kleffmann, J. Diurnal Fluxes of HONO above a Crop Rotation. *Atmos. Chem. Phys.* **2017**, *17* (11), 1–28. https://doi.org/10.5194/acp-17-6907-2017.

(51) Laufs, S.; Kleffmann, J. Investigations on HONO Formation from Photolysis of Adsorbed $HNO_3$ on Quartz Glass Surfaces. *Phys. Chem. Chem. Phys.* **2016**, *18* (14), 9616–9625. https://doi.org/10.1039/c6cp00436a.

(52) Zhou, X. L.; Gao, H. L.; He, Y.; Huang, G.; Bertman, S. B.; Civerolo, K.; Schwab, J. Nitric Acid Photolysis on Surfaces in Low-NOx Environments: Significant Atmospheric Implications. *Geophys. Res. Lett.* **2003**, *30* (23). https://doi.org/Artn221710.1029/2003gl018620.

(53) Zhou, X.; Zhang, N.; Teravest, M.; Tang, D.; Hou, J.; Bertman, S.; Alaghmand, M.; Shepson, P. B.; Carroll, M. A.; Griffith, S.; et al. Nitric Acid Photolysis on Forest Canopy Surface as a Source for Tropospheric Nitrous Acid. *Nat. Geosci.* **2011**, *4* (7), 440–443. https://doi.org/10.1038/ngeo1164.

(54) Ye, C.; Zhou, X.; Pu, D.; Stutz, J.; Festa, J.; Spolaor, M.; Tsai, C.; Cantrell, C.; Mauldin, R. L.; Campos, T.; et al. Rapid Cycling of Reactive Nitrogen in the Marine Boundary Layer. *Nature* **2016**, *532* (7600), 489–491. https://doi.org/10.1038/nature17195.

(55) Bao, F.; Li, M.; Zhang, Y.; Chen, C.; Zhao, J. Photochemical Aging of Beijing Urban PM2.5: HONO Production. *Environ. Sci. Technol.* **2018**, *52* (11), 6309–6316. https://doi.org/10.1021/acs.est.8b00538.

(56) Ye, C.; Zhang, N.; Gao, H.; Zhou, X. Photolysis of Particulate Nitrate as a Source of HONO and $NO_x$. *Environ. Sci. Technol.* **2017**, *51* (12), 6849–6856. https://doi.org/10.1021/acs.est.7b00387.

(57) Yang, W.; Han, C.; Yang, H.; Xue, X. Significant HONO Formation by the Photolysis of Nitrates in the Presence of Humic Acids. *Environ. Pollut.* **2018**. https://doi.org/https://doi.org/10.1016/j.envpol.2018.09.039.

(58) Romer, P.; Wooldridge, P. J.; Crounse, J. D.; Kim, M. J.; Wennberg, P. O.; Dibb, J.; Scheuer, E.; Blake, D. R.; Meinardi, S.; Brosius, A. L.; et al. Constraints on Aerosol Nitrate Photolysis as a Potential Source of HONO and NO. **2018**, No. x. https://doi.org/10.1021/acs.est.8b03861.

(59) Vandenboer, T. C.; Young, C. J.; Talukdar, R. K.; Markovic, M. Z.; Brown, S. S.; Roberts, J. M.; Murphy, J. G. Nocturnal Loss and Daytime Source of Nitrous Acid through Reactive Uptake and Displacement. *Nat. Geosci.* **2015**, *8* (1), 55–60. https://doi.org/10.1038/ngeo2298.

(60) Liu, Y.; Lu, K.; Li, X.; Dong, H.; Tan, Z.; Wang, H.; Zou, Q.; Wu, Y.; Zeng, L.; Hu, M.; et al. A Comprehensive Model Test of the HONO Sources Constrained to Field Measurements at Rural North China Plain. *Environ. Sci. Technol.* **2019**, *53* (7), 3517–3525. https://doi.org/10.1021/acs.est.8b06367.

(61) Wong, K. W.; Tsai, C.; Lefer, B.; Grossberg, N.; Stutz, J. Modeling of Daytime HONO Vertical Gradients during SHARP 2009. *Atmos. Chem. Phys.* **2013**, *13* (7), 3587–3601. https://doi.org/10.5194/acp-13-3587-2013.

(62) Meusel, H.; Kuhn, U.; Reiffs, A.; Mallik, C.; Harder, H.; Martinez, M.; Schuladen, J.; Bohn, B.; Parchatka, U.; Crowley, J. N.; et al. Daytime Formation of Nitrous Acid at a Coastal Remote Site in Cyprus Indicating a Common Ground Source of Atmospheric HONO and NO. *Atmos. Chem. Phys.* **2016**, *16* (22), 14475–14493. https://doi.org/10.5194/acp-16-14475-2016.

(63) Twigg, M. M.; House, E.; Thomas, R.; Whitehead, J.; Phillips, G. J.; Famulari,

D.; Fowler, D.; Gallagher, M. W.; Cape, J. N.; Sutton, M. A.; et al. Surface/Atmosphere Exchange and Chemical Interactions of Reactive Nitrogen Compounds above a Manured Grassland. *Agric. For. Meteorol.* **2011**, *151* (12), 1488–1503. https://doi.org/10.1016/j.agrformet.2011.06.005.

(64) Laufs, S.; Cazaunau, M.; Stella, P.; Kurtenbach, R.; Cellier, P.; Mellouki, A.; Loubet, B.; Kleffmann, J. Diurnal Fluxes of HONO above a Crop Rotation. *Atmos. Chem. Phys.* **2017**, *17* (11), 6907–6923. https://doi.org/10.5194/acp-17-6907-2017.

(65) Su, H.; Cheng, Y.; Oswald, R.; Behrendt, T.; Trebs, I.; Meixner, F. X.; Andreae, M. O.; Cheng, P.; Zhang, Y.; Poschl, U. Soil Nitrite as a Source of Atmospheric HONO and OH Radicals. *Science.* **2011**, *333* (6049), 1616–1618. https://doi.org/10.1126/science.1207687.

(66) Oswald, R.; Behrendt, T.; Ermel, M.; Wu, D.; Su, H.; Cheng, Y.; Breuninger, C.; Moravek, A.; Mougin, E.; Delon, C. HONO Emissions from Soil Bacteria as a Major Source of Atmospheric Reactive Nitrogen. *Science.* **2013**, *341* (6151), 1233–1235. https://doi.org/10.1126/science.1242266.

(67) Donaldson, M. A.; Bish, D. L.; Raff, J. D. Soil Surface Acidity Plays a Determining Role in the Atmospheric-Terrestrial Exchange of Nitrous Acid. *Proc. Natl. Acad. Sci. U. S. A.* **2014**, *111* (52), 18472–18477. https://doi.org/10.1073/pnas.1418545112.

(68) Scharko, N. K.; Schütte, U. M. E.; Berke, A. E.; Banina, L.; Peel, H. R.; Donaldson, M. A.; Hemmerich, C.; White, J. R.; Raff, J. D. Combined Flux Chamber and Genomics Approach Links Nitrous Acid Emissions to Ammonia Oxidizing Bacteria and Archaea in Urban and Agricultural Soil. *Environ. Sci. Technol.* **2015**, *49* (23), 13825–13834. https://doi.org/10.1021/acs.est.5b00838.

(69) Weber, B.; Wu, D.; Tamm, A.; Ruckteschler, N.; Rodríguez-Caballero, E.; Steinkamp, J.; Meusel, H.; Elbert, W.; Behrendt, T.; Sörgel, M.; et al. Biological Soil Crusts Accelerate the Nitrogen Cycle through Large NO and HONO Emissions in Drylands. *Proc. Natl. Acad. Sci.* **2015**, *112* (50), 15384–15389. https://doi.org/10.1073/pnas.1515818112.

(70) Ermel, M.; Behrendt, T.; Oswald, R.; Derstroff, B.; Wu, D.; Hohlmann, S.; Stönner, C.; Pommerening-Röser, A.; Könneke, M.; Williams, J.; et al. Hydroxylamine Released by Nitrifying Microorganisms Is a Precursor for HONO Emission from Drying Soils. *Sci. Rep.* **2018**, *8* (1), 1877.

https://doi.org/10.1038/s41598-018-20170-1.

(71) Kim, M.; Or, D. Microscale PH Variations during Drying of Soils and Desert Biocrusts Affect HONO and NH3 Emissions. *Nat. Commun.* **2019**, *10* (1), 1–12. https://doi.org/10.1038/s41467-019-11956-6.

(72) Li, X.; Rohrer, F.; Hofzumahaus, A.; Brauers, T.; Haseler, R.; Bohn, B.; Broch, S.; Fuchs, H.; Gomm, S.; Holland, F.; et al. Missing Gas-Phase Source of HONO Inferred from Zeppelin Measurements in the Troposphere. *Science (80-. ).* **2014**, *344* (6181), 292–296. https://doi.org/10.1126/science.1248999.

(73) Ye, C.; Zhou, X.; Pu, D.; Stutz, J.; Festa, J.; Spolaor, M.; Cantrell, C.; Mauldin, R. L.; Weinheimer, A.; Haggerty, J. Comment on “Missing Gas-Phase Source of HONO Inferred from Zeppelin Measurements in the Troposphere.” *Science.* **2015**, *348* (6241), 1326.

(74) Bejan, I.; Abd El Aal, Y.; Barnes, I.; Benter, T.; Bohn, B.; Wiesen, P.; Kleffmann, J. The Photolysis of Ortho-Nitrophenols: A New Gas Phase Source of HONO. *Phys. Chem. Chem. Phys.* **2006**, *8* (17), 2028–2035. https://doi.org/10.1039/b516590c.

(75) Carr, S.; Heard, D. E.; Blitz, M. A. Comment on “Atmospheric Hydroxyl Radical Production from Electronically Excited $NO_2$ and $H_2O$.” *Science.* **2009**, *324* (5925), 336b-336b. https://doi.org/10.1126/science.1166669.

(76) Amedro, D.; Parker, A. E.; Schoemaecker, C.; Fittschen, C. Direct Observation of OH Radicals after 565 nm Multi-Photon Excitation of $NO_2$ in the Presence of $H_2O$. *Chem. Phys. Lett.* **2011**. https://doi.org/10.1016/j.cplett.2011.07.062.

(77) Kim, S.; VandenBoer, T. C.; Young, C. J.; Riedel, T. P.; Thornton, J. A.; Swarthout, B.; Sive, B.; Lerner, B.; Gilman, J. B.; Warneke, C.; et al. The Primary and Recycling Sources of OH during the NACHTT-2011 Campaign: HONO as an Important OH Primary Source in the Wintertime. *J. Geophys. Res.* **2014**, *119* (11), 6886–6896. https://doi.org/10.1002/2013jd019784.

(78) Tsai, C.; Spolaor, M.; Colosimo, S. F.; Pikelnaya, O.; Cheung, R.; Williams, E.; Gilman, J. B.; Lerner, B. M.; Zamora, R. J.; Warneke, C.; et al. Nitrous Acid Formation in a Snow-Free Wintertime Polluted Rural Area. *Atmos. Chem. Phys. Discuss.* **2017**, *2017*, 1–37. https://doi.org/10.5194/acp-2017-648.

(79) Spataro, F.; Ianniello, A. Sources of Atmospheric Nitrous Acid: State of the Science, Current Research Needs, and Future Prospects. *J. Air Waste Manag. Assoc.* **2014**, *64* (11), 1232–1250.

https://doi.org/10.1080/10962247.2014.952846.

(80) Duan, J.; Qin, M.; Fang, W.; Ling, L. Y.; Hu, R. Z.; Lu, X.; Shen, L. L.; Wang, D.; Xie, P. H.; Liu, J. G.; et al. Incoherent broadband cavity enhanced absorption spectroscopy for measurements of atmospheric HONO. *Acta Phys. Sin.* **2015**, *64* (18), 8. https://doi.org/10.7498/aps.64.180701.

(81) Duan, J.; Qin, M.; Ouyang, B.; Fang, W.; Li, X.; Lu, K.; Tang, K.; Liang, S.; Meng, F.; Hu, Z.; et al. Development of an Incoherent Broadband Cavity-Enhanced Absorption Spectrometer for in Situ Measurements of HONO and NO $_2$. *Atmos. Meas. Tech.* **2018**, *11* (7), 4531–4543. https://doi.org/10.5194/amt-11-4531-2018.

(82) Wu, T.; Zha, Q.; Chen, W.; Xu, Z.; Wang, T.; He, X. Development and Deployment of a Cavity Enhanced UV-LED Spectrometer for Measurements of Atmospheric HONO and $NO_2$ in Hong Kong. *Atmos. Environ.* **2014**, *95* (2), 544–551. https://doi.org/10.1016/j.atmosenv.2014.07.016.

(83) Zhou, X. An Overview of Measurement Techniques for Atmospheric Nitrous Acid. In *NATO Science for Peace and Security Series C: Environmental Security*; Barnes, I., Rudziński, K. J., Eds.; Springer Netherlands: Dordrecht, 2013; Vol. 120, pp 29–44. https://doi.org/10.1007/978-94-007-5034-0_3.

(84) Stockwell, C. E.; Yokelson, R. J.; Kreidenweis, S. M.; Robinson, A. L.; Demott, P. J.; Sullivan, R. C.; Reardon, J.; Ryan, K. C.; Griffith, D. W. T.; Stevens, L. Trace Gas Emissions from Combustion of Peat, Crop Residue, Domestic Biofuels, Grasses, and Other Fuels: Configuration and Fourier Transform Infrared (FTIR) Component of the Fourth Fire Lab at Missoula Experiment (FLAME-4). *Atmos. Chem. Phys.* **2014**, *14* (18), 9727–9754. https://doi.org/10.5194/acp-14-9727-2014.

(85) Chen, L.; Hou, S. Q.; Wang, W. G.; Tong, S. R.; Pei, K. M.; Ge, M. F. Development of a Home-Made Long Path Absorption Photometer for the Sensitive Detection of Nitrous Acid. *Wuli Huaxue Xuebao/ Acta Phys. - Chim. Sin.* **2014**, *30* (8), 1408–1415. https://doi.org/10.3866/PKU.WHXB201406032.

(86) Heland, J.; Kleffmann, J.; Kurtenbach, R.; Wiesen, P. A New Instrument To Measure Gaseous Nitrous Acid (HONO) in the Atmosphere. *Environ. Sci. Technol.* **2001**, *35* (15), 3207–3212. https://doi.org/10.1021/es000303t.

(87) Kleffmann, J.; Heland, J.; Kurtenbach, R.; Lorzer, J.; Wiesen, P. A New Instrument (LOPAP) for the Detection of Nitrous Acid (HONO). *Environ. Sci.*

*Pollut. Res.* **2002**, *9* ((special issue 4)), 48–54. https://doi.org/10.1016/j.aeue.2013.07.005.

(88) Dong, H. B.; Zeng, L. M.; Hu, M.; Yu, Y. S.; Zhang, Y. H.; Slanina, J.; Zheng, M.; Wang, Z. F.; Jansen, R. Technical Note: The Application of an Improved Gas and Aerosol Collector for Ambient Air Pollutants in China. In *Atmospheric Chemistry and Physics*; 2012; Vol. 12, pp 10519–10533. https://doi.org/10.5194/acp-12-10519-2012.

(89) Vandenboer, T. C.; Markovic, M. Z.; Sanders, J. E.; Ren, X.; Pusede, S. E.; Browne, E. C.; Cohen, R. C.; Zhang, L.; Thomas, J.; Brune, W. H. Evidence for a Nitrous Acid (HONO) Reservoir at the Ground Surface in Bakersfield, CA, during CalNex 2010. *J. Geophys. Res. Atmos.* **2015**, *119* (14), 9093–9106.

(90) Wang, J.; Zhang, X.; Guo, J.; Wang, Z.; Zhang, M. Observation of Nitrous Acid (HONO) in Beijing, China: Seasonal Variation, Nocturnal Formation and Daytime Budget. *Sci. Total Environ.* **2017**, *587–588*, 350–359. https://doi.org/10.1016/j.scitotenv.2017.02.159.

(91) Cheng, P.; Cheng, Y.; Lu, K.; Su, H.; Yang, Q.; Zou, Y.; Zhao, Y.; Dong, H.; Zeng, L.; Zhang, Y. An Online Monitoring System for Atmospheric Nitrous Acid (HONO) Based on Stripping Coil and Ion Chromatography. *J. Environ. Sci.* **2013**, *25* (5), 895–907. https://doi.org/10.1016/S1001-0742(12)60251-4.

(92) Zhou, X.; Qiao, H.; Deng, G.; Civerolo, K. A Method for the Measurement of Atmospheric HONO Based on DNPH Derivatization and HPLC Analysis. *Environ. Sci. Technol.* **1999**, *33* (20), 3672–3679.

(93) Liao, W.; Case, A. T.; Mastromarino, J.; Tan, D.; Dibb, J. E. Observations of HONO by Laser-Induced Fluorescence at the South Pole during ANTCI 2003. *Geophys. Res. Lett.* **2006**, *33* (9). https://doi.org/10.1029/2005GL025470.

(94) Levy, M.; Zhang, R.; Zheng, J.; Zhang, A. L.; Xu, W.; Gomez-Hernandez, M.; Wang, Y.; Olaguer, E. Measurements of Nitrous Acid (HONO) Using Ion Drift-Chemical Ionization Mass Spectrometry during the 2009 SHARP Field Campaign. *Atmos. Environ.* **2014**, *94*, 231–240. https://doi.org/10.1016/j.atmosenv.2014.05.024.

(95) Pinto, J. P.; Dibb, J.; Lee, B. H.; Rappenglück, B.; Wood, E. C.; Levy, M.; Zhang, R.-Y.; Lefer, B.; Ren, X.-R.; Stutz, J.; et al. Intercomparison of Field Measurements of Nitrous Acid (HONO) during the SHARP Campaign. *J. Geophys. Res. Atmos.* **2014**, *119* (9), 5583–5601.

https://doi.org/10.1002/2013JD020287.

(96) Alicke, B.; Platt, U.; Stutz, J. Impact of Nitrous Acid Photolysis on the Total Hydroxyl Radical Budget during the Limitation of Oxidant Productioh/Pianura Padana Produzione Di Ozono Study in Milan. *J. Geophys. Res. Atmos.* **2002**, *107* (22). https://doi.org/10.1029/2000JD000075.

(97) Alicke, B. OH Formation by HONO Photolysis during the BERLIOZ Experiment. *J. Geophys. Res.* **2003**, *108* (D4). https://doi.org/10.1029/2001jd000579.

(98) Kleffmann, J.; Gavriloaiei, T.; Hofzumahaus, A.; Holland, F.; Koppmann, R.; Rupp, L.; Schlosser, E.; Siese, M.; Wahner, A. Daytime Formation of Nitrous Acid: A Major Source of OH Radicals in a Forest. *Geophys. Res. Lett.* **2005**, *32* (5), 1–4. https://doi.org/10.1029/2005GL022524.

(99) Bröske, R.; Kleffmann, J.; Wiesen, P. Heterogeneous Conversion of NO&lt;Sub&gt;2&lt;/Sub&gt; on Secondary Organic Aerosol Surfaces: A Possible Source of Nitrous Acid (HONO) in the Atmosphere? *Atmos. Chem. Phys.* **2003**, *3* (3), 469–474. https://doi.org/10.5194/acp-3-469-2003.

(100) Nan, J.; Wang, S.; Guo, Y.; Xiang, Y.; Zhou, B. Study on the Daytime OH Radical and Implication for Its Relationship with Fine Particles over Megacity of Shanghai, China. *Atmos. Environ.* **2017**, *154*, 167–178. https://doi.org/10.1016/j.atmosenv.2017.01.046.

(101) Brown, S. S.; Thornton, J. A.; Keene, W. C.; Pszenny, A. A. P.; Sive, B. C.; Dubé, W. P.; Wagner, N. L.; Young, C. J.; Riedel, T. P.; Roberts, J. M.; et al. Nitrogen, Aerosol Composition, and Halogens on a Tall Tower (NACHTT): Overview of a Wintertime Air Chemistry Field Study in the Front Range Urban Corridor of Colorado. *J. Geophys. Res. Atmos.* **2013**, *118* (14), 8067–8085. https://doi.org/10.1002/jgrd.50537.

(102) Kleffmann, J.; Wiesen, P. Technical Note: Quantification of Interferences of Wet Chemical HONO LOPAP Measurements under Simulated Polar Conditions. *Atmos. Chem. Phys.* **2008**, *8* (22), 6813–6822. https://doi.org/10.5194/acp-8-6813-2008.

(103) Dong, H.; Zeng, L.; Zhang, Y.; Hu, M.; Wu, Y. The Application of an Improved Gas and Aerosol Collector for Ambient Air Pollutants in China. In *EGU General Assembly Conference*; 2016.

(104) Wu, Z.; Hu, M.; Lin, P.; Liu, S.; Wehner, B.; Wiedensohler, A. Particle Number

Size Distribution in the Urban Atmosphere of Beijing, China. *Atmos. Environ.* **2008**, *42* (34), 7967–7980. https://doi.org/10.1016/j.atmosenv.2008.06.022.

(105) Guo, S.; Hu, M.; Zamora, M. L.; Peng, J.; Shang, D.; Zheng, J.; Du, Z.; Wu, Z.; Shao, M.; Zeng, L.; et al. Elucidating Severe Urban Haze Formation in China. *Proc. Natl. Acad. Sci.* **2014**, *111* (49), 17373–17378. https://doi.org/10.1073/pnas.1419604111.

(106) Yang, Y.; Shao, M.; Keßel, S.; Li, Y.; Lu, K.; Lu, S.; Williams, J.; Zhang, Y.; Zeng, L.; Nölscher, A. C.; et al. How the OH Reactivity Affects the Ozone Production Efficiency: Case Studies in Beijing and Heshan, China. *Atmos. Chem. Phys.* **2017**, *17* (11), 7127–7142. https://doi.org/10.5194/acp-17-7127-2017.

(107) Sun, L.; Xue, L.; Wang, T.; Gao, J.; Ding, A.; Cooper, O. R.; Lin, M.; Xu, P.; Wang, Z.; Wang, X.; et al. Significant Increase of Summertime Ozone at Mount Tai in Central Eastern China. **2016**, No. x, 10637–10650. https://doi.org/10.5194/acp-16-10637-2016.

(108) Sun, L.; Xue, L.; Wang, Y.; Li, L.; Lin, J.; Ni, R.; Yan, Y.; Chen, L.; Li, J.; Zhang, Q.; et al. Impacts of Meteorology and Emissions on Summertime Surface Ozone Increases over Central Eastern China between 2003 and 2015. *Atmos. Chem. Phys.* **2019**, *19* (3), 1455–1469. https://doi.org/10.5194/acp-19-1455-2019.

(109) Li, K.; Jacob, D. J.; Liao, H.; Shen, L.; Zhang, Q.; Bates, K. H. Anthropogenic Drivers of 2013–2017 Trends in Summer Surface Ozone in China. *Proc. Natl. Acad. Sci. U. S. A.* **2019**, *116* (2), 422–427. https://doi.org/10.1073/pnas.1812168116.

(110) Liao, H.; Chang, W.; Yang, Y. Climatic Effects of Air Pollutants over China: A Review. *Adv. Atmos. Sci.* **2015**, *32* (1), 115–139. https://doi.org/10.1007/s00376-014-0013-x.

(111) Wang, G.; Zhang, R.; Gomez, M. E.; Yang, L.; Levy Zamora, M.; Hu, M.; Lin, Y.; Peng, J.; Guo, S.; Meng, J.; et al. Persistent Sulfate Formation from London Fog to Chinese Haze. *Proc. Natl. Acad. Sci.* **2016**, *113* (48), 13630–13635. https://doi.org/10.1073/pnas.1616540113.

(112) Cheng, Y.; Zheng, G.; Wei, C.; Mu, Q.; Zheng, B.; Wang, Z.; Gao, M.; Zhang, Q.; He, K.; Carmichael, G.; et al. Reactive Nitrogen Chemistry in Aerosol Water as a Source of Sulfate during Haze Events in China. *Sci. Adv.* **2016**, *2* (12). https://doi.org/10.1126/sciadv.1601530.

(113) Wang, H.; Lu, K.; Chen, X.; Zhu, Q.; Chen, Q.; Guo, S.; Jiang, M.; Li, X.; Shang, D.; Tan, Z.; et al. High $N_2O_5$ Concentrations Observed in Urban Beijing: Implications of a Large Nitrate Formation Pathway. *Environ. Sci. Technol. Lett.* **2017**, *4* (10), 416–420. https://doi.org/10.1021/acs.estlett.7b00341.

(114) Yun, H.; Wang, W.; Wang, T.; Xia, M.; Yu, C.; Wang, Z.; C. N. Poon, S.; Yue, D.; Zhou, Y. Nitrate Formation from Heterogeneous Uptake of Dinitrogen Pentoxide during a Severe Winter Haze in Southern China. *Atmos. Chem. Phys.* **2018**, *18* (23), 17515–17527. https://doi.org/10.5194/acp-18-17515-2018.

(115) Wang, H.; Lu, K.; Chen, X.; Zhu, Q.; Wu, Z.; Wu, Y.; Sun, K. Fast Particulate Nitrate Formation via N2O5uptake Aloft in Winter in Beijing. *Atmos. Chem. Phys.* **2018**, *18* (14), 10483–10495. https://doi.org/10.5194/acp-18-10483-2018.

(116) Song, S.; Gao, M.; Xu, W.; Shao, J.; Shi, G.; Wang, S.; Wang, Y.; Sun, Y.; McElroy, M. B. Fine-Particle PH for Beijing Winter Haze as Inferred from Different Thermodynamic Equilibrium Models. *Atmos. Chem. Phys.* **2018**, *18* (10), 7423–7438. https://doi.org/10.5194/acp-18-7423-2018.

(117) Ma, Z.; Xu, J.; Quan, W.; Zhang, Z.; Lin, W.; Xu, X. Significant Increase of Surface Ozone at a Rural Site, North of Eastern China. *Atmos. Chem. Phys.* **2016**, *16* (6), 3969–3977. https://doi.org/10.5194/acp-16-3969-2016.

(118) Tham, Y. J.; Wang, Z.; Li, Q.; Yun, H.; Wang, W.; Wang, X.; Xue, L.; Lu, K.; Ma, N.; Bohn, B.; et al. Significant Concentrations of Nitryl Chloride Sustained in the Morning: Investigations of the Causes and Impacts on Ozone Production in a Polluted Region of Northern China. *Atmos. Chem. Phys.* **2016**, *16* (23), 14959–14977. https://doi.org/10.5194/acp-16-14959-2016.

(119) Zhou, F.; Shao, K.; Hu, M.; Tang, X. Concentrations of Aerosol and Related Gases in Beijing. *Huanjing Kexue/Environmental Sci.* **2002**, *23* (1), 11.

(120) Qin, M.; Xie, P. H.; Liu, W. Q.; Li, A.; Dou, K.; Fang, W.; Liu, J. G.; Zhang, W. J. Observation of Atmospheric Nitrous Acid with DOAS in Beijing, China. *J. Environ. Sci.* **2006**, *18* (1), 69–75.

(121) Yang, Q.; Su, H.; Li, X.; Cheng, Y.; Lu, K.; Cheng, P.; Gu, J.; Guo, S.; Hu, M.; Zeng, L.; et al. Daytime HONO Formation in the Suburban Area of the Megacity Beijing, China. *Sci. China Chem.* **2014**, *57* (7), 1032–1042. https://doi.org/10.1007/s11426-013-5044-0.

(122) Zhu, Y. W.; Fu, Q.; Xie, P. H.; Liu, W. Q.; Peng, F. M.; Qin, M.; Lin, Y. H.; Si, F. Q.; Dou, K. Monitoring and Analysis of Air Pollutants Using DOAS in Winter

of Beijing. *Guang Pu Xue Yu Guang Pu Fen Xi/Spectroscopy Spectr. Anal.* **2009**, *29* (5), 1390–1393. https://doi.org/10.3964/j.issn.1000-0593(2009)05-1390-04.

(123) Spataro, F.; Ianniello, A.; Esposito, G.; Allegrini, I.; Zhu, T.; Hu, M. Occurrence of Atmospheric Nitrous Acid in the Urban Area of Beijing (China). *Sci. Total Environ.* **2013**, *447*, 210–224. https://doi.org/10.1016/j.scitotenv.2012.12.065.

(124) Hendrick, F.; Müller, J.-F.; Clémer, K.; Wang, P.; De Mazière, M.; Fayt, C.; Gielen, C.; Hermans, C.; Ma, J. Z.; Pinardi, G.; et al. Four Years of Ground-Based MAX-DOAS Observations of HONO and NO 2 in the Beijing Area. *Atmos. Chem. Phys.* **2014**, *14* (2), 765–781. https://doi.org/10.5194/acp-14-765-2014.

(125) Wang, L.; Wen, L.; Xu, C.; Chen, J.; Wang, X.; Yang, L.; Wang, W.; Yang, X.; Sui, X.; Yao, L.; et al. HONO and Its Potential Source Particulate Nitrite at an Urban Site in North China during the Cold Season. *Sci. Total Environ.* **2015**, *538*, 93–101. https://doi.org/10.1016/j.scitotenv.2015.08.032.

(126) Hou, S.; Tong, S.; Ge, M.; An, J. Comparison of Atmospheric Nitrous Acid during Severe Haze and Clean Periods in Beijing, China. *Atmos. Environ.* **2016**, *124*, 199–206. https://doi.org/10.1016/j.atmosenv.2015.06.023.

(127) Tong, S.; Hou, S.; Zhang, Y.; Chu, B.; Liu, Y.; He, H.; Zhao, P.; Ge, M. Exploring the Nitrous Acid (HONO) Formation Mechanism in Winter Beijing: Direct Emissions and Heterogeneous Production in Urban and Suburban Areas. *Faraday Discuss.* **2016**, *189*, 213–230. https://doi.org/10.1039/c5fd00163c.

(128) Wang, J.; Zhang, X.; Guo, J.; Wang, Z.; Zhang, M. Observation of Nitrous Acid (HONO) in Beijing, China: Seasonal Variation, Nocturnal Formation and Daytime Budget. *Sci. Total Environ.* **2017**, *587–588*, 350–359. https://doi.org/10.1016/j.scitotenv.2017.02.159.

(129) Xu, W.; Kuang, Y.; Zhao, C.; Tao, J.; Zhao, G.; Bian, Y.; Yang, W.; Yu, Y.; Shen, C.; Liang, L.; et al. NH3-Promoted Hydrolysis of $NO_2$ Induces Explosive Growth in HONO. *Atmos. Chem. Phys.* **2019**, *19* (16), 10557–10570. https://doi.org/10.5194/acp-19-10557-2019.

(130) An, J.; Li, Y.; Chen, Y.; Li, J.; Qu, Y.; Tang, Y. Enhancements of Major Aerosol Components Due to Additional HONO Sources in the North China Plain and Implications for Visibility and Haze. *Adv. Atmos. Sci.* **2013**, *30* (1), 57–66. https://doi.org/10.1007/s00376-012-2016-9.

(131) Li, Y.; An, J.; Gultepe, I. Effects of Additional HONO Sources on Visibility over

the North China Plain. *Adv. Atmos. Sci.* **2014**, *31* (5), 1221–1232. https://doi.org/10.1007/s00376-014-4019-1.

(132) Fu, X.; Wang, T.; Zhang, L.; Li, Q.; Wang, Z.; Xia, M.; Yun, H.; Wang, W.; Yu, C.; Yue, D.; et al. The Significant Contribution of HONO to Secondary Pollutants during a Severe Winter Pollution Event in Southern China. *Atmos. Chem. Phys.* **2019**, *19* (1), 1–14. https://doi.org/10.5194/acp-19-1-2019.

(133) Xing, L.; Wu, J.; Elser, M.; Tong, S.; Liu, S.; Li, X.; Liu, L.; Cao, J.; Zhou, J.; El-Haddad, I.; et al. Wintertime Secondary Organic Aerosol Formation in Beijing-Tianjin-Hebei (BTH): Contributions of HONO Sources and Heterogeneous Reactions. **2018**, No. September, 1–25. https://doi.org/10.5194/acp-2018-770.

(134) Qu, Y.; Chen, Y.; Liu, X.; Zhang, J.; Guo, Y.; An, J. Seasonal Effects of Additional HONO Sources and the Heterogeneous Reactions of $N_2O_5$ on Nitrate in the North China Plain. *Sci. Total Environ.* **2019**, *690*, 97–107. https://doi.org/10.1016/j.scitotenv.2019.06.436.

(135) Zhang, J.; An, J.; Qu, Y.; Liu, X.; Chen, Y. Impacts of Potential HONO Sources on the Concentrations of Oxidants and Secondary Organic Aerosols in the Beijing-Tianjin-Hebei Region of China. *Sci. Total Environ.* **2019**, *647*, 836–852. https://doi.org/10.1016/j.scitotenv.2018.08.030.

(136) Zhang, J.; Chen, J.; Xue, C.; Chen, H.; Zhang, Q.; Liu, X.; Mu, Y.; Guo, Y.; Wang, D.; Chen, Y.; et al. Impacts of Six Potential HONO Sources on HOx Budgets and SOA Formation during a Wintertime Heavy Haze Period in the North China Plain. *Sci. Total Environ.* **2019**, *681*, 110–123. https://doi.org/10.1016/j.scitotenv.2019.05.100.

(137) Meller, R.; Moortgat, G. K. Temperature Dependence of the Absorption Cross Sections of Formaldehyde between 223 and 323 K in the Wavelength Range 225-375 Nm. *J. Geophys. Res. Atmos.* **2000**. https://doi.org/10.1029/1999JD901074.

(138) Zhu, Y. W.; Liu, W. Q.; Xie, P. H.; Dou, K.; Liu, S. S.; Si, F. Q.; Li, S. W.; Qin, M. Observational Study of Atmospheric HONO in Summer of Beijing. *Huanjing Kexue/Environmental Sci.* **2009**.

(139) Xue, C.; Ye, C.; Ma, Z.; Liu, P.; Zhang, Y.; Zhang, C.; Tang, K.; Zhang, W.; Zhao, X.; Wang, Y.; et al. Development of Stripping Coil-Ion Chromatograph Method and Intercomparison with CEAS and LOPAP to Measure Atmospheric

HONO. *Sci. Total Environ.* **2019**, *646*, 187–195. https://doi.org/10.1016/j.scitotenv.2018.07.244.

(140) Bongartz, A.; Kames, J.; Schurath, U.; George, C.; Mirabel, P.; Ponche, J. L. Experimental Determination of HONO Mass Accommodation Coefficients Using Two Different Techniques. *J. Atmos. Chem.* **1994**, *18* (2), 149–169. https://doi.org/10.1007/BF00696812.

(141) Wongphatarakul, V.; Friedlander, S. K.; Pinto, J. P. A Comparative Study of PM2.5 Ambient Aerosol Chemical Databases. *Environ. Sci. Technol.* **1998**. https://doi.org/10.1021/es9800582.

(142) Xue, C.; Ye, C.; Zhang, Y.; Ma, Z.; Liu, P.; Zhang, C.; Zhao, X.; Liu, J.; Mu, Y. Development and Application of a Twin Open-Top Chambers Method to Measure Soil HONO Emission in the North China Plain. *Sci. Total Environ.* **2019**, *659*, 621–631. https://doi.org/10.1016/j.scitotenv.2018.12.245.

(143) Zhang, Y.; Liu, J.; Mu, Y.; Xu, Z.; Pei, S.; Lun, X.; Zhang, Y. Nitrous Oxide Emissions from a Maize Field during Two Consecutive Growing Seasons in the North China Plain. *J. Environ. Sci.* **2012**, *24* (1), 160–168. https://doi.org/10.1016/S1001-0742(10)60594-3.

(144) Zhang, Y.; Mu, Y.; Zhou, Y.; Tian, D.; Liu, J.; Zhang, C. NO and N2O Emissions from Agricultural Fields in the North China Plain: Origination and Mitigation. *Sci. Total Environ.* **2016**, *551–552*, 197–204. https://doi.org/10.1016/j.scitotenv.2016.01.209.

(145) Zhang, Y.; Liu, J.; Mu, Y.; Pei, S.; Lun, X.; Chai, F. Emissions of Nitrous Oxide, Nitrogen Oxides and Ammonia from a Maize Field in the North China Plain. *Atmos. Environ.* **2011**, *45* (17), 2956–2961. https://doi.org/10.1016/j.atmosenv.2010.10.052.

(146) Tian, D.; Zhang, Y.; Zhou, Y.; Mu, Y.; Liu, J.; Zhang, C.; Liu, P. Effect of Nitrification Inhibitors on Mitigating $N_2O$ and NO Emissions from an Agricultural Field under Drip Fertigation in the North China Plain. *Sci. Total Environ.* **2017**, *598*, 87–96. https://doi.org/10.1016/j.scitotenv.2017.03.220.

(147) Laufs, S.; Kleffmann, J. Investigations on HONO Formation from Photolysis of Adsorbed $HNO_3$ on Quartz Glass Surfaces. *Phys. Chem. Chem. Phys.* **2016**, *18* (14), 9616–9625. https://doi.org/10.1039/c6cp00436a.

(148) Ren, X.; Sanders, J. E.; Rajendran, A.; Weber, R. J. A Relaxed Eddy Accumulation System for Measuring Vertical Fluxes of Nitrous Acid. *Atmos.*

*Meas. Tech.* **2011**, *4* (10), 2093–2103. https://doi.org/10.5194/amt-4-2093-2011.

(149) Zhou, X.; Zhang, N.; Teravest, M.; Tang, D.; Hou, J.; Bertman, S.; Alaghmand, M.; Shepson, P. B.; Carroll, M. A.; Griffith, S.; et al. Nitric Acid Photolysis on Forest Canopy Surface as a Source for Tropospheric Nitrous Acid. *Nat. Geosci.* **2011**, *4* (7), 440–443. https://doi.org/10.1038/ngeo1164.

(150) Oswald, R.; Behrendt, T.; Ermel, M.; Wu, D.; Su, H.; Cheng, Y.; Breuninger, C.; Moravek, A.; Mougin, E.; Delon, C.; et al. HONO Emissions from Soil Bacteria as a Major Source of Atmospheric Reactive Nitrogen. *Science.* **2013**, *341* (6151), 1233–1235. https://doi.org/10.1126/science.1242266.

(151) Ermel, M.; Behrendt, T.; Oswald, R.; Derstroff, B.; Wu, D.; Hohlmann, S.; Stönner, C.; Pommerening-Röser, A.; Könneke, M.; Williams, J.; et al. Hydroxylamine Released by Nitrifying Microorganisms Is a Precursor for HONO Emission from Drying Soils. *Sci. Rep.* **2018**, *8* (1), 1877. https://doi.org/10.1038/s41598-018-20170-1.

(152) Cui, Z.; Zhang, F.; Chen, X.; Miao, Y.; Li, J.; Shi, L.; Xu, J.; Ye, Y.; Liu, C.; Yang, Z.; et al. On-Farm Evaluation of an in-Season Nitrogen Management Strategy Based on Soil Nmintest. *F. Crop. Res.* **2008**, *105* (1–2), 48–55. https://doi.org/10.1016/j.fcr.2007.07.008.

(153) Miao, Y.; Stewart, B. A.; Zhang, F. Long-Term Experiments for Sustainable Nutrient Management in China. A Review. *Agron. Sustain. Dev.* **2011**, *31* (2), 397–414. https://doi.org/10.1051/agro/2010034.

(154) Heland, J.; Kleffmann, J.; Kurtenbach, R.; Wiesen, P. A New Instrument To Measure Gaseous Nitrous Acid (HONO) in the Atmosphere. *Environ. Sci. Technol.* **2001**, *35* (15), 3207–3212. https://doi.org/10.1021/es000303t.

(155) Su, H.; Cheng, Y.; Oswald, R.; Behrendt, T.; Trebs, I.; Meixner, F. X.; Andreae, M. O.; Cheng, P.; Zhang, Y.; Poschl, U. Soil Nitrite as a Source of Atmospheric HONO and OH Radicals. *Science.* **2011**, *333* (6049), 1616–1618. https://doi.org/10.1126/science.1207687.

(156) Wu, D.; Horn, M. A.; Behrendt, T.; Müller, S.; Li, J.; Cole, J. A.; Xie, B.; Ju, X.; Li, G.; Ermel, M.; et al. Soil HONO Emissions at High Moisture Content Are Driven by Microbial Nitrate Reduction to Nitrite: Tackling the HONO Puzzle. *ISME J.* **2019**. https://doi.org/10.1038/s41396-019-0379-y.

(157) Galmarini, S.; Vilà-Guerau De Arellano, J.; Duyzer, J. Fluxes of Chemically Reactive Species Inferred from Mean Concentration Measurements. *Atmos.*

*Environ.* **1997**, *31* (15), 2371–2374. https://doi.org/10.1016/S1352-2310(97)00026-5.

(158) Pryor, S. .; Barthelmie, R. .; Jensen, B.; Jensen, N. .; Sørensen, L. . $HNO_3$ Fluxes to a Deciduous Forest Derived Using Gradient and REA Methods. *Atmos. Environ.* **2002**, *36* (39–40), 5993–5999. https://doi.org/10.1016/S1352-2310(02)00765-3.

(159) Knowles, R. Denitrification. *Microbiol. Rev.* **1982**, *46* (1), 43–70. (160) Zhao, B.; Zheng, H.; Wang, S.; Smith, K. R.; Lu, X.; Aunan, K.; Gu, Y.; Wang, Y.; Ding, D.; Xing, J.; et al. Change in Household Fuels Dominates the Decrease in PM2.5 Exposure and Premature Mortality in China in 2005–2015. *Proc. Natl. Acad. Sci. U. S. A.* **2018**, *115* (49), 12401–12406. https://doi.org/10.1073/pnas.1812955115.

(161) Zheng, B.; Tong, D.; Li, M.; Liu, F.; Hong, C.; Geng, G.; Li, H.; Li, X.; Peng, L.; Qi, J.; et al. Trends in China’s Anthropogenic Emissions since 2010 as the Consequence of Clean Air Actions. *Atmos. Chem. Phys.* **2018**. https://doi.org/10.5194/acp-18-14095-2018.

(162) Fuchs, H.; Tan, Z.; Lu, K.; Bohn, B.; Broch, S.; Brown, S. S.; Dong, H.; Gomm, S.; Häseler, R.; He, L.; et al. OH Reactivity at a Rural Site (Wangdu) in the North China Plain: Contributions from OH Reactants and Experimental OH Budget. *Atmos. Chem. Phys.* **2017**, *17* (1), 645–661. https://doi.org/10.5194/acp-17-645-2017.

(163) Saunders, S. M.; Jenkin, M. E.; Derwent, R. G.; Pilling, M. J. Protocol for the Development of the Master Chemical Mechanism, MCM v3 (Part A): Tropospheric Degradation of Non-Aromatic Volatile Organic Compounds. *Atmos. Chem. Phys.* **2003**, *3* (1), 161–180. https://doi.org/10.5194/acp-3-161-2003.

(164) Liu, P.; Zhang, C.; Mu, Y.; Liu, C.; Xue, C.; Ye, C.; Liu, J.; Zhang, Y.; Zhang, H. The Possible Contribution of the Periodic Emissions from Farmers’ Activities in the North China Plain to Atmospheric Water-Soluble Ions in Beijing. *Atmos. Chem. Phys.* **2016**, *16* (15), 10097–10109. https://doi.org/10.5194/acp-16-10097-2016.

(165) Liu, P.; Zhang, C.; Xue, C.; Mu, Y.; Liu, J.; Zhang, Y.; Tian, D.; Ye, C.; Zhang, H.; Guan, J. The Contribution of Residential Coal Combustion to Atmospheric $PM_{2.5}$ in Northern China during Winter. *Atmos. Chem. Phys.* **2017**, *17* (18),

11503–11520. https://doi.org/10.5194/acp-17-11503-2017.

(166) Kleffmann, J.; Lörzer, J. C.; Wiesen, P.; Kern, C.; Trick, S.; Volkamer, R.; Rodenas, M.; Wirtz, K. Intercomparison of the DOAS and LOPAP Techniques for the Detection of Nitrous Acid (HONO). *Atmos. Environ.* **2006**, *40* (20), 3640–3652. https://doi.org/10.1016/j.atmosenv.2006.03.027.

(167) Song, S.; Gao, M.; Xu, W.; Shao, J.; Shi, G.; Wang, S.; Wang, Y.; Sun, Y.; McElroy, M. B. Fine-Particle PH for Beijing Winter Haze as Inferred from Different Thermodynamic Equilibrium Models. *Atmos. Chem. Phys.* **2018**, *18* (10), 7423–7438. https://doi.org/10.5194/acp-18-7423-2018.

(168) Sommariva, R.; Cox, S.; Martin, C.; Borońska, K.; Young, J.; Jimack, P.; Pilling, M.; Matthaios, V.; Newland, M.; Panagi, M.; et al. AtChem, an Open Source Box-Model for the Master Chemical Mechanism. *Geosci. Model Dev. Discuss.* **2019**, 1–27. https://doi.org/10.5194/gmd-2019-192.

(169) Harrison, R. M.; Peak, J. D.; Collins, G. M. Tropospheric Cycle of Nitrous Acid. *J. Geophys. Res. Atmos.* **1996**, *101* (D9), 14429–14439. https://doi.org/10.1029/96JD00341.

(170) Yu, Y.; Galle, B.; Panday, A.; Hodson, E.; Prinn, R.; Wang, S. Observations of High Rates of $NO_2$-HONO Conversion in the Nocturnal Atmospheric Boundary Layer in Kathmandu, Nepal. *Atmos. Chem. Phys.* **2009**, *9* (17), 6401–6415. https://doi.org/10.5194/acp-9-6401-2009.

(171) Tang, G.; Zhang, J.; Zhu, X.; Song, T.; Münkel, C.; Hu, B.; Schäfer, K.; Liu, Z.; Zhang, J.; Wang, L.; et al. Mixing Layer Height and Its Implications for Air Pollution over Beijing, China. *Atmos. Chem. Phys.* **2016**, *16* (4), 2459–2475. https://doi.org/10.5194/acp-16-2459-2016.

(172) Luo, T.; Wang, Z.; Zhang, D.; Chen, B. Marine Boundary Layer Structure as Observed by A-Train Satellites. *Atmos. Chem. Phys.* **2016**, *16* (9), 5891–5903. https://doi.org/10.5194/acp-16-5891-2016.

(173) Zhu, X.; Tang, G.; Guo, J.; Hu, B.; Song, T.; Wang, L.; Xin, J.; Gao, W.; Münkel, C.; Schäfer, K.; et al. Mixing Layer Height on the North China Plain and Meteorological Evidence of Serious Air Pollution in Southern Hebei. *Atmos. Chem. Phys.* **2018**, *18* (7), 4897–4910. https://doi.org/10.5194/acp-18-4897-2018.

(174) Lee, J. D.; Whalley, L. K.; Heard, D. E.; Stone, D.; Dunmore, R. E.; Hamilton, J. F.; Young, D. E.; Allan, J. D.; Laufs, S.; Kleffmann, J. Detailed Budget

Analysis of HONO in Central London Reveals a Missing Daytime Source. *Atmos. Chem. Phys.* **2016**, *16* (5), 2747–2764. https://doi.org/10.5194/acp-16-2747-2016.

(175) Han, C.; Yang, W.; Wu, Q.; Yang, H.; Xue, X. Heterogeneous Photochemical Conversion of $NO_2$ to HONO on the Humic Acid Surface under Simulated Sunlight. *Environ. Sci. Technol.* **2016**, *50* (10), 5017–5023. https://doi.org/10.1021/acs.est.5b05101.

(176) Stemmler, K.; Ndour, M.; Elshorbany, Y.; Kleffmann, J.; D'Anna, B.; George, C.; Bonn, B.; Ammann, M. Light Induced Conversion of Nitrogen Dioxide into Nitrous Acid on Submicron Humic Acid Aerosol. *Atmos. Chem. Phys.* **2007**, *7* (16), 4237–4248. https://doi.org/10.5194/acp-7-4237-2007.

(177) Ndour, M.; D'Anna, B.; George, C.; Ka, O.; Balkanski, Y.; Kleffmann, J.; Stemmler, K.; Ammann, M. Photoenhanced Uptake of $NO_2$ on Mineral Dust: Laboratory Experiments and Model Simulations. *Geophys. Res. Lett.* **2008**, *35* (5). https://doi.org/10.1029/2007GL032006.

(178) Nakashima, Y.; Sadanaga, Y.; Saito, S.; Hoshi, J.; Ueno, H. Contributions of Vehicular Emissions and Secondary Formation to Nitrous Acid Concentrations in Ambient Urban Air in Tokyo in the Winter. *Sci. Total Environ.* **2017**, *592*, 178–186. https://doi.org/10.1016/j.scitotenv.2017.03.122.

(179) Liu, Z.; Wang, Y.; Costabile, F.; Amoroso, A.; Zhao, C.; Huey, L. G.; Stickel, R.; Liao, J.; Zhu, T. Evidence of Aerosols as a Media for Rapid Daytime HONO Production over China. *Environ. Sci. Technol.* **2014**, *48* (24), 14386–14391. https://doi.org/10.1021/es504163z.

(180) Zhang, N.; Zhou, X.; Bertman, S.; Tang, D.; Alaghmand, M.; Shepson, P. B.; Carroll, M. A. Measurements of Ambient HONO Concentrations and Vertical HONO Flux above a Northern Michigan Forest Canopy. *Atmos. Chem. Phys.* **2012**, *12* (17), 8285–8296. https://doi.org/10.5194/acp-12-8285-2012.

(181) Romer, P. S.; Wooldridge, P. J.; Crounse, J. D.; Kim, M. J.; Wennberg, P. O.; Dibb, J. E.; Scheuer, E.; Blake, D. R.; Meinardi, S.; Brosius, A. L.; et al. Constraints on Aerosol Nitrate Photolysis as a Potential Source of HONO and $NO_X$. *Environ. Sci. Technol.* **2018**, *52* (23), 13738–13746. https://doi.org/10.1021/acs.est.8b03861.

(182) Xu, Z.; Wang, T.; Wu, J.; Xue, L.; Chan, J.; Zha, Q.; Zhou, S.; Louie, P. K. K.; Luk, C. W. Y. Nitrous Acid (HONO) in a Polluted Subtropical Atmosphere:

Seasonal Variability, Direct Vehicle Emissions and Heterogeneous Production at Ground Surface. *Atmos. Environ.* **2015**, *106*, 100–109. https://doi.org/10.1016/j.atmosenv.2015.01.061.

(183) Ji, Y.; Qin, X.; Wang, B.; Xu, J.; Shen, J.; Chen, J.; Huang, K.; Deng, C.; Yan, R.; Xu, K.; et al. Counteractive Effects of Regional Transport and Emission Control on the Formation of Fine Particles: A Case Study during the Hangzhou G20 Summit. *Atmos. Chem. Phys.* **2018**, *18* (18), 13581–13600. https://doi.org/10.5194/acp-18-13581-2018.

(184) Heard, D. E.; Carpenter, L. J.; Creasey, D. J.; Hopkins, J. R.; Lee, J. D.; Lewis, A. C.; Pilling, M. J.; Seakins, P. W.; Carslaw, N.; Emmerson, K. M. High Levels of the Hydroxyl Radical in the Winter Urban Troposphere. *Geophys. Res. Lett.* **2004**, *31* (18). https://doi.org/10.1029/2004GL020544.

(185) Michoud, V.; Colomb, A.; Borbon, A.; Miet, K.; Beekmann, M.; Camredon, M.; Aumont, B.; Perrier, S.; Zapf, P.; Siour, G.; et al. Study of the Unknown HONO Daytime Source at a European Suburban Site during the MEGAPOLI Summer and Winter Field Campaigns. *Atmos. Chem. Phys.* **2014**, *14* (6), 2805–2822. https://doi.org/10.5194/acp-14-2805-2014.

(186) Edwards, P. M.; Brown, S. S.; Roberts, J. M.; Ahmadov, R.; Banta, R. M.; DeGouw, J. A.; Dubé, W. P.; Field, R. A.; Flynn, J. H.; Gilman, J. B.; et al. High Winter Ozone Pollution from Carbonyl Photolysis in an Oil and Gas Basin. *Nature* **2014**, *514* (7522), 351–354. https://doi.org/10.1038/nature13767.

(187) Ma, X.; Tan, Z.; Lu, K.; Yang, X.; Liu, Y.; Li, S.; Li, X.; Chen, S.; Novelli, A.; Cho, C.; et al. Winter Photochemistry in Beijing: Observation and Model Simulation of OH and $HO_2$ Radicals at an Urban Site. *Sci. Total Environ.* **2019**. https://doi.org/10.1016/j.scitotenv.2019.05.329.

(188) Wong, K. W.; Tsai, C.; Lefer, B.; Grossberg, N.; Stutz, J. Modeling of Daytime HONO Vertical Gradients during SHARP 2009. *Atmos. Chem. Phys.* **2013**, *13* (7), 3587–3601. https://doi.org/10.5194/acp-13-3587-2013.

(189) Lin, Y. C.; Cheng, M. T.; Ting, W. Y.; Yeh, C. R. Characteristics of Gaseous $HNO_2$, $HNO_3$, $NH_3$ and Particulate Ammonium Nitrate in an Urban City of Central Taiwan. *Atmos. Environ.* **2006**, *40* (25), 4725–4733. https://doi.org/10.1016/j.atmosenv.2006.04.037.

(190) Alexander, B.; Hastings, M. G.; Allman, D. J.; Dachs, J.; Thornton, J. A.; Kunasek, S. A. Quantifying Atmospheric Nitrate Formation Pathways Based on

a Global Model of the Oxygen Isotopic Composition ($\Delta^{17}O$) of Atmospheric Nitrate. *Atmos. Chem. Phys.* **2009**, *9* (14), 5043–5056. https://doi.org/10.5194/acp-9-5043-2009.

(191) Alexander, B.; Sherwen, T.; Holmes, C. D.; Fisher, J. A.; Chen, Q.; Evans, M. J.; Kasibhatla, P. Global Inorganic Nitrate Production Mechanisms: Comparison of a Global Model with Nitrate Isotope Observations. *Atmos. Chem. Phys. Discuss.* **2019**, 1–36. https://doi.org/10.5194/acp-2019-422.

(192) Michoud, V.; Kukui, A.; Camredon, M.; Colomb, A.; Borbon, A.; Miet, K.; Aumont, B.; Beekmann, M.; Durand-Jolibois, R.; Perrier, S.; et al. Radical Budget Analysis in a Suburban European Site during the MEGAPOLI Summer Field Campaign. *Atmos. Chem. Phys.* **2012**, *12* (24), 11951–11974. https://doi.org/10.5194/acp-12-11951-2012.

(193) Lu, K.; Fuchs, H.; Hofzumahaus, A.; Tan, Z.; Wang, H.; Zhang, L.; Schmitt, S.; Rohrer, F.; Bohn, B.; Broch, S.; et al. Fast Photochemistry in Wintertime Haze: Consequences for Pollution Mitigation Strategies. *Environ. Sci. Technol.* **2019**, acs.est.9b02422. https://doi.org/10.1021/acs.est.9b02422.

(194) Villena, G.; Wiesen, P.; Cantrell, C. A.; Flocke, F.; Fried, A.; Hall, S. R.; Hornbrook, R. S.; Knapp, D.; Kosciuch, E.; Mauldin, R. L.; et al. Nitrous Acid (HONO) during Polar Spring in Barrow, Alaska: A Net Source of OH Radicals? *J. Geophys. Res. Atmos.* **2011**, *116* (24), 1–12. https://doi.org/10.1029/2011JD016643.

(195) Wen, L.; Xue, L.; Wang, X.; Xu, C.; Chen, T.; Yang, L.; Wang, T.; Zhang, Q.; Wang, W. Summertime Fine Particulate Nitrate Pollution in the North China Plain: Increasing Trends, Formation Mechanisms and Implications for Control Policy. *Atmos. Chem. Phys.* **2018**, *18* (15), 11261–11275. https://doi.org/10.5194/acp-18-11261-2018.

(196) Liu, P.; Zhang, C.; Mu, Y.; Liu, C.; Xue, C.; Ye, C.; Liu, J.; Zhang, Y.; Zhang, H. The Possible Contribution of the Periodic Emissions from Farmers' Activities in the North China Plain to Atmospheric Water-Soluble Ions in Beijing. *Atmos. Chem. Phys.* **2016**, *16* (15), 10097–10109. https://doi.org/10.5194/acp-16-10097-2016.

# Chaoyang XUE

## Les sources de HONO atmosphérique rural et leur impact sur la qualité de l'air régional dans la Plaine de Chine du Nord

**Résumé:**
La pollution de l'air est toujours un problème environnemental qui doit être résolu de toute urgence dans la Plaine de Chine du Nord (PCN). Dans le but d'explorer la formation de l’acide nitreux (HONO) et son impact sur la qualité de l'air régional dans la PCN, le développement et l'évaluation systématique d'instruments pour mesurer la concentration de HONO atmosphérique et son flux d'émission du sol ont été réalisés. Sur la base de mesures sur le terrain, un modèle 3D de chimie-transport (le système communautaire de modélisation de la qualité de l'air à plusieurs échelles : CMAQ, de l’EPA) et un modèle de boîte (0D) de mécanisme chimique (Master Chemical Mechanism : MCM) ont été utilisés pour explorer le bilan de HONO et son impact sur la pollution atmosphérique régionale, par exemple la pollution estivale à l'ozone ($O_3$) et la pollution par la brume hivernale. Nous avons constaté que le sol agricole était une source importante de HONO avec un impact significatif sur la pollution régionale à l'ozone en été. Un nouveau mécanisme d'émission de HONO du sol lié à la nitrification a été proposé. HONO joue également un rôle important dans la capacité oxydante de l’atmosphère et la détérioration de la qualité de l'air régional en hiver.

**Mots clés:** HONO, Plaine de Chine du Nord, émissions atmosphériques, $O_3$, nitrate particulaire

## The Sources of Rural Atmospheric HONO and Their Impact on Regional Air Quality in The North China Plain

**Summary:**
Air pollution is still an environmental problem that urgently needs to be solved in the North China Plain (NCP). With the aim to explore nitrous acid (HONO) formation and its impact on regional air quality in the NCP, the development and systematic assessment of instruments to measure atmospheric HONO concentration and soil HONO emission flux were realized. Based on field measurements, a 3D chemistry-transport model (the Community Multiscale Air Quality Modeling System, CMAQ) and a box (0D) model (Master Chemical Mechanism, MCM) were used to explore the HONO budget and its impact on regional air pollution, e.g., summer ozone ($O_3$) pollution and winter haze pollution. We found that agricultural soil was an important HONO source with a significant impact on regional $O_3$ pollution in the summertime. A new soil HONO emission mechanism related to nitrification was proposed. HONO also plays an important role in atmospheric oxidizing capacity and deteriorating regional air quality in the wintertime.

**Keywords:** HONO, North China Plain, atmospheric emissions, $O_3$, particulate nitrate

**LPC2E, CNRS-Université d’Orléans-CNES**
**3A avenue de la Recherche Scientifique**
**45071 Orléans Cedex 2, FRANCE**